

This is to certify that the

thesis entitled


Quantitative and Analytical High-Resolution
Transmission Electron Microscopy Study
of Epitaxial Co/Cu GMR Multilayers

presented by

John W. Heckman, Jr.

has been accepted towards fulfillment
of the requirements for

Master's degree in Materials Science
and Engineering


Major professor

Date March 29, 2002

LIBRARY
Michigan State
University

PLACE IN RETURN BOX to remove this checkout from your record.
TO AVOID FINES return on or before date due.
MAY BE RECALLED with earlier due date if requested.

DATE DUE	DATE DUE	DATE DUE

**QUANTITATIVE AND ANALYTICAL HIGH-RESOLUTION TRANSMISSION
ELECTRON MICROSCOPY STUDY OF EPITAXIAL Co/Cu GMR MULTILAYERS**

By

John W. Heckman, Jr.

A THESIS

Submitted to

Michigan State University

in partial fulfillment of the requirements

for the degree of

MASTER OF SCIENCE

Department of Materials Science and Mechanics

2002

ABSTRACT

QUANTITATIVE AND ANALYTICAL HIGH-RESOLUTION TRANSMISSION ELECTRON MICROSCOPY STUDY OF EPITAXIAL Co/Cu GMR MULTILAYERS

By

John W. Heckman, Jr.

Co/Cu multilayers were grown on Nb layers by sputter deposition as part of an effort to develop a system for producing epitaxial multilayer (ML) devices for perpendicular to plane, giant magnetoresistance measurements (CPP-GMR). Epitaxial MLs and a polycrystalline ML were analyzed using conventional, analytical and high-resolution transmission electron microscopy. The Nb base layer observed was a single defect-dense crystal on the sapphire substrate. Apparently amorphous interfaces and non-equilibrium lattice structures were seen in one epitaxial ML. This sample also showed a overall Cu mass deficit. MLs In the other epitaxial specimens were broken into "island-like" regions associated with Cu seed-layer discontinuity. These epitaxial MLs had strata showing a crystal defect density like the Nb base and Co/Cu interlayer contrast. The polycrystalline sample was small grained and textured in the [111] growth direction. Co/Cu interlayer contrast in the polycrystalline ML and the epitaxial island MLs arises from stacking changes in Co.

ACKNOWLEDGMENTS

I firstly thank Dr. M.A Crimp, major professor, for inviting me to join his group and to pursue this program. Thanks also to the others on my committee Dr. D. Mason, and J. Bass. I also thank Drs. R. Loloee, and W.P. Pratt, Jr., for providing me with the sample multilayers and the GMR data. A special thanks also goes to Hong Geng, fellow graduate student, for essential help in preparing specimens of thin metal films on sapphire.

I also thank Drs. J.F. Mansfield and C. Wauchope of the University of Michigan EMAL for access to the JEOL 4000EX and 2010F (supported by grant number NSF DMR 987177).

This work has been supported by the Michigan State University Center for Fundamental Materials Research and by the National Science Foundation, through the Materials Research Science and Engineering Center MRSEC grant number NSF DMR 9809688.

TABLE OF CONTENTS

LIST OF TABLES	vii
LIST OF FIGURES.....	viii
CHAPTER 1 INTRODUCTION.....	1
1.1 Overview.....	1
1.2 Giant Magnetoresistance.....	2
1.3 Oscillatory Exchange Coupling and GMR ML devices.....	4
1.4 The Co/Cu ML system.....	6
1.5 Fabrication Considerations in Co/Cu GMR MLs.....	8
1.6 Epitaxial Co/Cu GMR MLs.....	13
1.7 Characterization of Magnetic MLs.....	15
1.8 Relevance of Previous Work to This Study.....	19
CHAPTER 2 EXPERIMENTAL PROCEDURES AND MATERIALS.....	21
2.1 Magnetron Sputtering and ML Device Fabrication.....	21
2.2 Co/Cu GMR ML Devices.....	21
2.3 CIP GMMR Measurements.....	26
2.4 TEM Sample Preparation.....	27
2.5 TEM Experimental Methods.....	30
2.6 TEM Image Analysis.....	33
CHAPTER 3 EXPERIMENTAL RESULTS.....	37
3.1 Sample 20-1 (epitaxial).....	37
3.2 Sample 20-2 (polycrystalline).....	56
3.3 Sample 20-3 (epitaxial).....	74

3.4 Sample 20-4 (epitaxial).....	87
3.5 Samples 91-3 and 19-4 (epitaxial bilayers).....	100
CHAPTER 4 DISCUSSION.....	116
4.1 Growth of the Nb Base layer.....	116
4.2 Cu Buffer Layers.....	119
4.3 Co/Cu Multilayers.....	123
CHAPTER 5. CONCLUSIONS AND RECOMMENDATIONS.....	128
LIST OF REFERENCES.....	132

LIST OF TABLES

Table 1.1 Physical Characteristics of the multilayer materials.....	16
Table 2.1 Co/Cu bilayer and GMR multilayer fabrication temperatures.....	24

LIST OF FIGURES

Figure 1.1. Schematics of the GMR effect and mechanism. A) The magnetoresistance of 3 Fe/Cr superlattices at 4.2K. The GMR effect was greater for thinner Cr (nonmagnetic) layers. The authors' current along the same [110] axis as the layers were grown (current in plane or CIP) [2]. B) A schematic of the GMR mechanism. Electron trajectories are represented by the straight segments, scattering by an abrupt change in direction [1].....	3
Figure 1.2. Oscillatory exchange coupling and its effect on ferromagnetic layer orientation. A) The effect of NM layer thickness on GMR [23]. B) The effect of the coupling on alternating FM and NM layers, with and without an external magnetic field.....	4
Figure 1.3. The relationship between number of bilayers and GMR observed with the current in the multilayer plane (redrawn from [14]).....	9
Figure 1.4. Proposed grain structures of Co/Cu MLs. A) Grown directly on a Fe seed layer with a thick Cu capping layer. B) Grown on a 35 nm Cu base layer From [30].....	10
Figure 1.5. The immiscibility of copper and cobalt. A) The binary phase diagram for Cu and Co [36]. B) The calculated free energy of mixing for Co and Cu [37].	12
Figure 2.1 Schematic cross-section diagrams of the test specimens. A) The Co/Cu GMR ML pattern. B) A preliminary Co/Cu bilayer sputtered on a Nb substrate.....	22
Figure 2.2 Schematics of ML stacking. A) Fcc Cu over bcc Nb in the Kurdjumow-Sachs orientation. B) The non-relaxed incoherent spacing between Co and Cu in the fcc crystal structure.....	25
Figure 2.3 The general CIP MR response in $\text{Co}_{6\text{ nm}}/\text{Cu}_{6\text{ nm}}$ [13].....	26
Figure 2.4. Schematic of the main steps in specimen cross-section preparation.	29
Figure 2.5 Objective apertures used in TEM imaging in the JEOL 4000EX. A) The CTEM aperture, a 7.2 nm^{-1} diameter. B) The Scherzer aperture, 20.8 nm^{-1} . The diffraction pattern is Si, $B=\langle 110 \rangle$ showing 36 transmitted beams (including the direct spot).....	30

Figure 2.6 The Sapphire/Nb boundary. The transform of this area shows that there is no detectable difference in the Nb {110} and sapphire {10 $\bar{1}$ 0} spacings. Thus Nb lattice images were used to calibrate the HRTEM images.....	35
Figure 2.7 Resolvable lattice planes and their interplaner angles for equilibrium structures of the elements used in the ML fabrication.....	36
Figure 3.1. CTEM images of sample 20-1. A) Brightfield minimum contrast focus image, normal to the sapphire (10 $\bar{1}$ 0). B) (200) Darkfield on the same axis. C) Over-focused brightfield image showing Fresnel contrast parallel to the layer interfaces.....	37
Figure 3.2. Multibeam (HRTEM) approximately Scherzer focus images and average density plots along MLs. A) Sample 20-1. B) Sample 20-2. C. Sample 20-4.....	37
Figure 3.3. HRTEM image of a selected region of sample 20-1. The growth direction is about 30° off the depicted vertical. The three regions selected for lattice image analysis are indicated.....	41
Figure 3.4 An HRTEM image of the upper layers in sample 20-1. This figure is oriented with the growth direction running vertically. The top dark region is the capping Nb layer. The insets are areas that were tested by FFT analysis.....	42
Figure 3.5 Selected HRTEM images A-F and their FFTs from the upper layers of sample 20-1.....	43
Figure 3.6 HRTEM image of the middle layers in sample 20-1. This figure is oriented with the growth direction running vertically.....	46
Figure 3.7. Selected HRTEM images A-F and their FFTs from the middle layers of sample 20-1.....	48
Figure 3.8. HRTEM image of the bottom layers in sample 20-1. This figure is oriented with the growth direction running vertically. The lowermost area, F, is the bottom Nb layer.....	49
Figure 3.9. Selected HRTEM images A-F and their FFTs from the bottom layers of sample 20-1.....	50
Figure 3.10. EDS spectra from a cross-section the 20-1 ML structure. A) The spectrum formed by averaging three whole-ML spectra. B) DTSA simulation of a Co/Cu sample with the same volume fractions as a circular sample of the 20-1 ML motif.....	54

Figure 3.11. EDS spectra from a cross-section the 20-1 ML structure. A) The spectrum formed by averaging 18 Cu layer spectra. B) The spectrum formed by averaging 18 Co layer spectra.....	55
Figure 3.12. CTEM images of sample 20-2. A) Single beam brightfield image of a cross section of the 20-2 ML. B) The darkfield image created using the (0 $\bar{1}$ 0) Nb spot. C) A single-beam brightfield image taken 11 μ m below minimum contrast.....	57
Figure 3.13. Low magnification HRTEM image of the cross-sectioned 20-2 sample. The ML area (ML) and lattice analysis area (inset) are shown.....	59
Figure 3.14. HRTEM of the ML 20-2. Four regions were selected for lattice analysis of the metal layers. Based on crystal diffraction contrast there appears to be 5 rather than 6 bilayers.....	60
Figure 3.15. HRTEM of the upper region of sample 20-2. The image corresponds to the inset (1) from figure 3.14. The upper half of the region is the Nb capping layer.....	62
Figure 3.16. HRTEM of the middle region of sample 20-2. The image corresponds to the inset (2) from figure 3.14.....	63
Figure 3.17. High magnification HRTEM areas and their corresponding FFT transforms from Figures 3.15 (A-C) and 3.16 (D-F).....	64
Figure 3.18. HRTEM of the first Co and adjacent Cu layers from sample 20-2. The area corresponds to the inset (3) from figure 3.14.....	67
Figure 3.19. High magnification HRTEM areas and their corresponding FFT transforms from Figures 3.18 (A-C) and 3.16 (D-F).....	68
Figure 3.20. HRTEM of the Cu buffer layer and adjacent Nb base layer from sample 20-2. The area corresponds to the inset (4) from figure 3.14.....	70
Figure 3.21. High magnification HRTEM areas and their corresponding FFT transforms from Figures 3.19 (A-C) and 3.16 (D-F).....	71
Figure 3.22. EDS spectrum from a cross-section of the 20-2 ML structure.....	72
Figure 3.23. CTEM images of sample 20-3. A) Single beam brightfield image of a cross section of the 20-3 ML. B) The darkfield image obtained with the Nb (0 $\bar{1}$ 0) reflection. C. A single-beam brightfield image focused 11 μ m below the minimum contrast setting. Arrows 1-4 highlight a prominently layered region, an anomalously thick buffer region, a region apparently <i>sans</i> buffer layer and an apparent hole, respectively.....	74

Figure 3.24. CTEM image of the cross-sectioned 20-3 sample. A) An area within an island. B) The area around an apparent hole.....	77
Figure 3.25. HRTEM image of an island area of 20-3 selected for structural analysis. Areas A-F are representative areas of the upper and lower Nb layers and the first and last Co/Cu bilayers.....	78
Figure 3.26. High magnification HRTEM areas and their corresponding FFTs from areas A-F in Figure 3.25.....	79
Figure 3.27. High magnification HRTEM areas and their corresponding FFTs from areas G-J in Figure 3.25.....	81
Figure 3.28. A HRTEM image of a Cu buffer layer hole and surrounding area from sample 20-3.....	83
Figure 3.29. High magnification HRTEM images and their corresponding FFTs. from areas around the hole shown in Figure 3.28.....	84
Figure 3.30. CTEM images of sample 20-4. A) Single beam brightfield image of a cross section of the 20-4 ML. B) The darkfield image obtained with the Nb (0 $\bar{1}$ 0) reflection. C) A single-beam brightfield image focused 11 μ m below the minimum contrast setting. Arrows 1-3 highlight: A region apparently <i>sans</i> buffer layer, an apparent hole, and a prominently layered region, respectively.....	88
Figure 3.31. Low magnification HRTEM image of the cross-sectioned 20-4 sample. The area within a typical island chosen for structural imaging is outlined.	90
Figure 3.32. HRTEM image of an island area of 20-4 selected for structural analysis. Areas A-M are representative areas throughout Co/Cu bilayers.....	91
Figure 3.33. High magnification HRTEM areas and their corresponding FFTs from areas A-F in Figure 3.32.....	92
Figure 3.34. High magnification HRTEM areas and their corresponding FFTs from areas G-M in Figure 3.32.....	95
Figure 3.35. An EDS spectrum collected from the whole ML cross-section of sample 20-4. The collection time and beam parameters were essentially the same as those used previously.....	96
Figure 3.36. An EDS spectrum from the top amorphous layer covering the ML	96
Figure 3.37. EDS spectra from adjoining Cu and Co layers near the top of the ML. A) A Cu layer and B) a Co layer.....	98

Figure 3.38. An EDS spectrum from the Cu buffer layer of sample 20-4.....	99
Figure 3.39. Brightfield CTEM cross-section images of samples 19-3 and 19-4. A) Sample 19-3. B) Sample 19-4. C. An island structure from sample 19-4 showing three regions analyzed via HRTEM.....	102
Figure 3.40. HRTEM overview of the "inset 1" area of Figure 3.39C. Six representative areas were selected for lattice image analysis.....	104
Figure 3.41. High magnification HRTEM areas and their corresponding FFTs from areas A-F in Figure 3.40.....	105
Figure 3.42. HRTEM overview of the "inset 2" area of Figure 3.39C. The three inset areas and their FFTs are also shown.....	108
Figure 3.43. HRTEM overview of the "inset 3" area of Figure 3.39C. Six representative areas were selected for lattice image analysis.....	110
Figure 3.44. High magnification HRTEM areas and their corresponding FFTs from areas A-F in Figure 3.43.....	111
Figure 3.45. HREDS spectrum from the Co layer on an island from sample 19-4	113
Figure 3.46. An HREDS spectrum from the thicker (A) and thin (B) middle areas of the Cu layer on a island from sample 19-4.....	113
Figure 3.47. An HREDS spectrum from the "gap" area in an island from sample 19-4.....	114
Figure 3.48. An HREDS spectrum from the Cu Nb interface at the base of an island from sample 19-4.....	114
Figure 4.1. Binary phase diagrams. A) Co-Nb. B) Cu-Nb. Below 800°C there should be no solubility of Nb in Cu.....	120
Figure 4.2 Atomic force microscope images of 20 nm Cu layers grown on the surface of 250 nm epitaxial Nb layers. A) Deposited at 350°C. B) Deposited at 150°C and annealed at 350°C for 10 min. From [47].....	122

CHAPTER 1 INTRODUCTION

1.1 Overview:

In the last decade great progress has been made in the application of thin-film multilayer technology. Nowhere has this development been more apparent than in the area of thin-film giant magnetoresistance (GMR) devices. The operation of these devices is based on the property that certain layered structures, containing a ferromagnetic/nonmagnetic/ferromagnetic layer motif, display a great change in electrical resistance upon the application of an external magnetic field. Magnetic random access memory (MRAM), GMR read heads, and magnetic position sensors are commercial examples of the application of this technology.

Improvement and development of this technology will depend on the refinement of the knowledge of the effects of the physical characteristics of the magnetic and non-magnetic materials used on the resultant magnetic properties. For example, an early discovery towards the facile production of these devices was that GMR devices readily be made in high throughput sputtering devices. Already a wealth of information exists describing the effects of elemental choice, crystal orientation and size within the films, interfacial roughness and intermixing on the GMR response. Developing fabrication protocols for single crystal epitaxial structures is currently an important area of investigation. In this thesis, the results of experiments aimed at the development of such protocols are evaluated by transmission electron microscopy (TEM) techniques. For preliminary work, a well characterized and technologically applicable Co/Cu multilayer was chosen. Examples were sputtered under varying temperatures and annealing treatments

to develop epitaxial model systems for GMR studies. The focus of this investigation was the crystallographic and compositional characterization of these examples, at the atomic level, and their comparison to similar polycrystalline preparations.

1.2 Giant Magnetoresistance:

One of the factors influencing electrical resistance in metals is the magnetic condition of the medium. Giant magnetoresistance (GMR) refers to an anomalously high resistance to electrical current passage through some materials, as a consequence of their magnetic order [1]. This resistance can be greatly reduced through the application of an external magnetic field (Figure 1a).

The GMR effect was first observed by the independent groups of A. Fert [2], in France, and P. Gruenberg [3], in Germany. These groups noticed a drastic reduction of electrical resistance in the plane of ultra-thin Fe/Cr multilayers (MLs) in the presence of an externally applied magnetic field. This effect was far greater than the angularly dependent change seen in a single magnetic layer (anisotropic magnetoresistance effect). Under the application of the external field, the magnetic moments of the thin ferromagnetic layers change from their minimum energy configuration, having their magnetic moments aligned antiparallel to each other (*i.e.* antiferromagnetically coupled), to the parallel condition. The MR effect stems from the spin dependence of the electron conduction in the ferromagnetic layers. In the two-current model for conduction in ferromagnets, two current channels + and - (from spins of $+1/2$ and $-1/2$ on

an absolute axis) are considered. These correspond to \uparrow and \downarrow , the majority and minority spin directions in the ferromagnetic layers,

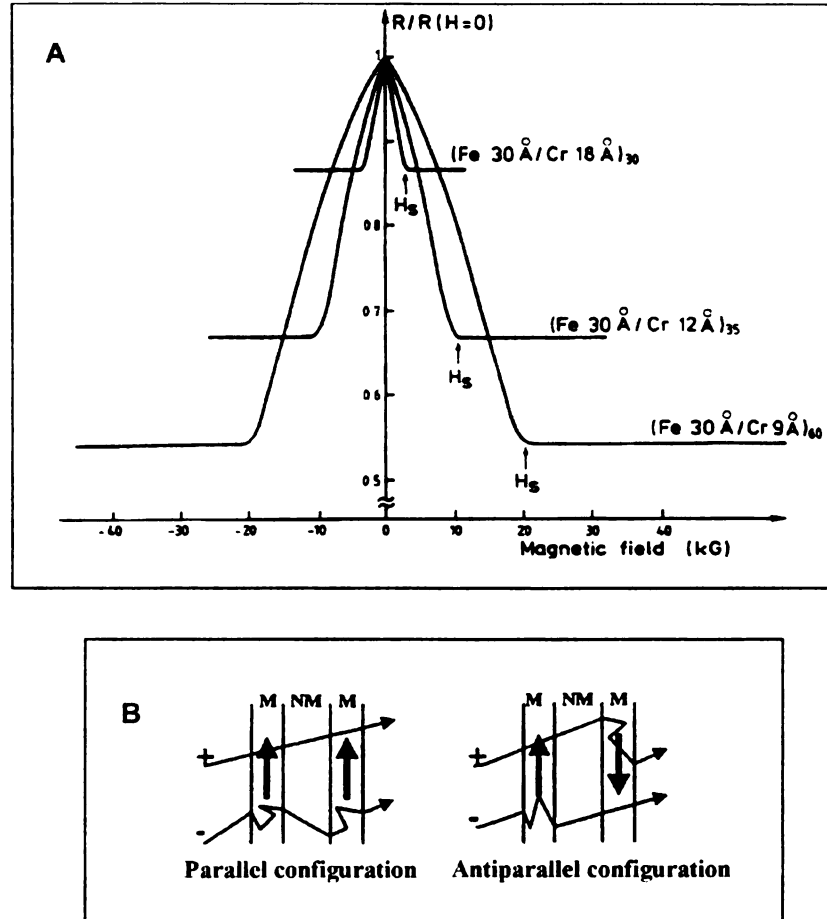


Figure 1.1. Schematics of the GMR effect and mechanism. A) The magnetoresistance of 3 Fe/Cr superlattices at 4.2K. The GMR effect was greater for thinner Cr (nonmagnetic) layers. The authors applied the current long the same [110] axis as the layers were grown (current in plane or CIP) [2]. B) A schematic of the GMR mechanism. Electron trajectories are represented by the straight segments, scattering by an abrupt change in direction [1].

The resistivity in the ferromagnetic material can be expressed as a function of the resistivities of each electron channel:

$$\rho = \frac{\rho \uparrow \rho \downarrow + \rho \uparrow \downarrow (\rho \uparrow + \rho \downarrow)}{\rho \uparrow + \rho \downarrow + 4\rho \uparrow \downarrow} \quad (1)$$

The orientations of the magnetism in the ferromagnetic layers either promotes or inhibits the mobility of the electron through the layer stack (Figure 1b).

The final *resistance* in the parallel state ML r_p can be written as:

$$r_p = \frac{r_+ r_-}{r_+ + r_-} \quad (2)$$

and that in the antiparallel configuration (r_{AP}) as:

$$r_{AP} = \frac{r_+ + r_-}{4} \quad (3)$$

The percent change in resistance between the two states is the GMR:

$$GMR = \frac{r_{AP} - r_p}{r_p} \times 100 \quad (4)$$

This is the form generally reported in the literature [1].

1.3 Oscillatory Exchange Coupling and GMR in multilayer devices:

In MLs, consisting of alternating layers of non-magnetic (NM) and ferromagnetic (FM) materials, the degree of exchange coupling in many systems oscillates with variation in NM layer thickness, (Figure 2a), rather than decaying monotonically with NM layer thickness [3]. The exchange coupling (the ability of one magnetic domain to affect the alignment of another) in these layers promotes a concomitant thickness dependent GMR effect [4, 5].

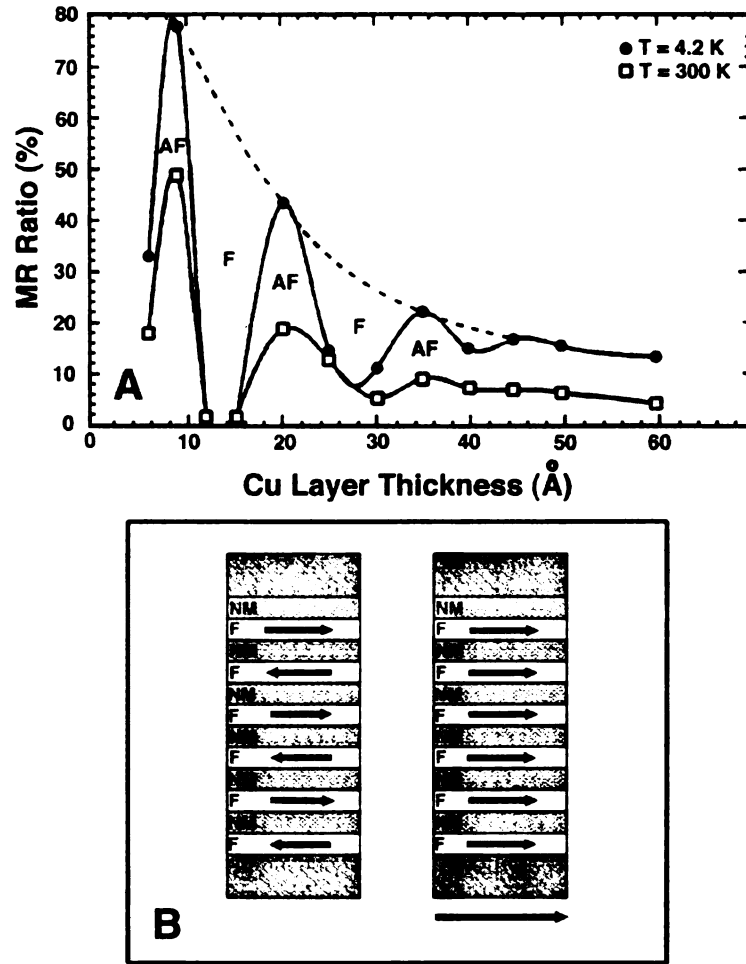


Figure 1.2. Oscillatory exchange coupling and its effect on ferromagnetic layer orientation. A) The effect of NM layer thickness on GMR [23]. B) The effect of the coupling on alternating FM and NM layers, with and without an external magnetic field.

Thus, the magnetizations of alternating ferromagnetic layers will exist in the maximum antiferromagnetic (AF) configuration only if the interleaving non-magnetic layers are of certain thicknesses. The magnitude of the antiferromagnetic coupling is also dependent on (among other attributes) the thickness of these NM layers and a decreasing effect can be seen as a damped oscillating response in the GMR of the ML. This effect is seen in FM/NM MLs for a number of elemental systems. Although the GMR effect appears to be the

highest for relatively thin NM layers (ca. 1nm), the GMR effect is evident even in Co/Cu MLs having NM layer thicknesses as great as 50nm [6].

With the ability to switch the magnetic order with an externally applied field, materials exhibiting the GMR effect have progressed from the realm of experimental novelties to engineering materials [e.g. 7,8]. The sensitivity of a GMR device to an external field can be improved in at least two ways. Highly sensitive structures, known as exchange biased spin valves, can be made by pinning the orientation of one ferromagnetic layer with an antiferromagnetic material while leaving another to rotate in the applied field. These are currently being used in sensor applications such as read-head devices for high-density disk drives and non-volatile, magnetic memory devices (MRAM) [8]. Second, by using a soft-magnetic adjacent layer (e.g. Vitrovac™ 6025, a Co based metallic glass) the low field sensitivity of a simple ML, such as the Co/Cu motif, can be greatly enhanced [9]. The various applications of thin-film GMR devices for engineering materials share the common requirement of a precisely fabricated ML metallic structure.

1.4 The Co/Cu multilayer system:

Early in the exploration of the GMR effect, Parkin, *et al.* [10] tested a number of ML superlattices for oscillatory exchange coupling that promotes the GMR effect. The system that possessed the highest GMR values was a configuration of alternating Co (ferromagnetic) and Cu (non-magnetic) layers [11]. This system has yielded the highest room-temperature magnetoresistance (65% at 295 K and 120% at 4.2 K) of any such superlattice and is still of research interest [12,13].

The Co/Cu system does have a high saturation field which limits its utility in certain applications. The incremental change in resistance in these systems decreases with increasing field strength. However, the change in resistivity (and therefore GMR) continues to increase for fields two orders of magnitude greater than the magnetic saturation field and the GMR effect increase towards a limit with bilayer number (Figure 1.3).

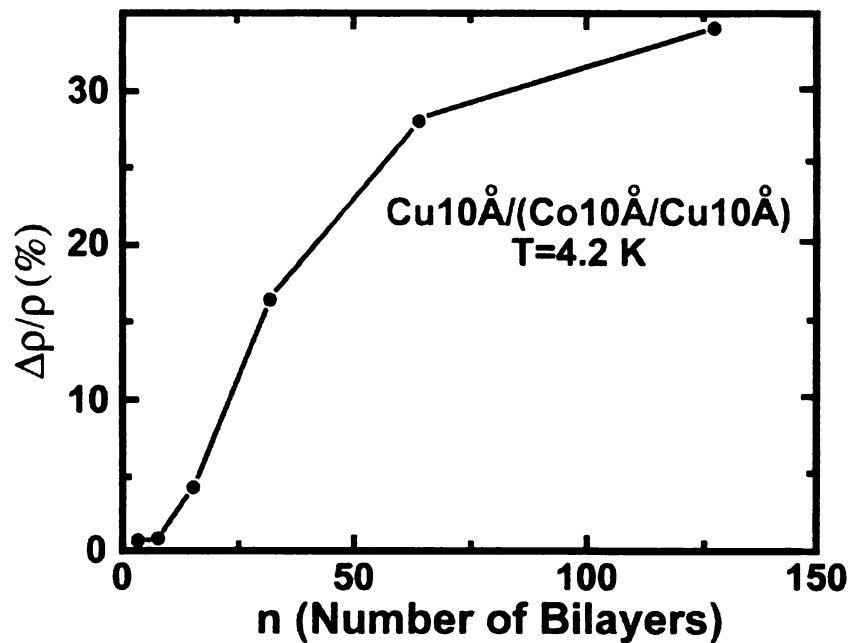


Figure 1.3. The relationship between number of bilayers and GMR observed with the current in the multilayer plane (redrawn from [14])

This may be due to a degree of Co disorder at the higher layer number interfaces that contributes significantly to the electron scattering but not much to the magnetism at higher fields [14]. Copper/cobalt MLs have been prepared on a number of different substrate types and by several methods. The first Co/Cu magnetic ML examples were deposited on single crystal copper via electron-

beam evaporation [15,16], while others have used a similar evaporation techniques to build the MLs on oxidized silicon [17] and metal-sliced substrates [18]. Another approach has been molecular beam epitaxy (MBE) [e.g. 19-22]. However, probably due to the faster growth rate and economics, the vast majority of preparations have been made with various sputtering systems [e.g. 23-27]. More recently, pulsed electrodeposition (plating) techniques have been used [28].

1.5 Fabrication considerations in Co/Cu GMR multilayers:

To be useful as a model or as an engineering material, the behavior and stability of a ML system during fabrication and in subsequent application needs to be known. Aside from representing materials with the appropriate ferromagnetic and non-magnetic properties, the more fundamental metallurgical characteristics of the Co/Cu system and its substrates are important. Obviously, layer thickness is important as evidenced by the oscillatory exchange coupling. As can be seen in Figure 1.2, the AF period is about 1.0 nm and an additional ± 0.5 nm in the NM layer thickness could destroy the GMR effect. As mentioned above, the number of bilayers also is an important characteristic. For a Co_{1 nm}/Cu_{1 nm} bilayer system, the GMR effect appeared to grow to a finite maximum with the number of bilayers (Figure 1.3). Thus, the ability to confirm layer geometry and quality is important.

A second consideration in the fabrication of MLs is the effect of crystallographic orientation and grain size on the GMR effect. Earlier work by Cebollada, *et al.* [16] found that there was significant AF coupling in Co/Cu (100)

layers grown by MBE on Cu (100). Others found that the response was absent in MBE Co/Cu MLs grown on Cu (111) [22,29], leading to the speculation that the (100) grains in the sputtered examples were related to the GMR effect [29]. However, Parkin, *et al.* [6] found that there was significant AF coupling in a system of Co/Cu MLs grown in a highly <111> texture on Pt buffer layers deposited on (0001) sapphire. They suggested that the absence of AF coupling seen in other <111> preparations, including those grown epitaxially on GaAs, may be a result of structural imperfections. Greig, *et al.* [19] found that the GMR in <111> epitaxial films grown on GaAs was highly dependent on the seed / buffer layer. Their low angle X-ray data also show strikingly more distinct layers when the buffer layer was Au rather than Cu. In a sputter deposited system, Modak, *et al.* [30] found that by changing the order of growth larger single crystals could be grown through a ML stack (short range epitaxy, Figure 1.4).

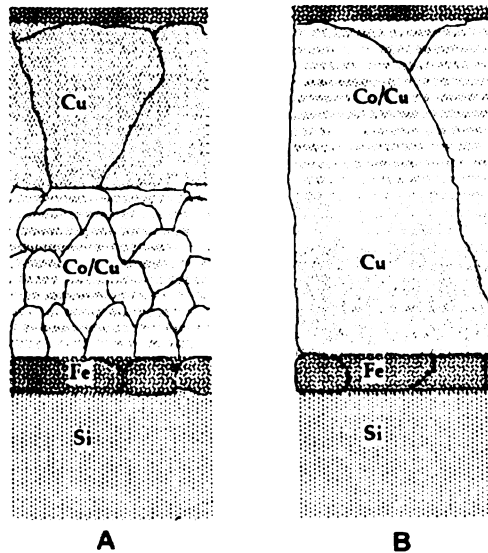


Figure 1.4. Proposed grain structures of Co/Cu MLs. A) Grown directly on a Fe seed layer with a thick Cu capping layer. B) Grown on a 35 nm Cu base layer. From [30]

Films grown on a 35 nm Cu buffer layer had larger crystals and exhibited about 42% higher GMR than similar MLs grown directly on the Fe seed layer (with the 35 nm Cu layer deposited on the top of the ML stack. Their TEM data also show considerably larger single crystal domains in the Co/Cu ML when grown on the thick Cu buffer layer.

The interfacial quality of the ML is a fabrication consideration that can also be important in the GMR response. One of the variables in the interface quality is roughness. There have been conflicting reports concerning the effect of interfacial roughness on the GMR response. For example Chládek, *et al.* [31] mention that the increased GMR seen in post deposition annealed systems is due to roughness caused by partially broken MLs. In a study of the effect of post deposition annealing, Rätzke, *et al.* [25] found that a 30 min anneal at 350°C caused a layer break-up that was associated with an increased coercivity and an initial increase in GMR. They consider the annealing effect to be one of lowering crystallographic defects while also causing the break-up of the Co layer into smaller domains. An annealing effect was also seen in Co/Cu multilayers, of varying Cu thickness, grown on glass substrates. In this study post deposition annealing over a range of Cu layer thicknesses, lead first to a slight increase in MR then a monotonic decrease. This was ascribed to the resolution of crystal defects , in the first part of the annealing, then to a decrease in MR with grain size increase [32]. On the other hand, Miura, *et al.*, [20] have demonstrated a sharp drop in GMR with the increase of interfacial roughness in Co/Cu ML systems. An imperfection related to layer break-up is in the form of "pinholes" in

the Cu layers. These ferromagnetic material "channels" can easily happen in the thin (ca. 1 nm) layers near the first AF peak and the theoretical maximum AF exchange can be masked. Thus, the GMR is affected by FM coupling through these defects [33].

Plaskett and McGuire [14] found that GMR increased rapidly at first then with a diminishing rate with the number of layers. They postulate that, as roughness increases with higher layer number, the electron scattering caused by these rough high-order layers dilutes the overall GMR effect. This is supported by *in-situ* X-ray diffraction analysis of a Permalloy / Ag ML system during fabrication in [31], where it was found that interfacial roughness increased with layer number. Kubinski, *et al.*, present micrographs showing a slight serial increase in interfacial roughness in a 16 bilayer stack (in another system) deposited on a Ru buffer over an oxidized Si substrate [35]. However, in Co/Cu and a Co/ Cu_x - Au_{1-x} systems [34], TEM images of specimen cross-sections show no discernable increase in roughness with layer number. Lastly, in an electrodeposited system [28], the final surface roughness decreased at higher layer number.

Interdiffusion is a ubiquitous concern in thin films in general [36]. For sensor applications, the inter-diffusion rates between elements forming separate layers, having distinct functions, are crucial concerns. Elements that have similar crystal structures and lattice parameters generally form solid solutions [37]. However, copper and cobalt are immiscible at temperatures below 422°C [38] and the associated positive heat of mixing [39] should promote highly stable interfaces (Figure 5). Nevertheless, the formation of ordered interdiffused regions has been

reported [40] in Co/Cu systems. However, in other studies involving annealing, coalescence leading to breakdown of the Co/Cu ML rather than diffusion has been reported. This coalescence is implied by a decrease of saturation magnetization field [12] and the presence of what appears to be Cu migrating along Co grain boundaries as seen in TEM images [25]. Diffusion and/or reactions with certain substrates has also been reported in GMR MLs [18,25].

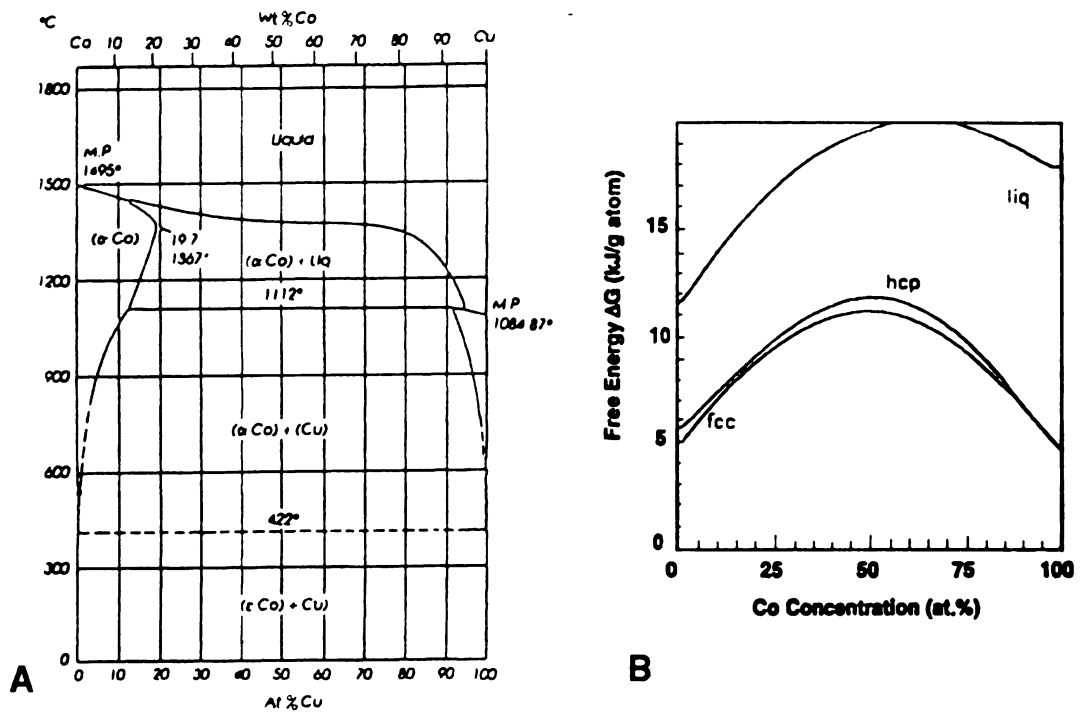


Figure 1.5. The immiscibility of copper and cobalt. A) The binary phase diagram for Cu and Co [38]. B) The calculated free energy of mixing for Co and Cu [39].

Reactions with Si substrates leading to the formation of silicides has been reported and used to form a basis for epitaxial growth [18].

1.6 Epitaxial Co/Cu GMR MLs:

Although the GMR effect was first seen in MBE grown MLs, most of the work in the Co/Cu system has been done with polycrystalline sputter deposited samples. However, epitaxially grown Co/Cu MLs have also been prepared by sputtering [e.g. 41]. The possibility of producing a more homogenous medium through the fabrication of single crystal (*i.e.* epitaxially grown) layers in GMR devices was early recognized as an intriguing approach for (at least) experimental modeling [e.g. 6]. In polycrystalline Co/Cu MLs, involving identical GMR layer stacks grown with differing crystallinity, Modak, *et al.* [30] found that the CIP GMR showed a distinct increase (about 42%) with a grain size increase from about 15 to 35 nm. These data may appear contradictory to the results of Tomlinson, *et al.* who reported an increase in GMR with *decreasing* crystal size [24]. However, in the large crystal samples of Modak, *et al.*, the film was <111> textured and the large grains were usually epitaxial [30]. Early on, single crystal epitaxial superlattices of Co/Cu had been grown using a single crystal Cu (100) substrate [15], however this was accomplished by electron beam evaporation. Sputtering systems are the practical method of choice in many thin-film fabrication endeavors owing to their higher deposition rate, lower capital and operation costs [36]. Co/Cu superlattices with large epitaxial areas have been grown on MgO (110) and (100) substrates using Pt or Pd as a seed layers and on sapphire (0001) using Pt as a seed layer [41]. Epitaxial growth in the Co/Cu

ML system has been shown to be highly dependent on the initial composition, dimensions, and structural quality of the initial layer and thus on the deposition conditions. The copper-cobalt system should be amenable to the formation of such epitaxial layers. Although the equilibrium structure of copper is fcc and cobalt is predominately hcp, cobalt can also will exist as an fcc structure and this is generally the form that has predominated when Co thin films are grown on Cu in MLs [e.g. 30,42].

The discovery of the GMR effect and most subsequent GMR measurements have been done by measuring the ΔR along the planes of the ML. Sensitive measurement of the GMR effect, especially for experimental purposes, is more effective in the current perpendicular to plane (CPP) geometry [43,44]. Superconducting Nb contacts are fabricated on top and bottom of the specimen since the resistances are very small in this geometry [43]. Nb is the contact material of choice for measurements in this temperature range due to its relatively high (9.5 K) superconducting behavior, which remains intact well above the He boiling point even in the presence of a strong magnetic field. The GMR across the sample is then measured using a superconducting quantum interference device magnetometer (SQUID) with a sample measuring temperature of 4.2 K.

The epitaxial growth of Nb on sapphire is quite facile, with the (110) planes of Nb growing epitaxially on the $(1\ 1\ \bar{2}0)$ of sapphire [45] with the Nb atomic lattice patterning on the Al atoms of the sapphire. Extended Nb single crystals have been made in this orientation by sputtering the Nb on heated single crystal sapphire [44] substrates followed by a post deposition annealing treatment. The

thermal expansion coefficients of the two materials are similar (Table 1.1) and a smooth-surfaced Nb layer is retained after cooling. The misfit between the Nb and the sapphire has been explored for a number of orientations and the lattice strain is accommodated by a network of dislocations [47-50]. However, the mismatch between the Nb and the Cu of the next deposited layer is more severe. The mismatch between the Nb (110) surface and the close packed planes of Cu (111) is accommodated with a Kurdjumov-Sachs orientation relation [46,51]. The fcc form of Co and Cu have a lattice mismatch of less than 2% that appears to be elastically accommodated in epitaxial thin films.

1.7 Characterization of magnetic MLs:

To correlate the structural concerns outlined above with device performance and predict their theoretical significance, unambiguous characterizations are desired. However, there is no one technique that provides a comprehensive measurement of all of the important characteristics of ML structures. For GMR MLs, low angle ($2\theta < 10^\circ$), and high angle ($2\theta > 10^\circ$) X-ray diffraction of the fabricated ML are attractive methods. Both can be accomplished during the thermal annealing steps of the fabrication process [e.g. 31].

Low angle scans of ML devices are a rapid and nondestructive means of characterizing the layer frequency, overall texture, and crystal structure. High angle diffraction can be used to obtain the crystal structure, orientation (texture), and average grain size. The rapid through-put and non-destructive nature of this technique has made it the most commonly used characterization technique [1, 37]

Table 1.1 Physical Characteristics of the multilayer materials

Material Characteristic	Al₂O₃ (sapphire)	Nb	Cu	α-Co	β-Co
structure	corrundum	bcc	fcc	hcp	fcc
Strukturbericht	D5 ₁	A2	A1	A3	A1
space group	167	229	225	194	225
point group	R-3c	Im3m	Fm3m	P63/m m c	Fm3m
lattice parameters	a=0.4763 c=1.303	a=0.3307	a=0.3615	a=0.2507 c=0.4070	a=0.3544
Atomic number (Z)	-	41	29	27	27
melting point	2030°C	2477°C	1085°C	1495°C	1495°C
coefficient of expansion	a=5.0 x 10 ⁻⁶ c= 9.03 x 10 ⁻⁶	7.2-7.6 x 10 ⁻⁶	17.0-18.3 x 10 ⁻⁶	12.1-14.0 x 10 ⁻⁶	12.1-14.0 x 10 ⁻⁶

Nuclear magnetic resonance (NMR) is a second technique that has yielded important structural information in multilayers [21,42]. By comparing the resonance frequency (the frequency causing nuclear spin flipping) in a pulsed, variable-frequency electromagnetic field, a spectrum of echo frequency maxima is generated. These resonance frequencies are dependent on the environment of the lattice atoms and, by comparisons to standards, the atomic environment (crystal structure) of the atoms can be determined. The low frequency signal can also give a measure of surface roughness in terms of Co nearest neighbors.

Reflection high energy electron diffraction (RHEED) is a diffraction technique that involves the use of grazing incident electron waves to probe the surface layers of the target. RHEED patterns are especially useful in determining the

quality of layer surfaces. RHEED is a non-destructive technique and has the advantage of being applicable during the film growth process. RHEED devices are *de rigueur* in commercial MBE systems and as such are the most common film qualifying technique for MBE epitaxial studies [e.g. 19.]

Scanning electron microscopy (SEM) generally has not the resolution or penetration to yield much information on completed devices. However, SEM with polarization has been used to characterize both the crystalline and magnetic structure of sputtered Co/Cu MLs [13]. SEM is also useful in the crystallographic orientational analysis of MLs component by component [45] via electron back-scatter diffraction (EBSP) techniques. Automated indexing systems allow relatively large areas to be mapped for crystal orientation.

Transmission electron microscopy (TEM) of cross-sectioned materials has also proven useful. Ordinary diffraction contrast can be used to differentiate between thin metal layers in establishing layer dimensions normal to the electron beam. This process is straightforward for materials with significantly different elastic cross sections and for differences on the order of Nb or Ag and Cu or NiFe ($\Delta Z \approx 17$) [41, 54]. However, in the case of the layers in the Co/Cu system, there is little differential scattering contrast due to closeness of atomic numbers ($\Delta Z = 2$). One approach that has been used to delineate overall layer quality in such systems is Fresnel defocus contrast [25, 28]. This technique makes use of differences in the mean inner potential of the two materials (which is a function of their densities and forward scattering factors) to generate focus sensitive interference images. This interference is seen as a band of contrast change at

the interface between regions with differing mean inner potentials [51,52]. Such techniques allow the quantitative analysis of layer interfaces by evaluation of the focus dependent fringe amplitude.

High resolution transmission electron microscopy (HRTEM) pushes the resolution of the TEM to the atomic level. HRTEM allows crystallographic details of such features as crystal defects, layer interfaces, local non-equilibrium structures and grain boundaries to be explored at the lattice level [32,41,54]. Extraction of periodic information from HRTEM micrographs has long been enhanced by the use of optical diffraction techniques [55]. Sinclair, *et al.* [56] have presented extensive analysis of metal lattice images and note that the technique allows the extraction of crystal orientation and local lattice variations from very small areas of the HRTEM micrograph, giving spatial resolution far better than practical with electron diffraction techniques. Combining HRTEM of metal foils with image analysis via computer generated fast Fourier transformation (FFT) allows rapid quantitative crystallographic analysis of regions a few square nanometers from HRTEM lattice images [e.g. 54].

In the latest, intermediate-voltage field-emission analytical electron microscopes (AEM)s, spatial analytical resolution has decreased to the nanometer or smaller scale in the past few years. This allows the near atomic level detection of individual metal ions [57]. Surprisingly few GMR ML systems have been studied using AEM [e.g.56]. AEM coupled with high resolution imaging, which is increasingly important in the study of magnetic MLs, can provide corroborative independent data for structural model testing [53].

1.8 Relevance of Previous Work to This Study:

Considerable work has been done on the preparation, GMR characterization, and structural analysis of variously prepared Co/Cu ML systems. Conflicting results appear with respect to the effects of a number of structural variables on the final device performance. It has been noted that, for a number of fabrication techniques and structures, the preparation of uniform material with known magnetic transport properties can be somewhat site (*i.e.* investigator) specific [35, 37].

Epitaxial Co/Cu MLs have been fabricated by a number of groups. The current study concerns the epitaxial growth of metal MLs like those used in GMR devices, using the Co/Cu system as a model, between the Nb contacts required for CPP measurement. The formation of an initial epitaxial layer is crucial to the subsequent ML development. Recent work [46] has confirmed that sputter deposited Nb will grow epitaxially on a $(1\ 1\ \bar{2}\ 0)$ sapphire surface. Samples with extensive layers of Nb contact metal outside of the ML device to be tested make CIP GMR measurement difficult due to the dilution effect of current through these layers. However, preliminary qualitative comparative CIP GMR measurements on epitaxial Co/Cu MLs revealed values much lower than the similarly configured polycrystalline sample. It was important to determine the degree of epitaxi in these samples. Possible structural correlations between the GMR observations and comparisons to the polycrystalline sample were also sought. In the present study, an initial series of 3 nominally identical epitaxially-grown Co/Cu MLs were analyzed. A second Co/Cu ML, of identical layering dimension, was fabricated

during the same production run, with the entire deposition conducted at room temperature. This provided a polycrystalline sample for comparison. Previously, CTEM has been used mainly to qualitatively analyze Co/Cu ML systems [e.g. 25-28]. HRTEM has shown numerous short-range crystal defects exist in Co/Cu systems [30,41]. Given the importance of structure, on many scales, to the performance and of Co/Cu GMR devices, CTEM, HRTEM and HREDS were used to analyze the structure and composition of the samples. The resulting information should help to determine the fabrication variables to be considered in attempting to increase the precision of epitaxial growth of GMR ML devices.

CHAPTER 2 EXPERIMENTAL PROCEDURES AND MATERIALS

2.1 Magnetron sputtering ML device fabrication

The GMR ML devices investigated in this study were fabricated by Dr. Reza Loloee in the MSU Department of Physics and Astronomy. The detailed features of the fabrication system has been described elsewhere (60). Briefly, an UHV compatible DC-magnetron sputtering system, with multiple sputtering heads, was used to apply alternating metal layers on $(1\ 1\ \bar{2}\ 0)$ surfaces of Al_2O_3 single crystal coupons (Union Carbide). Prior to film deposition, the sapphire surfaces were washed with hot water/surfactant (Alconox) followed by serial rinses in acetone, ethanol and de-ionized water. Cleaning was carried out in a class 1000 clean room adjacent to the sputtering facility. The sapphire substrates received an additional IR absorbing Nb coating (200 nm) on the back surface, prior to device fabrication, to help maintain the temperature during deposition. Nominal thicknesses of the layers were determined by timing of the sputtering process. The timing was based on the independent analysis, by profilometry and atomic force microscopy, of previously sputtered films. Up to four samples were prepared in a single system pump-down (Base pressure = 2×10^{-8} T).

2.2 Co/Cu GMR ML devices

The four GMR ML samples (Figure 2.1) of the nominal form sapphire/ $\text{Nb}_{250\text{ nm}}$ / $\text{Cu}_{20\text{ nm}}$ ($\text{Co}_{6\text{ nm}}$ / $\text{Cu}_{6\text{ nm}}$) $\times 6$ / $\text{Nb}_{100\text{ nm}}$ investigated here were fabricated in a single vacuum cycle in the apparatus described above. In addition, two single bilayer samples of the form sapphire/ $\text{Nb}_{250\text{ nm}}$ / $\text{Cu}_{20\text{ nm}}$ / $\text{Co}_{20\text{ nm}}$ fabricated in a prior run, as fabrication trials, were prepared for TEM.

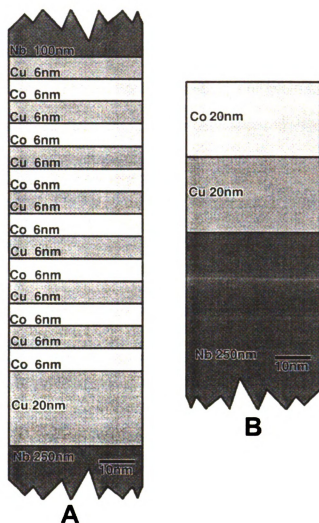


Figure 2.1 Schematic cross-section diagrams of the test specimens. A) The Co/Cu GMR ML pattern. B) A preliminary Co/Cu bilayer sputtered on a Nb substrate.

The GMR ML samples, serially fabricated, were denoted as 20-1, 20-2, 20-3 and 20-4. The two preliminary bilayer samples were 19-3 and 19-4. The growth conditions for the MLs and bilayers examined are listed in Table 2.1.

In all samples, the first layer deposited was a nominally 250 nm thick Nb base layer equivalent to that which is required for superconducting contacts in EBSVs.

This film was deposited on the pre-annealed $(1\ 1\ \bar{2}0)$ surface of the sapphire.

Ideally, in the coherent areas, the Nb (110) planes align with the Al atoms in the sapphire. The generation of epitaxial growth is dependent on the establishment of a suitable seed or buffer layer. Cu was chosen for this and for the NM layer in the GMR ML. The growth of epitaxial Cu layers on epitaxial Nb base (contact) layers has recently been investigated [46,60]. In those reports, the lower-energy Nishiyama-Wasserman (N-W) relationship was determined to exist. The interface between Cu and Nb has also been found to follow the Kurdjumow-Sachs (K-S) relation $(\langle 110 \rangle \{111\}_{\text{Cu}} \parallel \langle 111 \rangle \{110\}_{\text{Nb}})$ in thin Cu films grown on Nb base layers and in multilayers [51,61]. This should form a close packed (111) surface of Cu for further epitaxial growth. Figure 2.2A shows a schematic of the K-S relation viewed in the plane of the TEM samples.

Ideally subsequent epitaxial layers of Co and Cu should form with uniform planes of (111) fcc Co growing on (111) planes of Cu. The hcp to fcc structure change in Co is generally found to occur martensitically at a temperature of 422° C (Figure 1.5). The lattice mismatch is about 2% and in thin layers this should be accommodated elastically. Figure 2.2B shows the relative relationship in the TEM sample plane.

Table 2.1 Co/Cu bilayer and GMR multilayer fabrication temperatures

SAMPLE	Layer	Deposition T	Anneal t@T	Comments
19-3	Nb	750	10 min @ 950	Epitaxial 1 bilayer Cu _{20nm} /Co _{20nm}
	Cu	350		
	Co	450		
19-4	Nb	750	10 min @ 950	Epitaxial 1 bilayer Cu _{20nm} /Co _{20nm}
	Cu	470		
	Co	100		
20-1	Nb	750	10 min @ 950	Epitaxial (Co _{6nm} /Cu _{6nm})x 6 layers
	Cu1	150	350	
	Bal	90-100	-	
20-2	Nb	RT	RT	Polycrystalline (Co _{6nm} /Cu _{6nm})x 6 layers
	Cu ₁₋₆	RT	RT	
	Co _{1-6nm}	RT	RT	
20-3	Nb	750	10 min @ 950	Epitaxial (Co _{6nm} /Cu _{6nm})x 6 layer
	Cu1	450	-	
	Bal	90-100	-	
20-4	Nb	750	10 min @ 950	Epitaxial (Co _{6nm} /Cu _{6nm})x 6 layer
	Cu1	450	-	
	Co1	490	-	
	Bal	90-100		

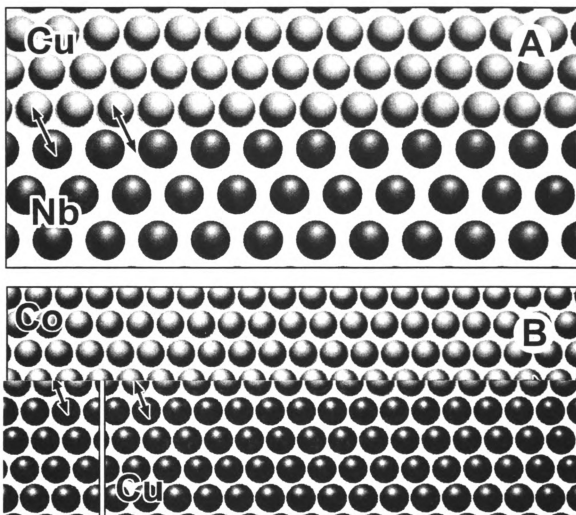


Figure 2.2. Schematics of ML stacking. A) Fcc Cu over bcc Nb in the Kurdjumow-Sachs orientation. B) The non-relaxed incoherent spacing between Co and Cu in the fcc crystal structure.

2.3 CIP GMR measurements

Although the Nb contact layer prevents direct comparison with previously reported data collected for similar MLs, current in plane (CIP) measurements were made between one epitaxial sample and one polycrystalline sample for a relative comparison. Samples 20-1 and 20-2 were tested in conventional 4-probe CIP configuration, at room temperature with a maximum applied field of 2 kOe. The general form (Figure 2.3) of the CIP GMR response for sample 20-2 was similar to that reported previously for polycrystalline ML samples of this motif [13, 62]. Sample 20-1 showed a $\Delta R/R$ of 1.3% while 20-2 showed 3.1% $\Delta R/R$. While these values cannot be directly compared to conventional CIP devices, due to the large Nb conduction, these values are in agreement with those seen previously in Co/Cu MLs with a 6 nm motif [13]. The two remaining samples, 20-3 and 20-4, were not tested.

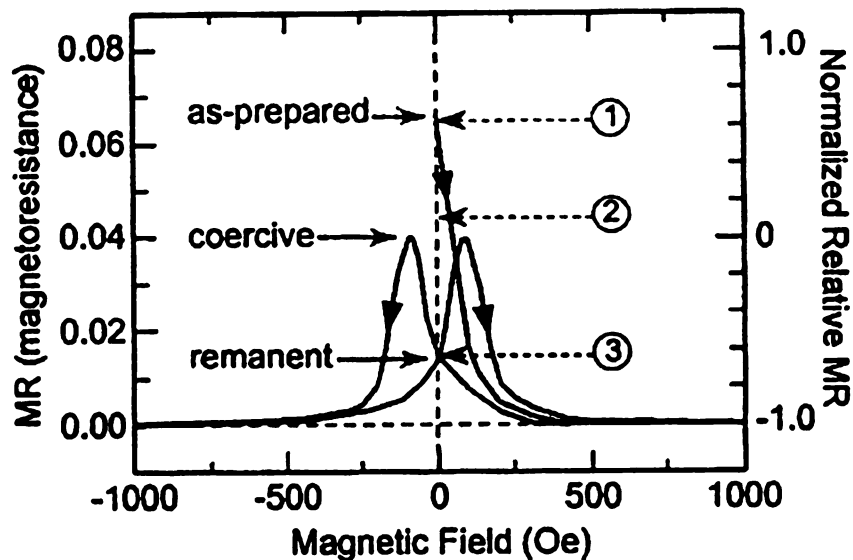


Figure 2.3. The general CIP MR response in Co_{6 nm}/Cu_{6 nm} MLs [13].

2.4 TEM sample preparation

The cross sectional samples for TEM, AEM, and HRTEM were prepared essentially by the methods of Bravman and Sinclair [63] as modified by Howell [64] and Geng, *et al.* [54]. This was accomplished by scoring the as-fabricated ML substrate (backside) and snapping the wafer into strips roughly 0.3 x 1.0 cm. The resulting pieces were cleaned in acetone and ethanol and glued, with the ML surfaces facing each other, with Gatan G-1™ Epoxy cement. The sample was then clamped with gentle pressure in a spring-loaded Teflon™ lined clamp and cured for about 1 hr at $\approx 130^{\circ}\text{C}$. Following polymerization, the resulting “sandwich” was backed in two layers of silicon (or sapphire) wafer cemented to the initial assemble with the same technique. The use of sapphire backing made a more robust sample after final ion milling owing to the lower sputtering rate than Si, which often perforated before the region of interest at the bottom of the dimple. However, the thickness of the clear and colorless sapphire cannot be judged as easily as Si when dimpling.

The resulting stack was temporally mounted on a 25 x 40 mm glass microscope slide with Crystalbond™ mounting wax. This was then sliced perpendicularly to the wafers surface with a high-speed diamond saw (Strueres Acutome-5), operated at 3000 rpm with a 5 $\mu\text{m}/\text{sec}$ feed rate, to yield slabs approximately 800 μm thick. These slabs were polished to a 50 nm finish with a series of diamond lapping films (15,5,3,1 μm 3M Imperial™ diamond lapping film) followed by 0.05 μm colloidal diamond. After washing in detergent and water followed by water and ethanol rinses, the polished side was cemented (G1

epoxy) to a Mo support ring 3 mm in diameter with a 2mm hole. This slab-and-ring assembly was wax mounted in the center of a 19 mm optically-flat sapphire disk and lapped, with the same series as the first side, leaving a final specimen thickness of $\leq 80\mu\text{m}$. The samples were then mounted and centered on the platen of a VCR group D500I dimpler and dimpled with 1 μm diamond slurry using a 15.5 mm stainless steel wheel. Alternatively, a similar diameter, 1 μm embedded-diamond lapping wheel was used with VCR lapping vehicle as the lubricant. The termination point, a thickness of $\approx 10\mu\text{m}$, was determined by period removal of the sample and observation via light microscopy, with a stereo microscope, every 10 to 20 μm of dimpling. The samples were then polished to a specular surface with colloidal diamond (0.050 μm). Following the final polish, the samples were dismounted from the dimpler supports with acetone, washed in ethanol, air dried and mounted on a Gatan DuoPost™ support and ion milled to perforation in a Gatan M691 PIPS™ ion mill. The samples were milled at $\pm 3^\circ$ beam incident-angle with 5 keV Ar ions, while turning at 3 rpm until a small perforated area was seen at the bottom of the dimple. Figure 2.4 shows an overview of the preparation sequence.

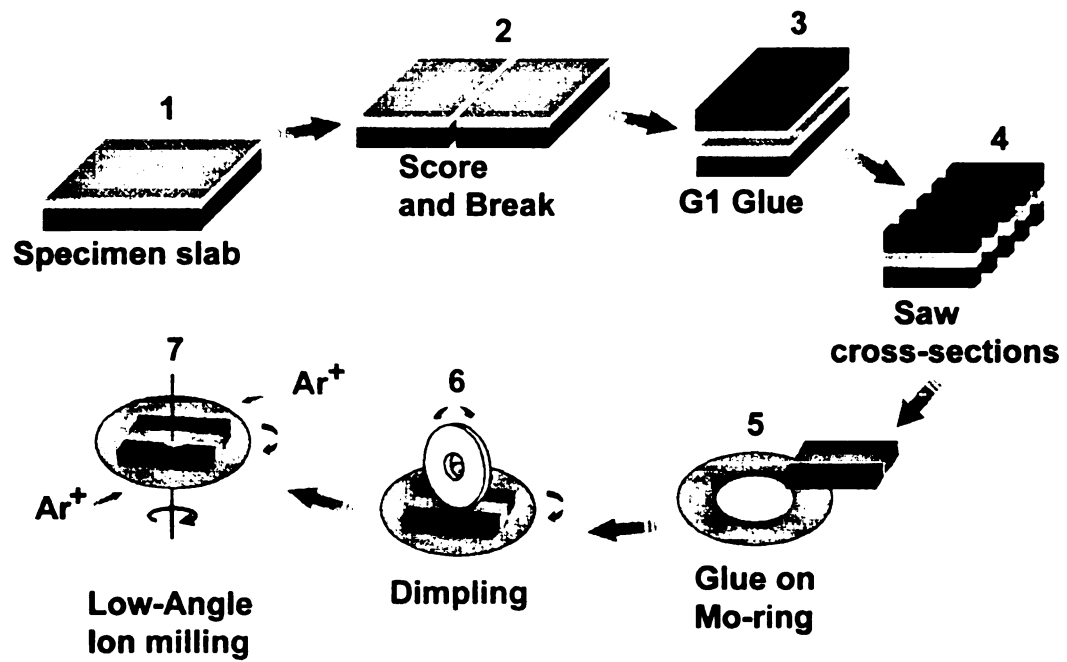


Figure 2.4. Schematic of the main steps in specimen cross-section preparation.

2.5 TEM experimental methods:

CTEM Imaging

Routine brightfield and darkfield CTEM imaging, to judge the overall morphology, crystallinity, quality of the sample and preparation, was accomplished with a Hitachi H-800 TEM operated at 200 keV. Some CTEM images were recorded on a JEOL 4000EX 400 keV microscope with a double-tilt top entry stage. An aperture small enough to exclude ordered diffraction from the component materials used in the samples was used for CTEM imaging (brightfield and darkfield). (Figure 2.5). Selected area electron diffraction (SAED) was used to roughly characterize the degree of polycrystallinity and to orient the samples on low order zones. The SAED patterns were recorded with the smallest aperture that would completely cover the whole ML stack, including the Nb base and capping layers. Images and SAD patterns were recorded on Kodak 4489 EM film (200 keV) and SO-163 (400keV) processed as suggested by Kodak.

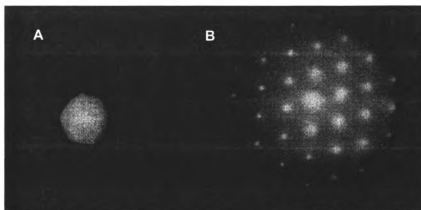


Figure 2.5 Objective apertures used in TEM imaging in the JEOL 4000EX. A) The CTEM aperture, a 7.2 nm^{-1} diameter. B) The Scherzer aperture, 20.8 nm^{-1} . The diffraction pattern is Si, $B = \langle 110 \rangle$ showing 36 transmitted beams (including the direct spot).

HRTEM

HRTEM analyses of thin areas of interest were accomplished using a JEOL 4000EX TEM with a LaB₆ cathode operated at 400 keV. The HRTEM was performed at the Electron Microbeam Analysis Laboratory (EMAL) located at the University of Michigan, Ann Arbor, MI. For lattice imaging, an objective aperture (#2 aperture - 20.8 nm⁻¹) was used to remove frequencies significantly above the Scherzer resolution limit (Figure 2.5). Lattice image micrographs were recorded at a nominal 2.5 to 8.0 x 10⁵ times magnification on Kodak SO-163 sheet film, with the objective lens set to approximately Scherzer defocus. For Fresnel imaging, the 7.2 nm⁻¹ aperture was used to exclude all but the desired beam. Specimens were tilted to the desired zone axis using the sapphire substrate (dynamical) diffraction pattern from material immediately below the area under investigation. This should allow the crystal tilt to be aligned to within about 0.4° of the zone axis using the symmetrical brightness of the reflections of the {10 $\bar{1}$ 0}. This is calculated using the angle to these first order reflections $\theta = \tan^{-1}(R/L)$, where R is measured from the diffraction pattern direct spot to any {10 $\bar{1}$ 0} reflection, and L = Rd/λ. The value of d is known to be 0.233 nm and λ is the relativistically corrected 400 keV λ of 0.00164 nm.

HREDS

Compositional analysis of the MLs, collectively as well as regions of individual various layers, was accomplished via high-resolution energy-dispersive X-ray spectroscopy (HREDS). The spectra were acquired with a JEOL 2010F TEM/STEM, also at the EMAL. The microscope was operated in a spot EDS

mode using a probe that was varied between ≈ 70 nm and 0.5 nm at the specimen surface, depending on the area for spectral acquisition. An EDAX Phoenix windowless SiLi detector system was used to capture spectra after which spectral files were translated to Microscopy Society of America (MSA) format for subsequent analysis using Desk Top Spectrum Analyzer DTSA [65]. No direct method was available for specimen-level beam-current measurement and known standards were not available so comparisons among specimens are qualitative.

Foil Thickness Measurements

Specimen thickness normal to the incident beam is desirable for accurate assessment and modeling of HRTEM images and for quantitative EDS. Foil thickness can be determined in several ways. The easiest is to generate a feature on either side of the foil (e.g. carbon contamination) and geometrically calculate the thickness by separating the projection of the features with a known angle of specimen tilt. This method generally over estimates the specimen thickness and is of limited use in the case of very thin (HRTEM) specimens [66]. One of the more widely used methods of calculating foil thickness is the use of CBED. Indeed, the technique was verified using a Co alloy [67,68]. Attempts were made to use this method. However, a satisfactory CBED pattern was not generated from the ML and the entire area of interest on the ML was apparently less than $1\xi_{\{10\bar{1}0\}}$ for sapphire. The method of choice, if available, is electron energy loss spectrometry (EELS). Not only can the thickness at a given position be measured from the ratio of zero -loss to total intensities but, if a scanning

mode is available, a thickness map can be generated [65]. Unfortunately, the EELS features on the analytical microscope used were not available during the analysis period. A second analytical method of thickness determination, and one that the ML sample geometry lends itself to is differential X-ray absorption (DXA) [69]. The foil thickness of a single element can be determined from the EDS X-ray spectrum if the spectrum contains two detectable, sufficiently separated characteristic peaks. The Nb base layer provides an ideal internal thickness standard as its EDS spectrum contains widely separated L and K peaks. The Nb layer also tapers from a thickness of zero at the margin of the ion milling perforation to electron opaque at some distance away along the ML.

A series of EDS spectra collected from this foil yielded a linear relationship between L_{α} and K_{α} intensities when plotted against distance from the ion milled edge of the Nb layer. However, attempts to match the slope of the thickness to simulated absorption ratios failed. This appears to be due to either differences in modeled vs. actual detector geometry and/or the presence of an extensive amorphous contamination layer on the specimen. The system could be calibrated with a known thickness of Nb foil, providing a rapid method of thickness determination, in near real time without altering the specimen tilt conditions being used for high-resolution work.

2.6 TEM image analysis

Structural analysis of the HRTEM images was accomplished using calibrated magnification prints, digitized with a flat-bed scanner coupled with a microcomputer. The programs used were NIH image [70] and Adobe

PhotoShop™ (equipped with the Image Processing Tool Kit [71] suite of analytical plug-ins). Digitized enlargements of HRTEM images were calibrated using lattice images of known orientations of the Nb contact layers. Similarly, the fast Fourier transforms (FFT) of selected areas of the digitized images were calibrated with transforms of the Nb lattice images. The spacing of the $\{110\}$ lattice spots seen in the $[111]$ Nb projection transform were found to be indistinguishable from the $\{10\bar{1}0\}$ lattice spots seen in $[0001]$ sapphire projection (Figure 2.6). Sapphire is regarded as undistorted by the Nb layer [48,49]. Both the NIH image fast Hartley transform [72] and the proprietary FFT program code used in the IPTK suite yielded identical result when applied to the same real space pixel maps. Thus the latter was used, for convenience, in most cases. Transforms for orientational and structural analysis were made from 128×128 , 256×256 and 512×512 pixel arrays selected from 600 pixel / inch images from photographic prints printed at final magnifications from about 2.7×10^6 to 10^7 times magnification. The choice pixel density in the analysis was a function of the final image size and the expanse of a particular analysis. The angles between resolvable lattice planes and their respective spacings for the equilibrium structures of the elements used in these MLs are shown in Figure 2.7.

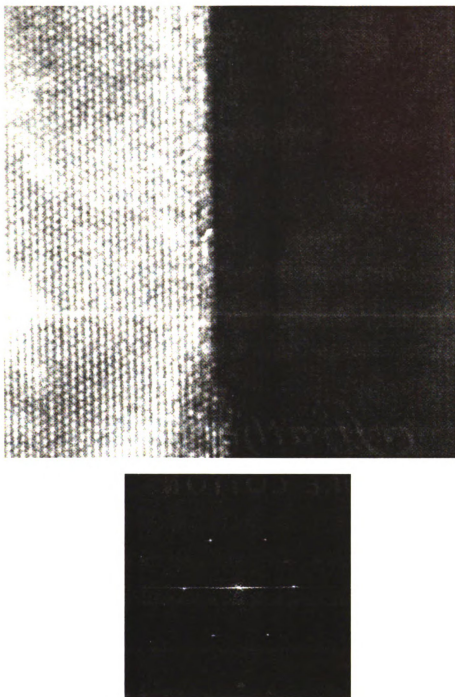


Figure 2.6. The Sapphire/Nb boundary. The transform of this area shows that there is no detectable difference in the Nb $\{110\}$ and sapphire $\{10\bar{1}0\}$ spacings. Thus Nb lattice images were used to calibrate the HRTEM images.

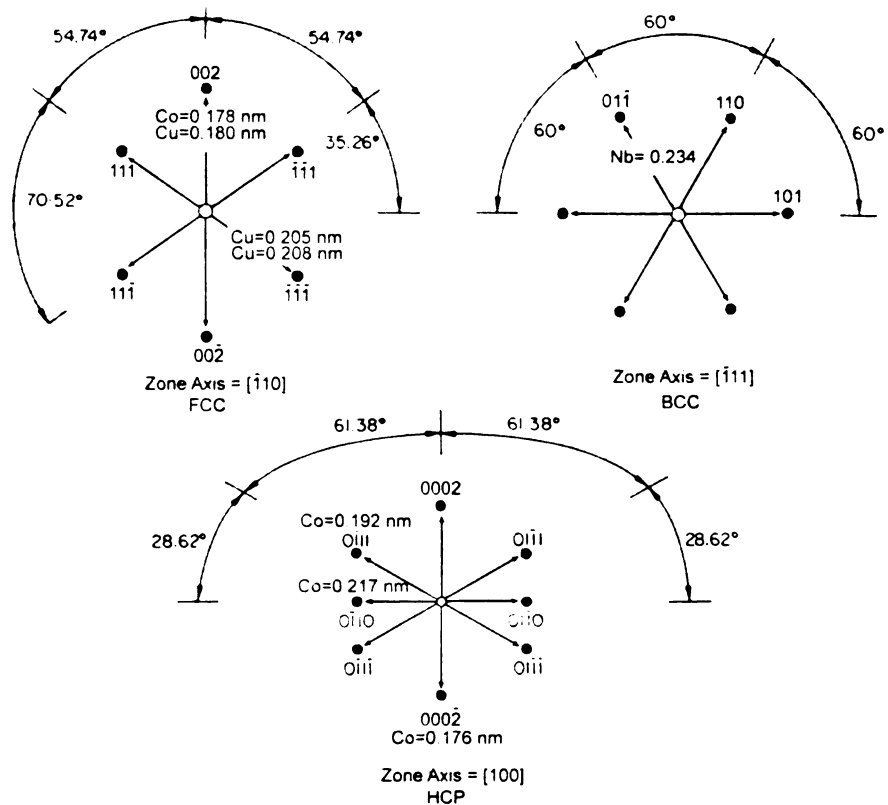


Figure 2.7. Resolvable lattice planes and their interplaner angles for equilibrium structures of the elements used in the ML fabrication.

CHAPTER 3 EXPERIMENTAL RESULTS

Four ML samples (three epitaxial and one polycrystalline) and two epitaxial bilayer samples were evaluated using TEM methods. The results of these observations are presented, sample by sample, below. CTEM and HRTEM were performed on representative thin areas of ion-milled cross -sections of each of the samples. HREDS was performed on selected areas and structures in two of the epitaxial samples . These were the polycrystalline ML sample and one of the epitaxial bilayer samples. Within each sample, the order in which individual layers were analyzed by HRTEM was from the upper-most "top" of the multilayer progressing to the base layer. Thus, after the Nb capping layer, the first stratum of the multilayer analyzed was the last copper layer deposited (Cu6). This was followed by Co6, the last cobalt layer deposited, etc.

3.1 Sample 20-1 (epitaxial)

CTEM of sample 20-1

CTEM, provided useful information about the overall uniformity, growth texture, degree of epitaxy, and continuity of layers in all of the Co/Cu MLs in this study. Figure 3.1 shows constant magnification brightfield and darkfield images of the epitaxial sample 20-1. The images in Figure 3.1 A & B, taken with the beam normal to the sapphire ($1\bar{1}00$) show a large and variable amount of contrast in the Nb layer. This indicates that the Nb base contact layer is crystalline but with a high defect density. The absence of grain boundaries suggests that it is a single epitaxial crystal. The measured Nb contact layer thickness was 201 nm (calculated from HRTEM lattice images) which is about

20% thinner than the nominal value of 250 nm. An SAED pattern from this sample is presented as an insert in Figure 3.1. It shows that there is good long-range order, with no observable radial blurring of the diffraction spots, which would be the result of multiple grains oriented close to a given axis. There is little interlayer contrast evident when imaged on the zone axis at Gaussian focus (Figure 3.1A). However, a weak layer modulation is evident in the darkfield image obtained using the Nb (200) reflection. Defocusing the objective lens reveals the layering much better (Figure 3.1C). The ML stack shows a consistent growth direction modulation, over the entire observed length, consistent with 6 bilayers. The Cu "buffer" layer thickness is also reasonably close to the nominal value (20 nm) for the first layer. Across the field of view measured, this thickness varied between 26 nm and 20 nm. The $(\text{Cu}_{6\text{ nm}}/\text{Co}_{6\text{ nm}}) \times 6$ ML averaged about 79 nm over the area viewed which is about 10% thicker than the nominal 72 nm thickness. The Co ($Z=27$) layers of the stack appear darker than the Cu ($Z=29$) layers (Figure 3.2), which is inconsistent with elastic scattering contrast (variations in transmitted intensity) which is proportional to Z^2 . In addition, although the total ML thickness is close to the nominal sum, the individual Cu layers in the stack appear thinner than expected.

HRTEM of sample 20-1

Regions of interest in the sample MLs were also examined using high resolution transmission electron microscopy (HRTEM). Images were recorded, near Scherzer defocus, from thin areas having a complete ML device cross section remaining.

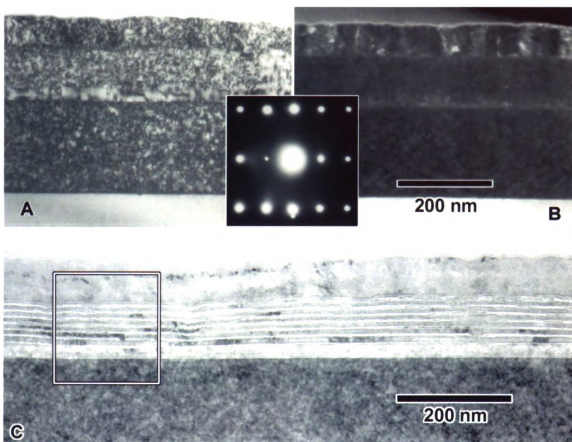


Figure 3.1. CTEM images of sample 20-1. A) Brightfield minimum contrast focus image, normal to the sapphire ($10\bar{1}0$). B) (200) Darkfield on the same axis. C) Over-focused brightfield image showing Fresnel contrast parallel to the layer interfaces.

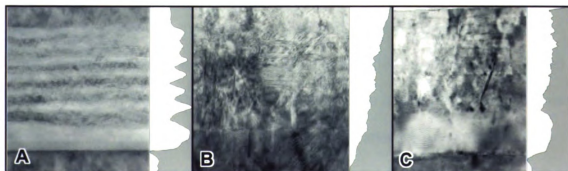


Figure 3.2. Multibeam (HRTEM) approximately Scherzer focus images and average density plots along MLs. A) Sample 20-1. B) Sample 20-2. C. Sample 20-4.

Figure 3.3 shows an overview HRTEM image of a representative area of the 20-1 ML. In this image, the general layering seen in the CTEM image (Figure 3.1) is still evident, despite the similarity in the scattering power of the Co and Cu constituents. Selected areas in the three regions delineated were analyzed via FFT analysis to assess lattice structure. The apparent local roughness and diffusiveness of the interfaces decreases with layer number towards the Cu buffer layer. A general increase in the crystallographic order of the layers and in their overall width can also be seen towards the buffer layer. Additionally, both the top and bottom Nb-Cu interfaces exhibit apparently diffuse zones. Some recording artifacts are also present. A small, white, "aster-like" feature can be seen in the second delineated area. This was the result of a static electrical discharge during film handling.

The upper part of the ML (Figure 3.3 inset 1) is detailed in Figure 3.4. The dark region at the top of the micrograph is the capping Nb layer. Below that can be seen the top two Co layers (also relatively dark) and the adjacent Cu layers. Insets A through F delineate the square (256 X 256 pixels) areas used for FFT analysis. In Figure 3.5, the regions A-C are enlarged and presented (growth direction vertical) along with their contrast-inverted (lattice spots appear white) FFTs. In Figure 3.5A, the top Nb layer shows some lattice fringes in the growth direction which are indicated by the two vertically oriented maxima in the adjacent FFT spaced at 0.23 nm, consistent with the Nb {110} spacing. Other than these maxima, the FFT is relatively diffuse, indicating a lack of resolvable

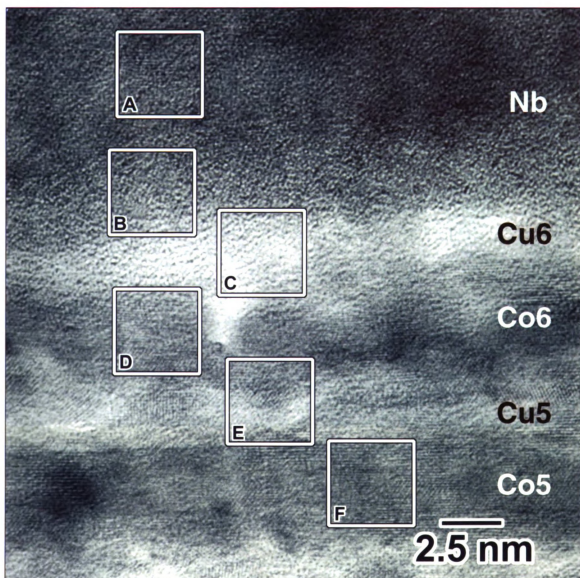


Figure 3.4 An HRTEM image of the upper layers in sample 20-1. This figure is oriented with the growth direction running vertically. The top dark region is the capping Nb layer. The insets are areas that were tested by FFT analysis.

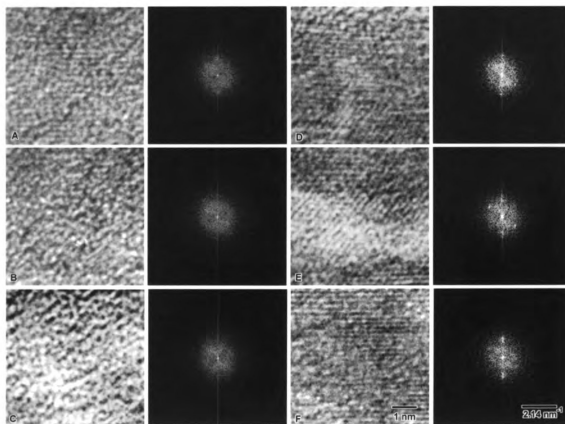


Figure 3.5. Selected HRTEM images A-F and their FFTs from the upper layers of sample 20-1.

crystal periodicities at other angles or frequencies. Figure 3.5B shows the image and transform of the diffuse region between the last deposited Cu layer (Cu6) and the Nb capping layer. The FFT of this area shows two weak maxima, oriented about 38° from the growth direction, spaced at 0.18 nm, consistent with the Cu (200) interplanar spacing. This implies that the direction of the close packed planes was about 17° off the nominal growth direction for the whole ML. The third area, Figure 3.5C, is an area that should be contained in the Cu6 layer. The FFT shows a diffuse contrast consistent with an amorphous phase rather than discrete maxima indicating order. Inset Figure 3.5 D is taken from the topmost Co layer (Co6). This transform shows two fairly strong reflections spaced at 0.20 nm in the growth direction, consistent with Co_{fcc} (111) spacing. However, there are also two weaker reflections, corresponding to spacings of 0.25 nm, at an angle of 57° to the growth direction. Inspection of the transformed area for this sample shows lattice fringes corresponding to this angular orientation in mainly in the lower left quadrant. This spacing is inconsistent with those expected in the ideotype ML. It most closely matches the "a" value for α -Co, 0.251 nm (twice the $(1\ 1\ \bar{2}0)$ spacing). In Figure 3.5 E, the transformed area from the Cu5 layer shows a wavy band of contrast across it. The FFT of this region yielded the 0.20 nm spaced reflections in the growth direction and a second wider set (0.25 nm), as did the previous area. However, in this area the angle for the second set of spots was 55° relative to the growth direction. Additionally, the spots on the growth axis appeared elongated; nearly, but indistinctly, two closely spaced reflections. In the final area analyzed in the top

portion of the ML, Figure 3.5 F, the selected area is situated centrally on layer Co5. The elongated growth direction reflections, seen in the previous selection, are resolved into spacings of 0.20 and about 0.25 nm.

In Figure 3.6, the middle field of the overall HRTEM image (Figure 3.6 inset 2), progressively more distinct layer interfaces are seen from the Co5||Cu4 interface down through the layers to the Co2||Cu2 interface near the bottom of the figure. An area enlargement and transform from the Co5||Cu4 interface is shown in Figure 3.7A. In addition to the 0.20 nm and 0.25 nm spots oriented in the growth direction, there appears to be a discontinuous (polycrystalline) ring at about the 0.29 nm spacing. This spacing is not from any known orientation of the component materials. . In the center of the area layers Co4 and Co3 are of nearly uniform contrast. In Figure 3.7B, (Co4), the strongest intensities are along the growth direction consistent with the lattice images visible in the micrograph. The 0.20 nm and 0.25 nm spots, resolvable in the previously inspected area are less distinct, however. Figures 3.7 C and D are two samples from the Cu3 layer. In the first of these (C), in addition to the growth oriented 0.20 nm spots consistent with the Co and Cu {111} spacing, there are two other sets of resolvable spots. These are both from a lattice spacing of 0.29 nm. They are oriented 72° from each other and 18° from the growth axis. In the micrograph these appear as a "texture" parallel to the growth axis. Across the same Cu3 layer, Figure 3.7D shows lattices in the growth direction at the Co or Cu {111} 0.20 nm spacing, 32° from this are planes at the 0.29 nm spacing. There is another strong set of spots 120° from the growth axis and 92° from the

previously mentioned spots that correspond to a 0.24 lattice, this is just slightly wider than the Nb {110} (0.23 nm) spacing. Figure 3.7D, the lattice image that produced this transform, appears to contain at least two areas with distinctly different lattice orientations. Figure 3.7E is an area of layer Cu₂. However, most of the lattice image seen in this area appears to be a contribution from the adjacent Co layers. The transform shows growth direction oriented spots and an additional weaker set at about 47° from the growth axis. The final area from the middle region of the ML, Figure 3.7F, shows an area from the Co₂ layer. The only distinct spots in this image are at spacings of 0.20 and 0.23 nm along the growth axis. These spacings suggests the presence of a Nb {110} lattice and the Co/Cu {111} lattice in the same area. The HRTEM image (Figure 3.7F) appears to have two different lattices in it and a wider spacing is seen in the upper right-hand corner of the image compared to the lower left-hand side.

The Co₁ layer, the Cu buffer layer, and the top of the Nb epitaxial base layer are shown in Figure 3.8 (inset 3 in Figure 3.3). Areas with significantly different and distinct lattice structures are evident across this field of view. In Figure 3.9A, an area of the nearly uniform Co₁ layer is shown. In the adjacent transform, there is a set of strong, sharp spots at 0.20 nm spacing along the growth axis, which are again suggestive of the Co/Cu {111} planes. The area of the Cu buffer layer adjacent to the Co₁ (Figure 3.9B) layer shows apparent lattice order in several directions and spacings. The FFT of this area shows 5 distinct sets of spots. Along the growth axis, there are sets at the 0.20 and 0.25 nm spacings.

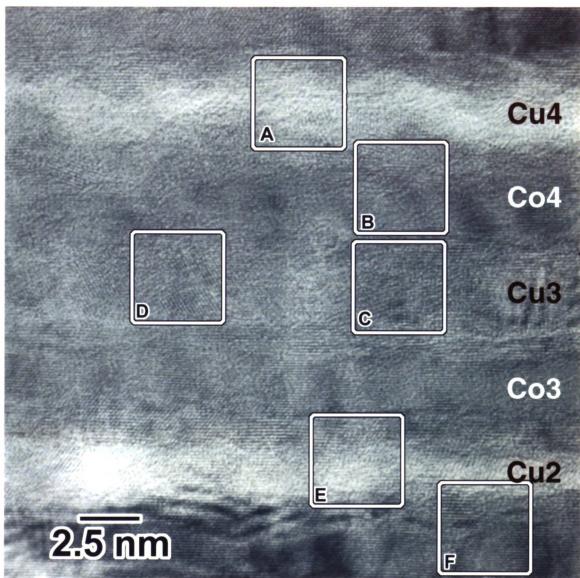


Figure 3.6 HRTEM image of the middle layers in sample 20-1. This figure is oriented with the growth direction running vertically.

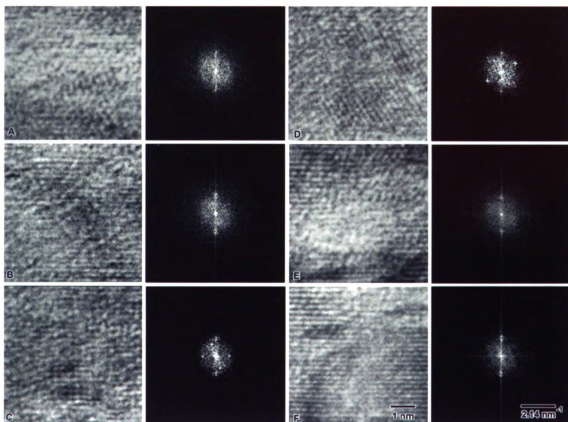


Figure 3.7. Selected HRTEM images A-F and their FFTs from the middle layers of sample 20-1.

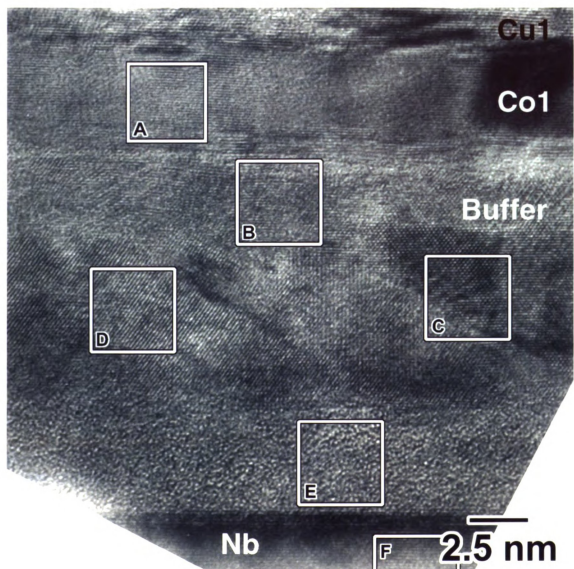


Figure 3.8. HRTEM image of the bottom layers in sample 20-1. This figure is oriented with the growth direction running vertically. The lowermost area, F, is the bottom Nb layer.

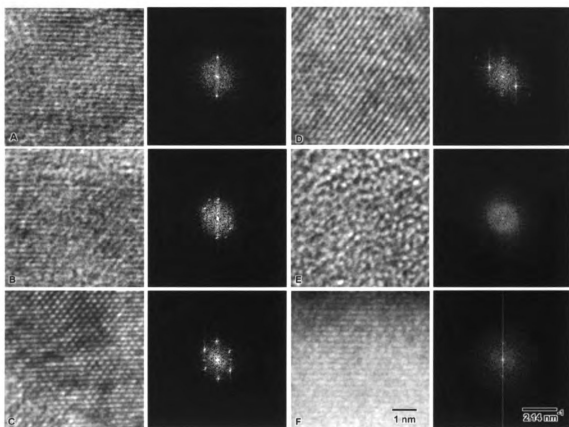


Figure 3.9. Selected HRTEM images A-F and their FFTs from the bottom layers of sample 20-1.

At an angle of 25° to these growth direction spots, there is a second 0.20 nm spaced pair. At 55° there is a second pair of 0.25 nm spacings. Finally at 90° to the growth axis, there are two weaker spots that correspond to a spacing of 0.30 nm. In Figure 3.9C, which is also from about the middle of the Cu buffer layer, the most distinct lattice image in the buffer layer is seen. There are 0.20 nm spacings along the growth axis, consistent with the expected {111} lattice, and an additional set of 0.25 nm spaced spots at 55° to the growth axis. At 72° from these spots are a third pair with a spacing of 0.280 nm. The FFT in Figure 3.9C also shows higher order reflections of lower intensity that appear to be second order spacings from the lower frequency lattices. In an adjacent area of the buffer layer (Figure 3.9D), strong fringes 55° from the growth axis with a spacing of 0.25 nm are again evident and are more intense than the weak growth direction spots. Again in this area, there are spots 72° from the highest intensity 55° set (122° from the growth axis). The inner most set of spots in this series corresponds to a spacing greater than 0.6 nm. The final area of the buffer layer selected was the interface with the Nb base layer (Figure 3.9E). This area was remarkably uniform throughout the area observed. Its contrast was intermediate between the Cu buffer layer and the Nb base layer. An FFT of a representative area of this band shows no indication of any crystalline order. Figure 3.9F is an area from the Nb base layer. Although only the top portion is shown in Figure 3.8, the entire square area in 3.9F was used for the FFT. This area appeared as expected for the Nb in this orientation, with only the (110) planes resolvable.

HREDS of sample 20-1.

HREDS of Co/Cu ML samples were acquired in spot mode on a JEOL 2010F with a windowless detector as described in Chapter 2. Two minute live-time spot-mode spectra were acquired. This was accomplished using an incident spot size that just covered the ML in cross sectional aspect. Three of these spectra, from near but not overlapping areas of the ML, were averaged. This averaged spectrum, along with a DTSA simulation using the microscope, spectrometer, and specimen parameters outlined in Chapter 2, are presented in Figure 3.10. In addition to the expected X-rays from Co and Cu, small peaks are visible in all of the real spectra consistent with C, O, Al, Nb and Mo characteristic X-rays. The carbon contribution is at least partially due to unavoidable contamination build-up in the microscope. The oxygen and aluminum are likely due to the resputtering of trace amounts of the sapphire substrate. The Nb is likely sputtered from the base layer of the ML and the Mo from the support ring. A hole count revealed no detectable levels of these elements. Most strikingly, the relative peak heights for the Co and Cu K X-rays are far from the yield ratios implied by the simulation. Further analysis of 36 spectra (18 each from Co and Cu layers) selected from arbitrary locations along the ML is presented in Figure 3.11. Figure 3.11A shows a spectrum of the averaged Co and Cu peaks from 18 "light" (nominally Cu)

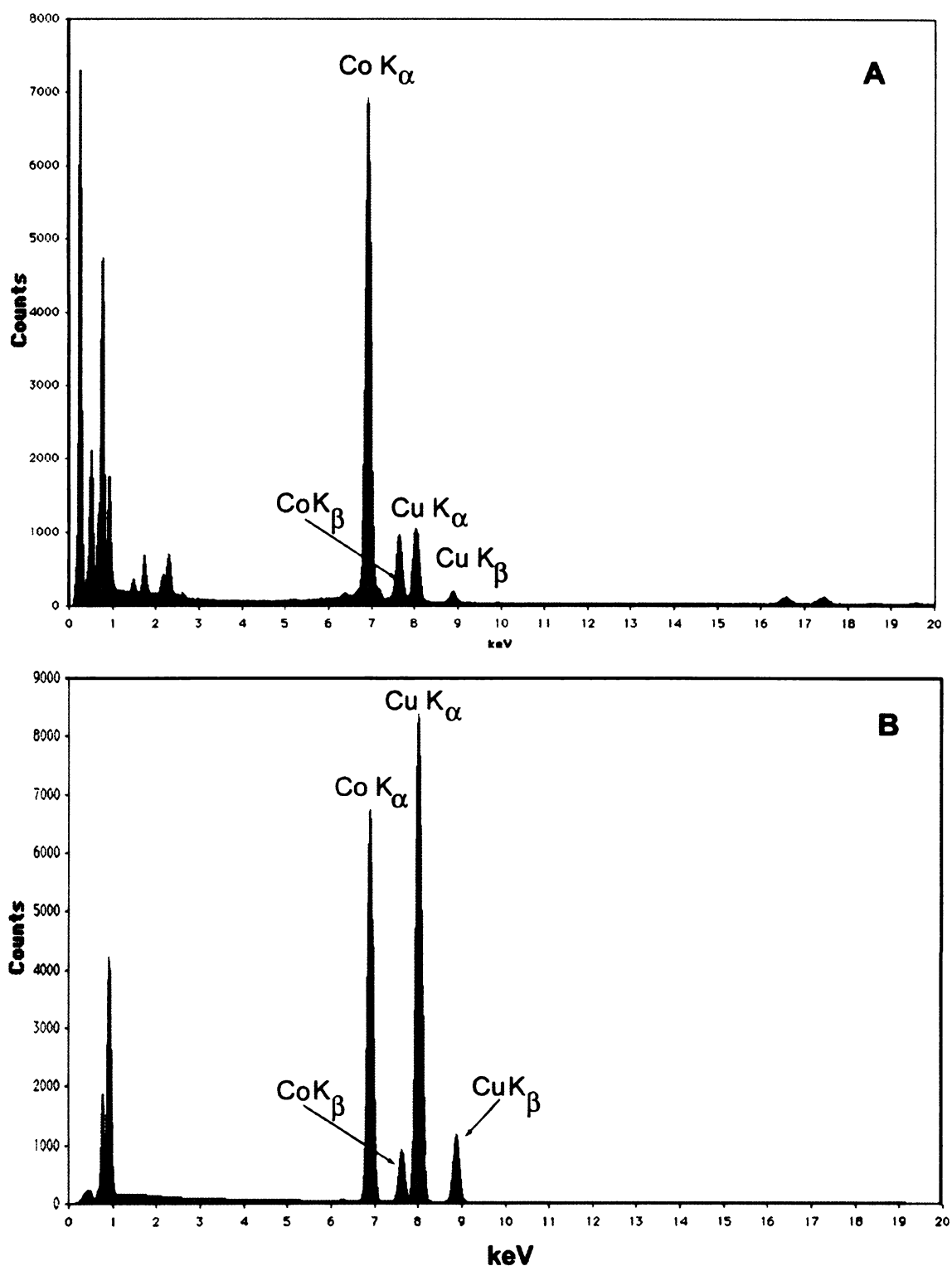


Figure 3.10. EDS spectra from a cross-section the 20-1 ML structure. A) The spectrum formed by averaging three whole-ML spectra. B) DTSA simulation of a Co/Cu sample with the same volume fractions as a circular sample of the 20-1 ML motif

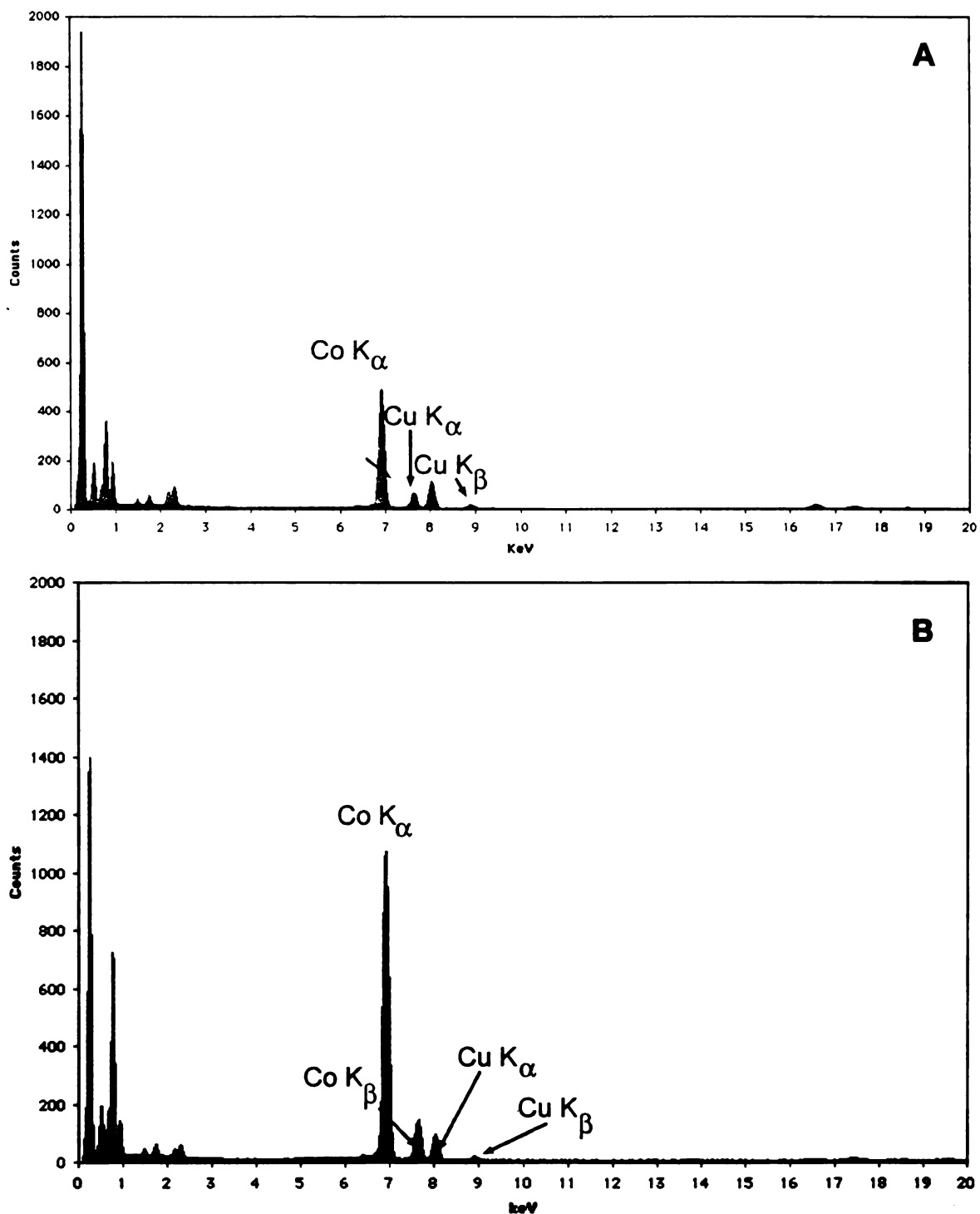


Figure 3.11. EDS spectra from a cross-section the 20-1 ML structure. A) The spectrum formed by averaging 18 Cu layer spectra. B) The spectrum formed by averaging 18 Co layer spectra.

layers. This spectrum shows a low total count number and a very low Cu proportion. The total X-ray yield was nearly an order of magnitude less than that seen for the ML as a whole (*c.f.* Figure 3.10A). Figure 3.1B is a spectrum from the mean of the complementary 18 Co layers showing about twice the Co K X-ray intensity and nearly the same Cu intensity as the mean for the Cu layers.

Summary for sample 20-1

At first observation in CTEM, sample 20-1 appeared to be a reasonably well grown epitaxial sample when viewed at lower magnifications. In the electron diffraction pattern normal to the $(1\bar{1}00)$ (*i.e.* the $[1\bar{1}0]$) both the ML and the Nb base layer appeared as a single crystal. However, imaging in the HRTEM mode, especially at the magnifications used for lattice imaging, revealed highly anomalous growth in the ML. The crystallinity of the nominally Cu layers was either largely missing or appeared to be continuations of lattices originating in the much more strongly crystalline Co layers throughout most of the ML. Lattice spacings inconsistent with those of the equilibrium structures of the sample components were seen in all regions. The Cu buffer layer had what appeared to be an amorphous interface with the Nb base layer, which is not expected with a pure Cu||Nb interface. HREDS showed that the sample, as a whole, contained no unexpected elements, was Cu deficient, and that the Cu layers appeared to be "mass deficient" which corroborated the lower than expected electron scattering seen in the nominally Cu layers when viewed in HRTEM (*c.f.* Figure 3.2A and 3.2B).

3.2 Sample 20-2 (polycrystalline)

Sample 20-2 was grown during the same operation cycle and under the same sputtering conditions as the epitaxial samples (Table 2.1), with the exception that the entire sample was grown at room temperature and there was no post deposition anneal.

CTEM of sample 20-2

In Figure 3.12 the ML is shown in cross section with the sapphire substrate oriented in the [0001] direction. The SAED pattern (inset), which included only the ML and Nb contacts, shows the ML is highly textured in the [111] growth direction. Figure 3.12A is a brightfield image of the polycrystalline 20-2 sample showing the columnar growth. In Figure 3.12B, the same area is presented in a darkfield image using the Nb ($0\bar{1}1$) reflection. As expected, in either brightfield or darkfield mode, there is little interlayer contrast at near Gaussian focus. The bottom Nb layer is distinguishable from the rest of the ML, due to interruptions in the contrast of the columnar crystals at its interface with the Cu buffer layer and greater electron scattering. In Figure 3-12C (the same area recorded 11 μm below minimum contrast focus) the layering is quite evident. Consistent with the nominal deposition, the first layer above the Nb contact is a thicker Cu layer. However, there appears to be only 5 bilayers above this, as opposed to the 6 pairs planned. Fresnel defocus contrast also shows that there is a sample-wide unevenness in the bilayer stack. The amplitude of this unevenness appears to increase with layer number. It also appears to show layerwise coincidence, with

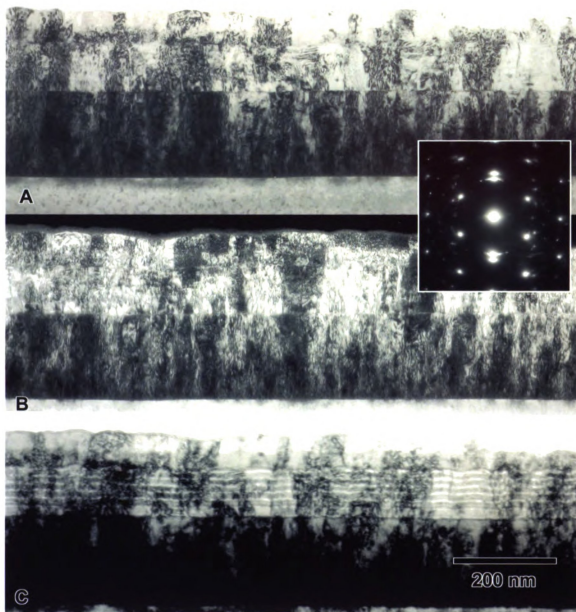


Figure 3.12. CTEM images of sample 20-2. A) Single beam brightfield image of a cross section of the 20-2 ML. B) The darkfield image created using the (010) Nb spot. C) A single-beam brightfield image taken 11 μm below minimum contrast.

roughness features arising from the first layers deposited being propagated through the ML stack.

HRTEM of sample 20-2

The overall interlayer contrast in the polycrystalline sample 20-2 was much less obvious than that seen in the HRTEM images of sample 20-1(Figure 3.2B), although a wide range of layer-dimension crystallographic features were apparent. Figure 3-13 shows a low magnification HRTEM image of a selected region of the ML cross section. The region outlined in the center was chosen for lattice image analysis as it appeared to contain examples of the major crystallographic features. The most striking of these features is the striated appearance of the nominally Co layers, Co2-Co5, in the center of Figure 3.13. The images were recorded along the sapphire [0001] rather than normal to the $(01\bar{1}0)$ sapphire, as was the case for sample 20-1. Four 26 nm square regions were selected from the HRTEM image field for analysis (Figure 3.14). The first two of these areas (insets 1 and 2) were chosen to incorporate examples of most of the obvious types of crystal defects observable in low magnification micrographs. As before base-layer Nb lattice image $\{110\}$ planes, from the same negative as the ML areas, were used for calibration. In Figure 3.14, the nominal layer positions, judged by local differences in interlayer contrast are also indicated. Consistent with the results of the Fresnel contrast image (Figure 3.12C), only 5 bilayer pairs appear to have been deposited. However, the total ML thickness in the growth direction of the area evaluated (Figure 3.14) is slightly

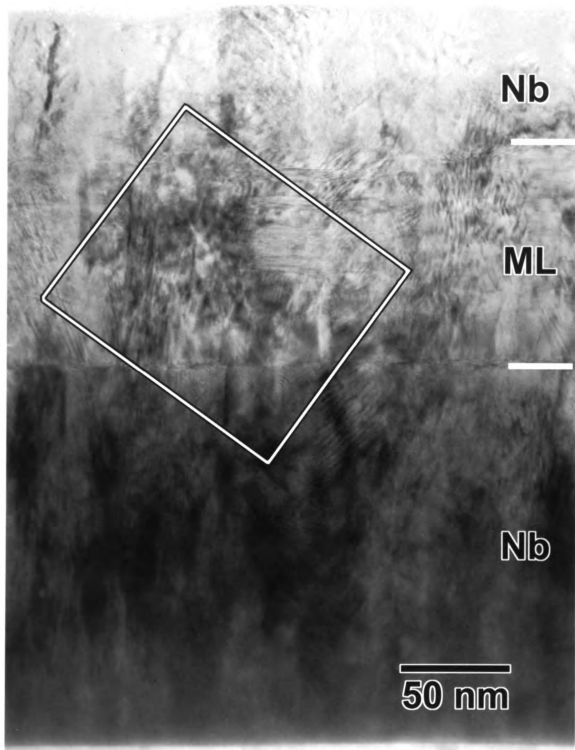


Figure 3.13. Low magnification HRTEM image of the cross-sectioned 20-2 sample. The ML area (ML) and lattice analysis area (inset) are shown.

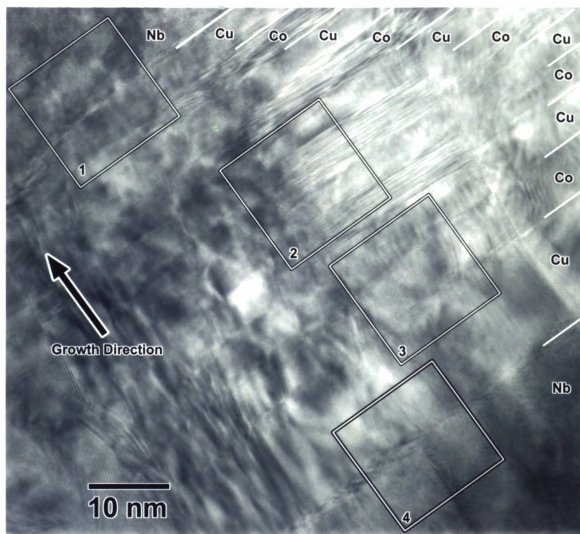


Figure 3.14. HRTEM of the ML 20-2. Four regions were selected for lattice analysis of the metal layers. Based on crystal diffraction contrast there appears to be 5 rather than 6 bilayers.

more than 100 nm, actually thicker than the 92 nm nominal thickness. Although there is some unevenness, as mentioned in the CTEM description, this overall dimension is consistent over extended ranges (*c.f.* Figure 3.12). Figure 3.15 is a region near the top of the ML stack and Figure 3.16 is in a region incorporating the intralayer transition to the striated horizontal contrast modulation. The areas analyzed in these two regions are presented in Figure 3.17.

The upper half of the micrograph in Figure 3.15 is the Nb capping layer and the presence of nearly uninterrupted lattice planes perpendicular to the growth direction is evident. In Figure 3.17A, a nearly perfect $[110]$ growth direction is seen in this area of the Nb layer. The FFT shows growth axis reflections consistent with the 0.2338 nm spacing of the Nb $\{110\}$ planes. The lower amplitude of the off axis $\{110\}$ reflections is due to the higher distortion in the off axis planes. At the Nb||Cu5 interface, an irregular band of lower contrast can be seen (Figure 3.15B). Figure 3.17B shows the enlargement of this area. The image dimensions were that of the previous area, to improve frequency sampling. The FFT shows the expected $(110)|| (111)$ growth-axis spots which are seen as a doublet, due to the 0.2338 nm Nb $\{110\}$ vs. 0.2084 nm Cu $\{111\}$ spacing. However, the spot due to the Nb $(01\bar{1})$ appears to be displaced towards the growth axis and is seen at 57° rather than the expected 60° . At 67° , a reflection consistent with a Cu $\{111\}$ frequency is seen. The final two spots, nearly co-radial, at 122° are at 0.18 and 0.23 nm are consistent with the Cu $\{200\}$ ||Nb $\{110\}$ relationship. The final area from the top of the ML analyzed

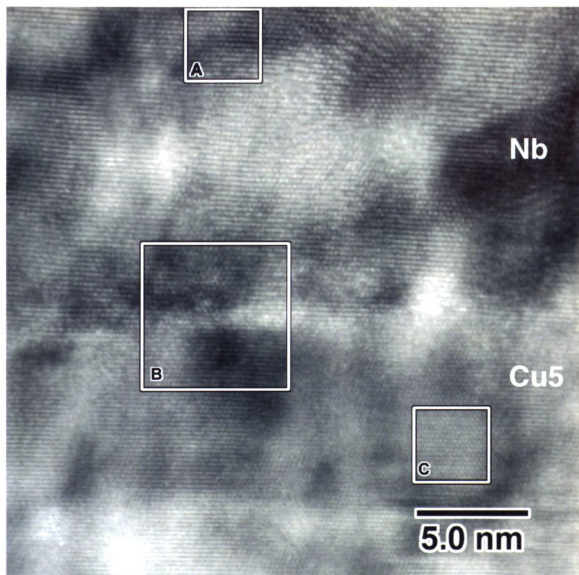


Figure 3.15. HRTEM of the upper region of sample 20-2. The image corresponds to the inset (1) from figure 3.14. The upper half of the region is the Nb capping layer.

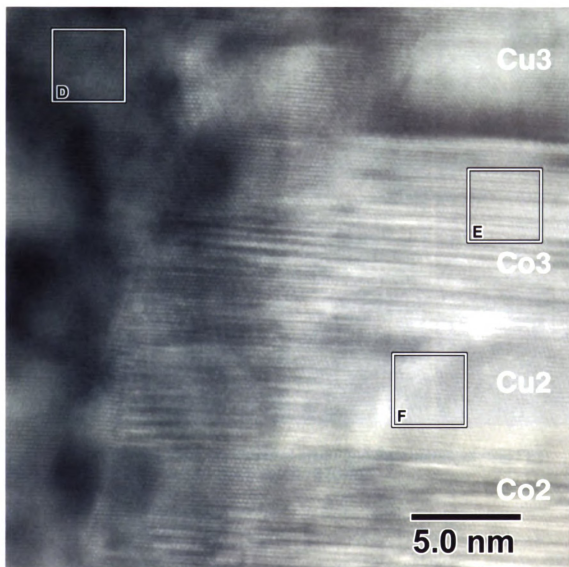


Figure 3.16. HRTEM of the middle region of sample 20-2. The image corresponds to the inset (2) from figure 3.14.

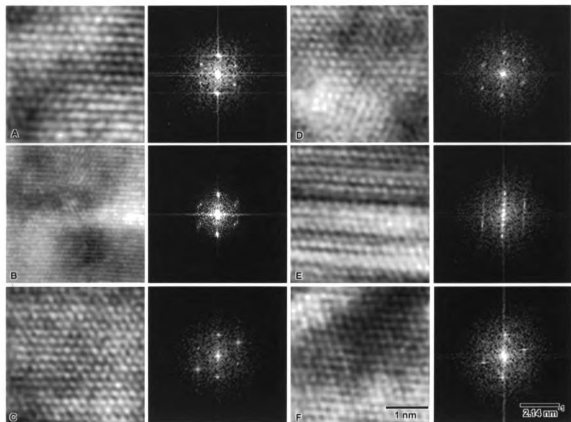


Figure 3.17. High magnification HRTEM areas and their corresponding FFT transforms from Figures 3.15 (A-C) and 3.16 (D-F).

be a nearly perfect example of the (111) growth of Cu expected.

In the middle region of the ML (Figure 3.16) distinctive differences in crystal structure are apparent within the individual layers. In the left side of this region, the crystal is consistent with a single fcc structure across the layer boundaries oriented, as expected, with the growth on the (111) planes of fcc Cu and Co. A representative area (Figure 3.16D) in layer Cu3 is shown in detail in Figure 3.17D. The image and its FFT are consistent with expected (111). Figure 3.16E shows an area of layer Co3 that exhibits extensive short-range contrast modulation in the growth direction. The high magnification image and its FFT (Figure 3.17E) show what appears to be extremely short range twinning on the (111) planes. The FFT shows a maximum growth-direction frequency consistent with the (111) planes of either Co or Cu (the bulk equilibrium spacings of 0.205 nm for Co_{fcc} and 0.208 nm for Cu cannot be differentiated with the sampling space used). Along the growth direction are two other sets of lower frequencies one corresponding to a frequency of twice the (111) spacing and to 5 times the (111) spacing. The contrast modulation responsible for these spots can be discerned in Figure 3.17E. The final area analyzed is shown in Figure 3.16F and the high magnification image is presented in Figure 3.17F. This area of the Cu2 layer shows a single crystal pattern with the expected [111] growth direction. The crystal in this area has its growth plane stacking switch from an "abcabc" to a "cbacba" motif compared to that seen in Figures 3.17D from the left side of the analysis area. Thus it appears as a mirror image with respect to the zone axis.

The first Co/Cu bilayer deposited on the Cu buffer layer showed little differential contrast with the Cu buffer layer (Figure 3.14 inset (3)). This region shown in, Figure 3.18, was chosen to compare the structures within the layers Cu1 and Co1. Figure 3.19A is a sample area in the Cu1 layer. It represents an essentially perfect domain with the expected (111) growth and equilibrium lattice spacings. The predominant defect in the Figure 3.18 region appeared to be small twins on the $(1\ 1\ \bar{1})$ planes (Figure 3.19B). In the Co1 layer (Figure 3.19C) the FFT shows additional spots at a frequency corresponding to twice the {111} spacing. Careful inspection of the Figure 3.19C image that generated this transform shows a subtle alternate plane modulation in contrast.

At the junction of the Cu buffer layer and the Co1 layer, there are regions of differential contrast across the boundary. However, the crystal orientation on either side is nearly the same. Some slight distortion may be present along the $(1\ 1\ \bar{1})$ at the interface as is evidenced by the fine splitting of the $(1\ 1\ \bar{1})$ spot in Figure 3.19D. Figures 19E and F are selections from the Cu buffer layer shown in the lower half of Figure 18. The growth throughout the buffer layer is in the [111] direction with little deviation from the orientation described above.

The quality of growth in the ML is sequentially dependent on the quality of the previously grown layer. The last region of the 20-2 ML (Figure 3.20) characterized is the lower part of the Cu buffer layer and the Nb interfacial region. In areas A and B from Figure 3.20, the regular spacing of the (111) planes seen throughout the area of the sample studied are evident. There is a slight

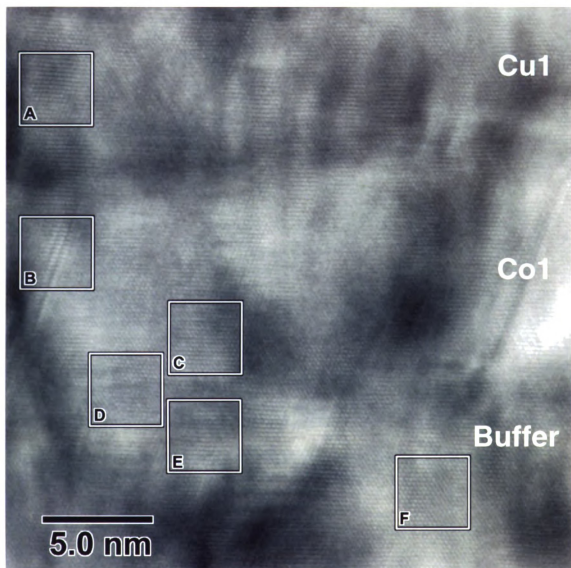


Figure 3.18. HRTEM of the first Co and adjacent Cu layers from sample 20-2. The area corresponds to the inset (3) from figure 3.14.

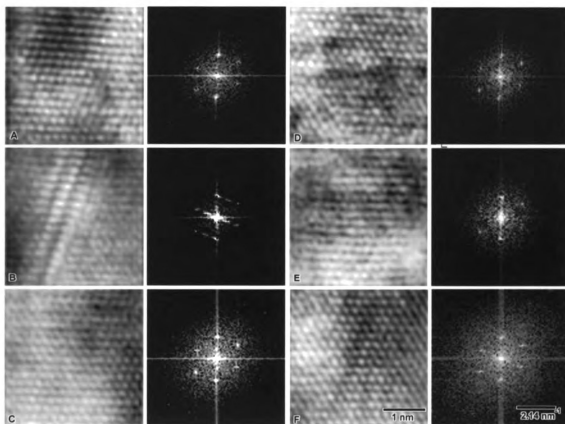


Figure 3.19. High magnification HRTEM areas and their corresponding FFT transforms from Figures 3.18 (A-C) and 3.16 (D-F).

difference in rotation along the $[1\ 1\ 1]$ in the buffer layer. The areas A and B of Figure 3.20 both show clear lattice images in the $[1\ 1\ 1]$ but only the area highlighted in B (*cf.* Figure 3.21 A and B) shows the (002) and $(1\ 1\ \bar{1})$ reflections. The interfacial region, seen in the middle of Figure 3.20, appears as an undulating band of contrast change. In the area selected for lattice analysis (Figure 3.21C) the growth direction spots correspond to spacings of 0.21 nm, consistent with the Cu $\{111\}$ spacing. The interfacial region, seen in the middle of Figure 3.20, appears as an undulating band of contrast change. In the area selected for lattice analysis (Figure 3.21C) the growth direction spots correspond to spacings of 0.21 nm, consistent with the Cu $\{111\}$ spacing. At 50° to the growth direction there is a strong frequency at 0.23 nm, consistent with the Nb $\{110\}$ spacing and at 110° from the growth direction there is a second spot at this spacing. This is consistent with a $\langle 111 \rangle$ viewing zone axis in the Nb layer. In Figure 3.21D, the Nb crystal can be seen to be imaged on a $\langle 111 \rangle$ zone as all lattice angles are 60° to each other and the spacing is the 0.23 nm consistent with the $\{110\}$ in Nb. Towards the center of the field of view in Figure 3.20, there is a band of increased contrast. An area (Figure 3.20 inset E) straddling this is analyzed in Figure 3.21E. The FFT of the area shows a set of frequencies, both corresponding to the Nb $\{110\}$ spacing, oriented at 46° and 60° to the growth direction spot (also Nb $\{110\}$ spacing). In the area to the right of the boundary, the area is oriented with the 46° motif (Figure 3.21F).

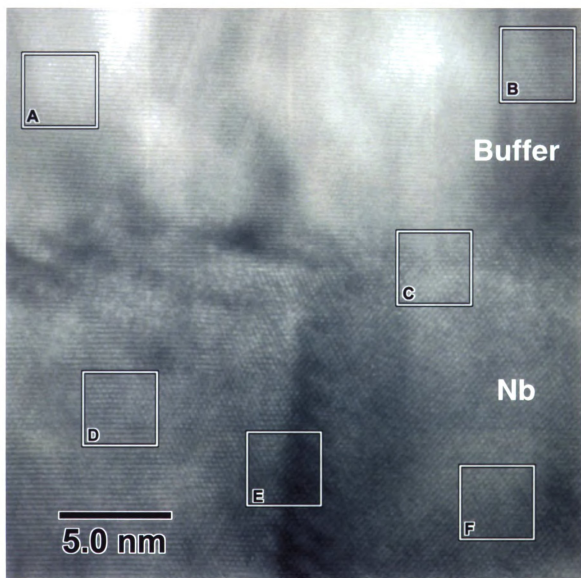


Figure 3.20. HRTEM of the Cu buffer layer and adjacent Nb base layer from sample 20-2. The area corresponds to the inset (4) from figure 3.14.

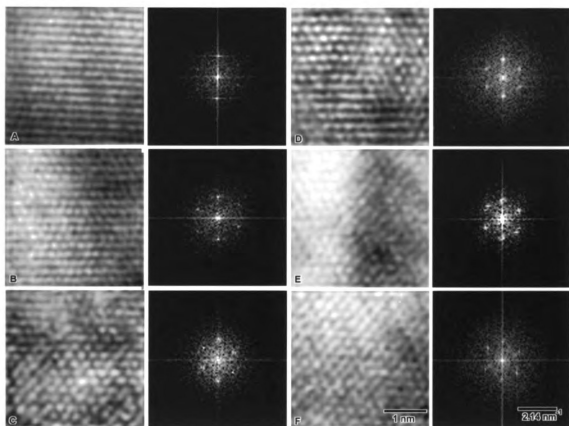


Figure 3.21. High magnification HRTEM areas and their corresponding FFT transforms from Figures 3.19 (A-C) and 3.16 (D-F).

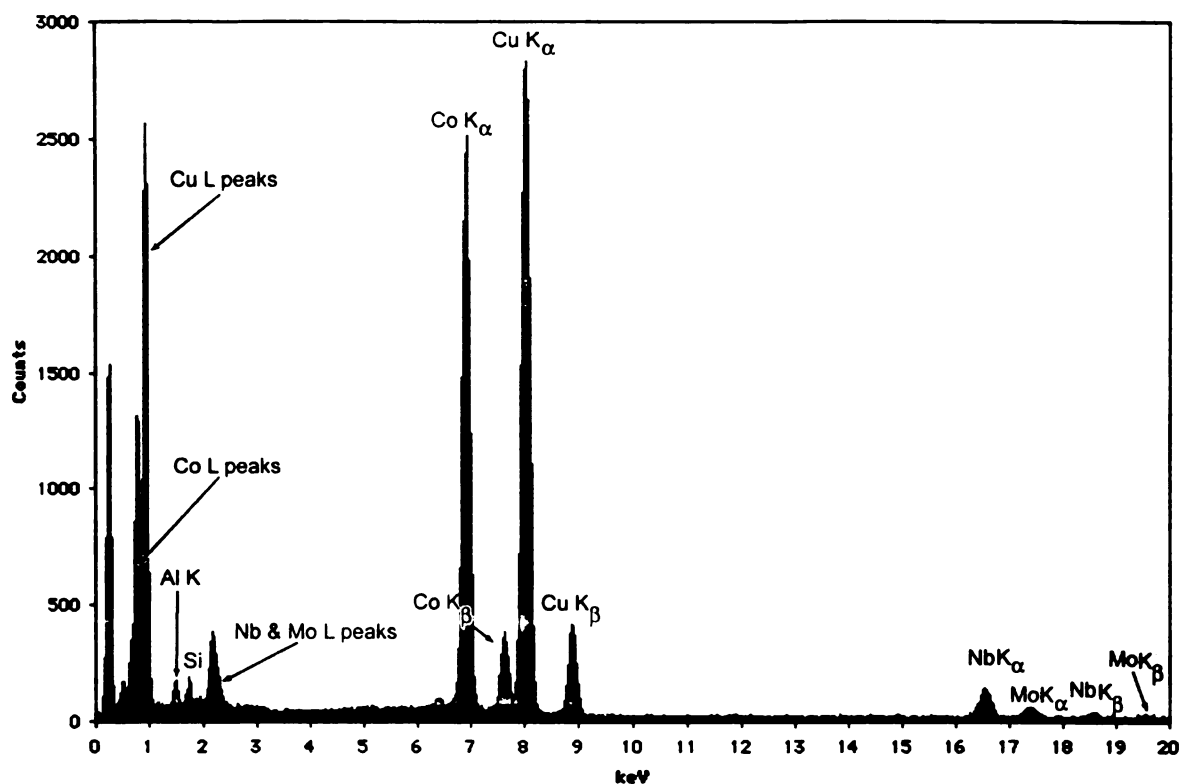


Figure 3.22. EDS spectrum from a cross-section of the 20-2 ML structure.

HREDS of Sample 20-2

Although sample 20-2 consisted of only 5 bilayers, the nominal volumetric proportions of Co and Cu were still very close to the 40 Co:60 Cu ratio seen for 6 bilayers. Figure 3.22 shows a 2 min spot mode spectrum collected under similar conditions to those used above for sample 20-1. The peak ratios for the Co and Cu K peaks are essentially the same as those for the simulated spectrum (Figure 3.10B).

Summary for sample 20-2

Sample 20-2, being grown exclusively at room temperature, provides an important comparison with sample 20-1 and the subsequent epitaxially grown samples. The overall contrast (Figure 3.2) and the overall ML uniformity seen in

CTEM mode implies that the deposition process *per se* does not appear to be responsible for the growth anomalies seen in sample 20-1. Similarly, since the general highly textured polycrystalline growth observed is consistent with that reported by others, it is doubtful that the structures seen in sample 20-1 resulted from TEM sample preparation artifacts. Foils from both samples were prepared by essentially identical methods.

The overall Co-Cu composition, based on qualitative evaluation of the Co and Cu K peaks was nearly identical to the simulated ratio. Although the low interlayer contrast prevented spot-mode layer by layer analysis, there were indications of compositional layering due to crystal diffraction.

Throughout the ML and buffer layer, the Cu grains oriented to yield lattice images had an apparently low defect density. Co layers, on the other hand, had a high density of stacking faults in the growth plane that HRTEM images suggest increases towards the center of the layer, away from the interfaces. This appears to be due to a tendency for the fcc Co to revert to the hcp, a phenomenon commonly seen in relatively thick Co layers. The Nb layers forming the capping layer and the base layers for the ML also were strongly textured in the growth direction. Most grains were found to be within just a few degrees of the overall growth direction.

3.3 Sample 20-3 (epitaxial)

The third sample prepared from the studied sputtering run (20-3) was grown with a different temperature regimen than the first epitaxial sample (20-1). While the Nb base layer was applied under the same conditions (as shown in table 2.1), the Cu buffer layer was applied at a higher temperature (450°C) and was given no post deposition anneal in contrast to the Cu buffer layer in 20-1. The rest of the ML was deposited at 90°-100°C.

CTEM

In contrast to the continuous film morphology seen with samples 20-1 and 20-2, sample 20-3 had a discontinuous morphology above the Nb base layer (Figure 3.23). This bottom Nb layer appeared qualitatively similar to that seen in 20-1 (Figure 3.1) and was close to the nominal 250 nm thickness. The brightfield image (Figure 3.23a) shows that the entire Cu seed layer and ML stack was broken into island-like regions. The SAED pattern and dark field image confirm that the ML, with the exception of the capping Nb layer, was nevertheless highly $\langle 111 \rangle$ textured, if not entirely epitaxial. The combined Co/Cu strata of the ML varied in total thickness by 85 nm. The thinnest regions were 73 nm and the thicker areas as much as 158 nm, with the mean thickness being 124 nm. The islands, viewed in cross section, had an average width (along the ML) of 374 nm. The layering was especially evident in these island regions (Figure 3.23C) when viewed at a high objective lens defocus. The Cu buffer layer in these regions had three distinct morphologies. In some areas there were anomalously thick buffer layers. These generally subtended what appeared to be the clearest

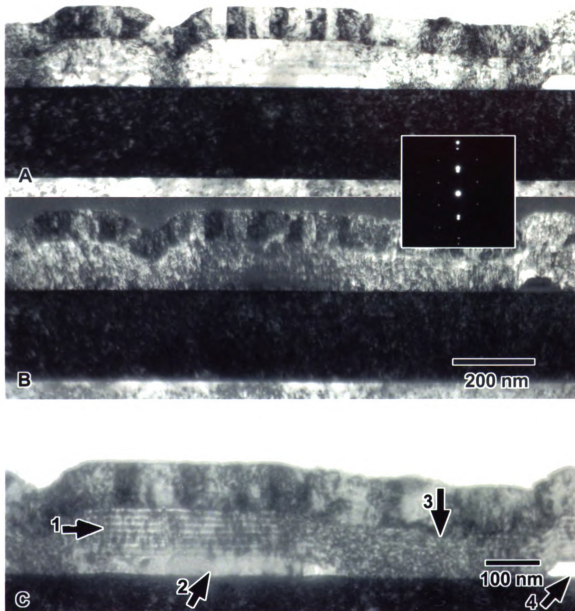


Figure 3.23. CTEM images of sample 20-3. A) Single beam brightfield image of a cross section of the 20-3 ML. B) The darkfield image obtained with the Nb (010) reflection. C. A single-beam brightfield image focused 11 μm below the minimum contrast setting. Arrows 1-4 highlight a prominently layered region, an anomalously thick buffer region, a region apparently *sans* buffer layer and an apparent hole, respectively.

layering (Figure 3.23C). In other areas, often adjacent to the islands, the buffer layer appears to be absent, with the remainder of the ML in direct contact with the Nb base layer. In these areas, Fresnel defocus contrast reveals the persistence of layering in the remaining ML. A third layering variation observed was the complete lack of contrast and apparent voids subtending regions of some of the islands. Fresnel contrast also indicates that most of the differences in total ML thickness is due to local differences in the Cu buffer layer.

HRTEM of sample 20-3

Two regions of interest in this ML were also examined using high resolution transmission electron microscopy. The first area is of a region showing an island-like structure and the second is the area surrounding an apparent hole (Figure 3.24). Images were recorded near the JEOL 4000 EX Scherzer defocus (-52 nm) from thin areas that were far enough from the thinned edge to have a complete ML device cross section remaining. As before, the HRTEM magnification calibrations were made using Nb lattice images, from areas within the micrograph. Figure 3.25 is a HRTEM image of the area for analysis of the ML, taken from a typical island area (Figure 3.24A (inset)). In this region the Cu buffer layer is 70 nm thick, 3.5 times the nominal value. The rest of the ML ($(\text{Co}_{6 \text{ nm}}/\text{Cu}_{6 \text{ nm}}) \times 6$) is 76 nm, which is in good agreement with the 72 nm nominal dimension. Although the ML cross-section had been aligned to within a degree of the sapphire [0001] in the microscope, structural images were only apparent in the upper and lower Nb layers and some of the areas of the Cu buffer layer.

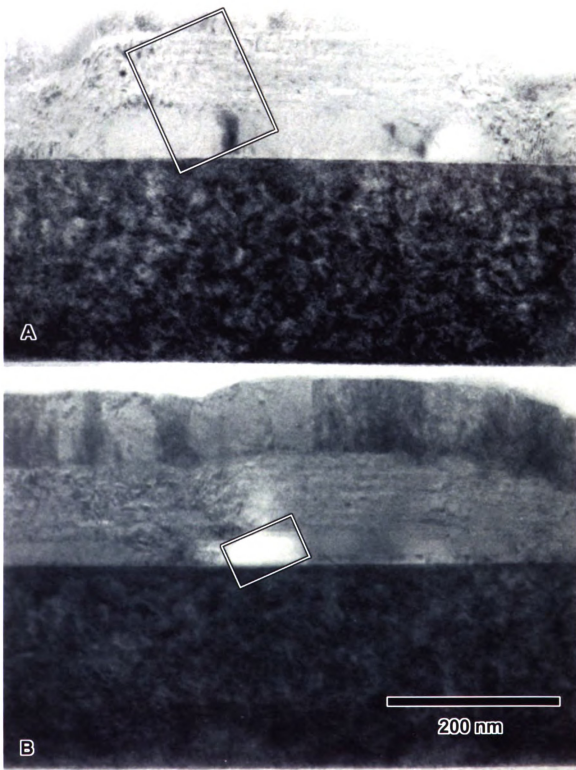


Figure 3.24. CT-TEM image of the cross-sectioned 20-3 sample. A) An area within an island. B) The area around an apparent hole.

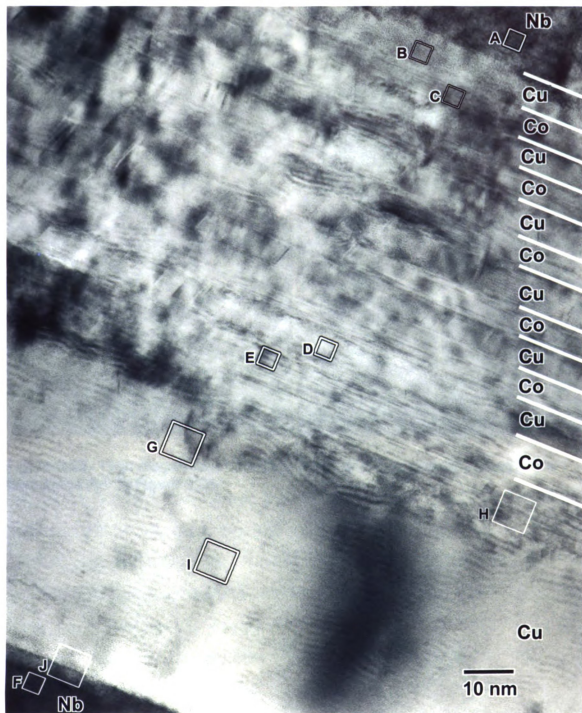


Figure 3.25. HRTEM image of an island area of 20-3 selected for structural analysis. Areas A-F are representative areas of the upper and lower Nb layers and the first and last Co/Cu bilayers.

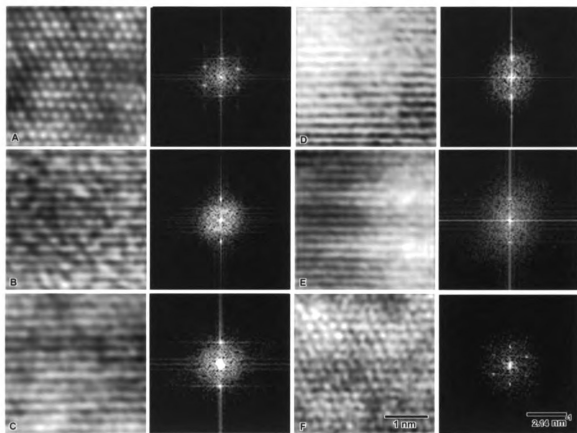


Figure 3.26. High magnification HRTEM areas and their corresponding FFTs from areas A-F in Figure 3.25.

However, the ML stack showed prominent layer delineation in the region over the Cu buffer island. This appeared to be due, in large part, to diffraction from the same intralayer faulting seen in the Co layers in some areas of specimen 20-2. Figure 3.26 shows the images and FFTs from areas A-F in Figure 3.25. Although structural images were obtained from the Nb regions above and below the ML, the only discernable lattices evident in the Co/Cu strata of the ML were attributable to the (111) planes of fcc Co and Cu. The effect is shown here for both the first and last bilayer pairs (*cf.* Figure 3.26 B,C and D,E). The buffer layer was analyzed in four areas (Figure 3.25G-J). These were selected to investigate the most obvious areas with contrast differences in them. The areas selected were twice the dimensions (6.6 nm X 6.6 nm) of those selected for the bilayer region of the ML. An area showing anomalous contrast is seen in Figure 3.27G. This figure shows a prominent reflection a spacing of 0.20 nm, which is consistent with the fcc {111} spacing for Co (0.205 nm) and very near that for Cu (0.208 nm). This spot has a diminishing tail through a rotation of about 20° from the growth direction. This tail also has a diminishing radius, in the FFT, implying a dilatation of the lattice spacings with angle from the growth direction. There is a second spot that corresponds to a lattice spacing of 0.24 nm which is about 4% less than the {110} spacing for Co and 6% less than the Cu {110}. In addition to these spots, there is a second weaker set of reflections at 118° from the growth axis, which may be a second set of {110} reflections. However, these lattices should not be visible along the [110] zone axis. The second inset in the Cu buffer layer (Figure 3.27H) is from an area very near the Co1 boundary. In the image, there is a slight periodic modulation in contrast along the growth direction and the FFT shows the same arrangement of reflections as did area G above. However, the 0.24 spots are fairly distinct and are on the growth axis. This implies that the modulation is a moiré effect. This is

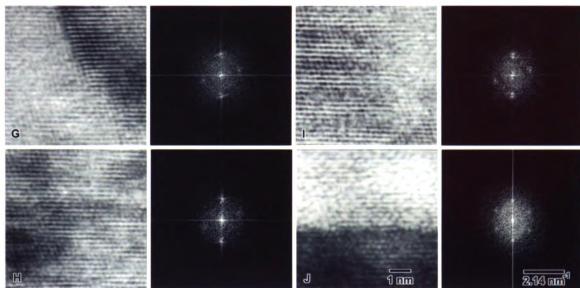


Figure 3.27. High magnification HRTEM areas and their corresponding FFTs from areas G-J in Figure 3.25.

further supported by the image in Figure 3.27I. The HRTEM shows a clear periodic contrast modulation and the FFT from this region shows the two interfering spots and the pair of spots near the center of the FFT which correspond to the period of the fringes. Figure 3.27J, an area spanning the Cu buffer||Nb interface shows an interesting transform. The growth direction spots are fairly sharp and correspond to lattice spacings of 0.22 nm. This is intermediate between the 0.234 nm Nb{110} spacing and the 0.208 Cu {111} spacing. At angles of 56° and 117° there are two additional spots corresponding to the Nb{110} spacing.

In addition to the buffer layer morphology described above, some areas, under some "islands", appeared to be voids when viewed in CTEM (Figure 3.23C, arrow 4). One such area was isolated for HRTEM (Figure 3.24B). Under HRTEM conditions, this area can be seen to consist of a hole surrounded by areas of differing structure (Figure 3.28). Similar moiré patterns are seen, near the hole, as were seen in the previous island Cu buffer layer HRTEM image. In Figure 3.29A, a reference area from the Co1 layer is presented. It shows the common growth-direction lattice fringes and the FFT confirms a 0.20 nm spacing consistent with the {111} growth of the Co_{fcc}. The area in Figure 3.28 inset (B) is enlarged in Figure 3.29B. It has a contrast intermediate between the Co1 layer and the hole and both the image and the adjacent FFT show no indication of periodic structure. The structure seen in Figure 3.29C is similar to that seen in the middle of the Cu buffer layer in the island. There are a series of moiré fringes arising from reflections having the same spacing and on-axis orientation as that

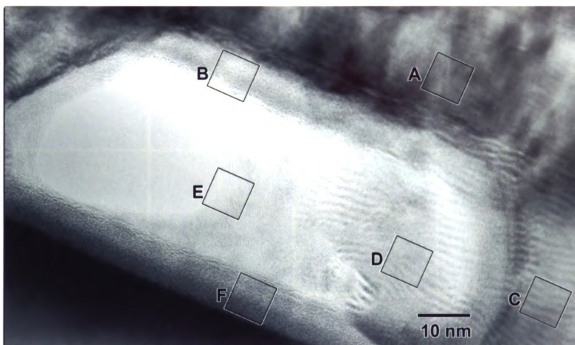


Figure 3.28. A HRTEM image of a Cu buffer layer hole and surrounding area from sample 20-3.

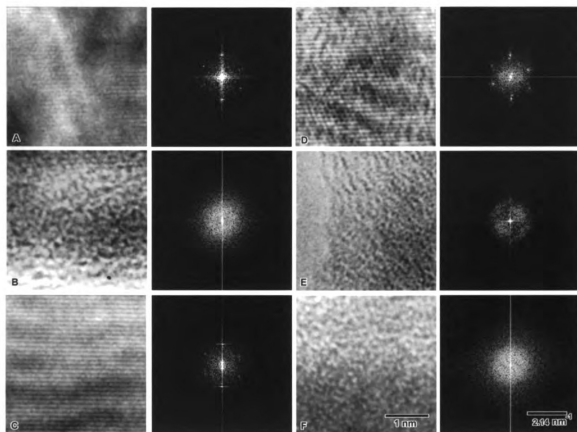


Figure 3.29. High magnification HRTEM images and their corresponding FFTs. from areas around the hole shown in Figure 3.28

seen in Figure 3.26. The area in Figure 3.28 inset (D) has 5 pairs of lattice spots and a set of low frequency moiré spots. Along the growth direction, the 0.21 Cu {111} spacing is evident as is a coaxial inner pair, corresponding to a lattice spacing of 0.24 nm. A similarly spaced pair is evident at 107° from the growth direction. At 55° from the growth axis, there are two more spot pairs. These are at 0.20 nm and 0.18 nm. These are similar to the Co {111} and Cu {200} spacings respectively. The order disappears in the image near the margin of the hole as shown in Figure 3.29E and along the buffer layer Nb boundary (Figure 3.29F)

Summary for sample 20-3

Sample 20-3, the second epitaxial sample studied, differed markedly from the first epitaxial sample (20-1). The most striking feature is the presence of a grossly discontinuous Cu buffer layer. This layer appears as a series of islands across the Nb base layer. The Nb base layer was, in fact, the only feature even qualitatively similar to sample 20-1. The Cu buffer layer islands were variable. Some of the islands had holes, or apparent holes, that seem to have formed after the start of ML fabrication, since there are areas where a continuous ML can be seen following the hole contour. In the Cu of both the continuous islands and those with holes in the Cu buffer layer, numerous moiré fringes were seen. These fringes appear to arise from the overlap of crystals not oriented with their closest packed planes along the growth axis. Around island areas with holes, the crystalline Cu buffer layer appeared to taper down towards the hole margin, finally appearing amorphous at the lateral margin of the holes. At the upper

(Cu||Co interface) and lower (Cu||Nb interface) margins of the hole diffuse layers of intermediate contrast, with no apparent lattice structure are seen. These interfacial features are not seen in the island areas with continuous buffer layers.

The ML stack in sample 20-3 showed a interlayer contrast that appears to arise from the same $\text{Co}_{\text{fcc}}-\text{Co}_{\text{hcp}}$ strain relations that gave the interlayer contrast in 20-2; that is a tendency towards reversion to the hcp Co structure. However, the ML region analyzed was not optimally oriented for full structural analysis.

3.4 Sample 20-4 (epitaxial)

The last sample from the studied sputtering run was fabricated with yet a different temperature regimen. As shown in Table 2.1, the Nb base layer was applied at an elevated temperature and given post deposition annealing identical to samples 20-1 and 20-3 described above. The Cu buffer layer was also applied at an elevated (450°C) temperature. However, in contrast to the second epitaxial test (20-3), the Co1 layer was deposited at 490°C, rather than the 90°-100°C regimen of the previous sample. The remainder of the ML was deposited at 90°-100°.

CTEM of sample 20-4

Sample 20-4 had a discontinuous morphology above the Nb base layer, like sample 20-3. The Nb base layer was similar to that seen in the other two epitaxial samples (20-1 and 20-3), but measured 180 nm thick. The brightfield image (Figure 3.30A) also shows that the entire Cu seed layer and ML stack were again broken into islands that had a mean length of 257 nm when viewed in cross-section. The SAED pattern (*cf.* insets Figure 3.23 and 3.30) was essentially the same as that recorded for the previous sample and the darkfield image shows similar defect contrast (Figure 3.30B). There were some lapses in continuity in the layers of this sample, that resulted from faults that passed through the entire ML to the Nb layer surface. The total ML thickness averaged 106 nm with a maximum of 122 nm and a minimum of 0 nm (at the trans-ML faults). As with sample 20-3, there were distinct buffer layer morphologies. In some of the island structures, a dilated buffer layer was present.

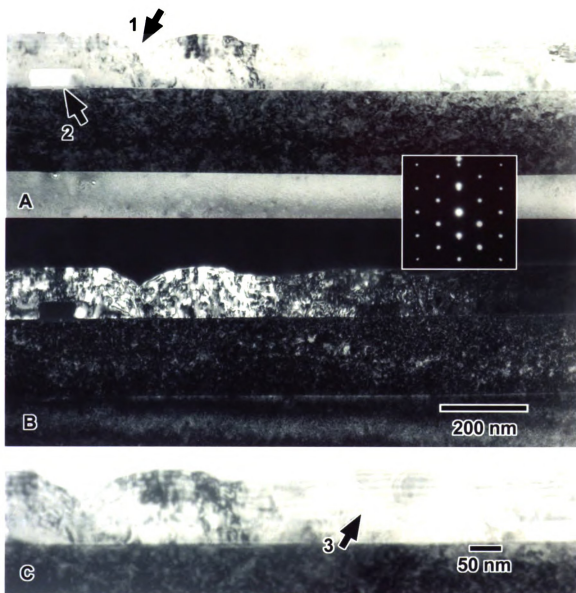


Figure 3.30. CTEM images of sample 20-4. A) Single beam brightfield image of a cross section of the 20-4 ML. B) The darkfield image obtained with the Nb (0T0) reflection. C) A single-beam brightfield image focused 11μm below the minimum contrast setting. Arrows 1-3 highlight: A region apparently *sans* buffer layer, an apparent hole, and a prominently layered region, respectively.

In other areas (Figure 3.30A, arrow 2) holes were present. In yet other areas, the ML had no apparent buffer layer. Imaging at high defocus (Figure 3.30C) revealed layers, that were the most uniform on the broader islands (Figure 3.30C, arrow 3), but present throughout the ML. The capping layer appears as an apparently amorphous film, rather than the expected 100 nm Nb layer (*cf.* Figures 3.23-3.30).

HRTEM of sample 20-4

An area from a typical island in this ML was examined using HRTEM. As before, images were recorded near the JEOL 4000 EX Scherzer defocus (-52 nm) from thin areas that were far enough from the thinned edge to have a complete ML cross-section remaining. The HRTEM magnification calibrations were made using Nb lattice images contained this area. The FFT analyses were done using 3 to 6 nm scaled areas from constant magnification micrographs. Figure 3.31 is a HRTEM image of the area for analysis of the ML, showing the typical island area from which it was taken. In this region the Cu buffer layer is 43 nm thick, roughly twice the nominal value. The exact location of the Cu buffer layer Co1 interface is difficult to discern. The rest of the ML ($(\text{Co}_{6\text{ nm}}/\text{Cu}_{6\text{ nm}}) \times 6$) is 81 nm, which is in good agreement with the total ML thickness seen in sample 20-3 nm and in reasonable agreement with the expected thickness of 72 nm. The ML cross-section was aligned to within a degree of the sapphire [0001] in the microscope and structural images were apparent in all layers. Figure 3.32 shows the HRTEM analysis area and the sampling areas within it insets (A-M). Good

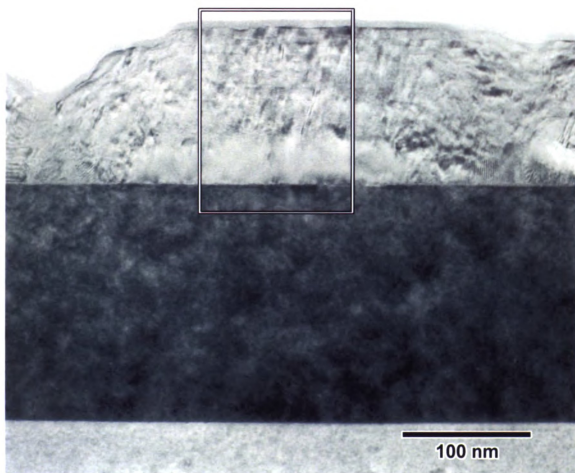


Figure 3.31. Low magnification HRTEM image of the cross-sectioned 20-4 sample. The area within a typical island chosen for structural imaging is outlined.

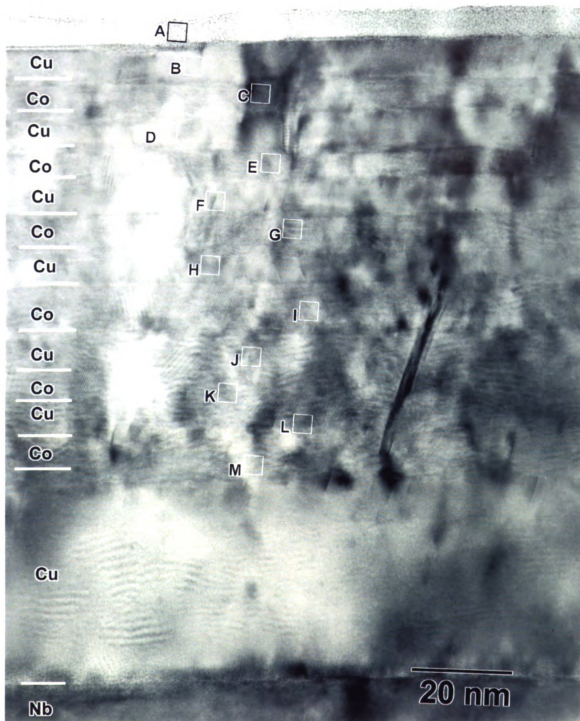


Figure 3.32. HRTEM image of an island area of 20-4 selected for structural analysis. Areas A-M are representative areas throughout Co/Cu bilayers.

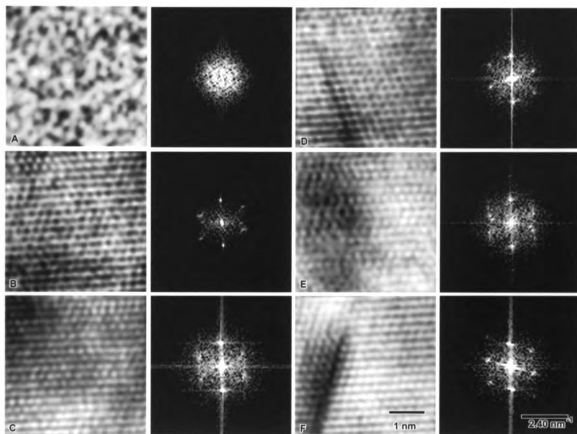


Figure 3.33. High magnification HRTEM areas and their corresponding FFTs from areas A-F in Figure 3.32.

structural images were obtainable from representative areas across the ML. All areas in the ML oriented to display ordered structure showed the sharpest frequency along the (111) planes of fcc Co and Cu.

The topmost layer, which should have been the 100 nm Nb capping layer, appeared as a thin (5 to 6 nm) apparently amorphous layer (Figure 3.33A). The Cu₆ layer (of the last deposited bilayer pair) grew as a single crystal at least across the range of the HRTEM area viewed (≈ 125 nm). The Co₆ layer, of this last bilayer pair, showed a transform that indicated the presence of hcp Co towards the center of the layer in some regions. The spacing in the growth direction appears the unaffected, but this may be below the resolution level of the sample size used. The Cu₅ layer was clearly fcc but the area sampled was oriented as if twinned on the [111] growth axis compared the Cu₆ layer (Figure 3.33D). In the Co₅ layer, the arrangement of atomic layers is more complicated (Figure 3.33E). There is a strong growth-direction spot with the expected spacing of 0.21 nm. At 55° to this is a very weak spot corresponding to 0.18 nm which is expected for a {200} plane spacing. At 72° there is another spot at the 0.21 nm spacing, which implies that a twin is imaged in the field of view. Finally, at 78° there is a pair of spots that correspond to a spacing of 0.25 nm, which is approximately the {110} spacing for Cu or Co, fcc. The angular relationship and existence of this frequency in the zone viewed are less clear. The Cu₄ layer, excerpted in Figure 3.33E, shows the identical structure to that seen in figure 3.33D, except that the overall stacking has changed from the abcabc to the cbacba (a simple twin relationship).

This pattern of nearly equilibrium Cu layers and more disordered Co layers is also seen in bilayers 3 and 2 (Figures 3.33H-K). Layers Cu1 and Co1 are hard to distinguish. The areas shown in Figure 3.33 L and M appear nearly uniform when viewed in the context of the whole HRTEM area (Figure 3.32). However, even in the Co1 layer (which was deposited at 450), the HRTEM image and FFT (Figure 3.34M) show there are lattice images and frequencies inconsistent with a completely fcc structure. In addition to the prominent growth direction lattices which have spacings (0.20 nm) exactly consistent with the $\text{Co}_{\text{fcc}} \{111\}$, there is an additional pair similarly spaced at 70° and a pair at 125° spaced at 0.18 nm. This implies a perfect $\{111\}$ fcc growth motif for the Co1 layer. However, there is an additional set of spots 102° from the growth direction (38° from the $(1\ 1\ \bar{1})$ spot). These correspond to a lattice spacing of 0.22 nm which is consistent with the $\{1\ 0\ \bar{1}\}$ spacing in the Co_{hcp} motif, although the angles from the growth direction differ by 8 degrees. Thus it appears that in both the epitaxial and polycrystalline Co||Cu layers 6 nm thick exhibit significant hcp character.

HREDS of sample 20-4

To determine local elemental composition in this sample, HREDS spectra were collected from selected areas of the ML and over the whole layer stack, as was previously shown for sample 20-2. The results of this acquisition are shown in Figure 3.35. The $\text{Cu } K_\alpha / \text{Co } K_\alpha$ ratio differed from the theoretical (*cf.* Figure 3.11B) by less than 6%. In addition to the overall spectrum, attempts to collect spectra from individual layers and regions in a representative island showing a

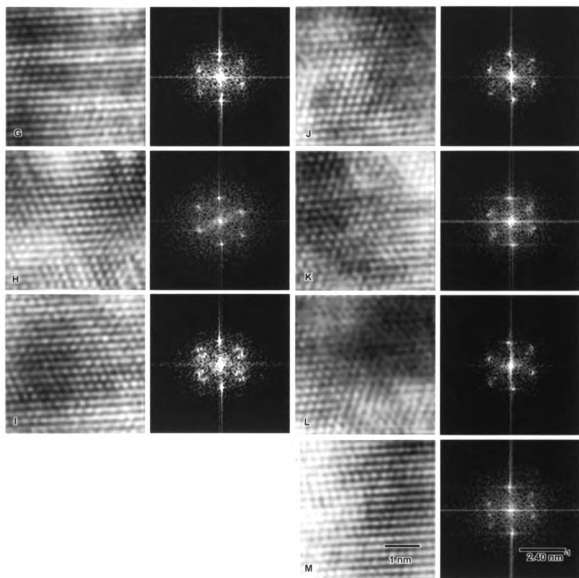


Figure 3.34. High magnification HRTEM areas and their corresponding FFTs from areas G-M in Figure 3.32.

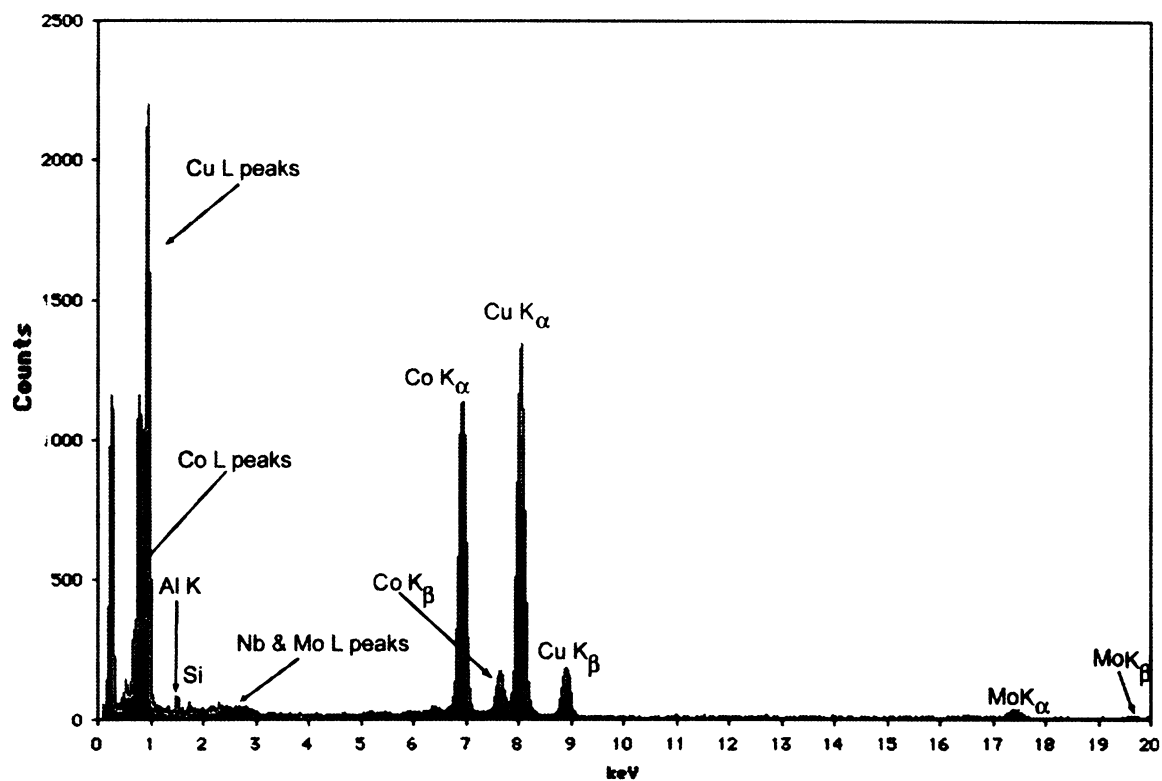


Figure 3.35. An EDS spectrum collected from the whole ML cross-section of sample 20-4. The collection time and beam parameters were essentially the same as those used previously.

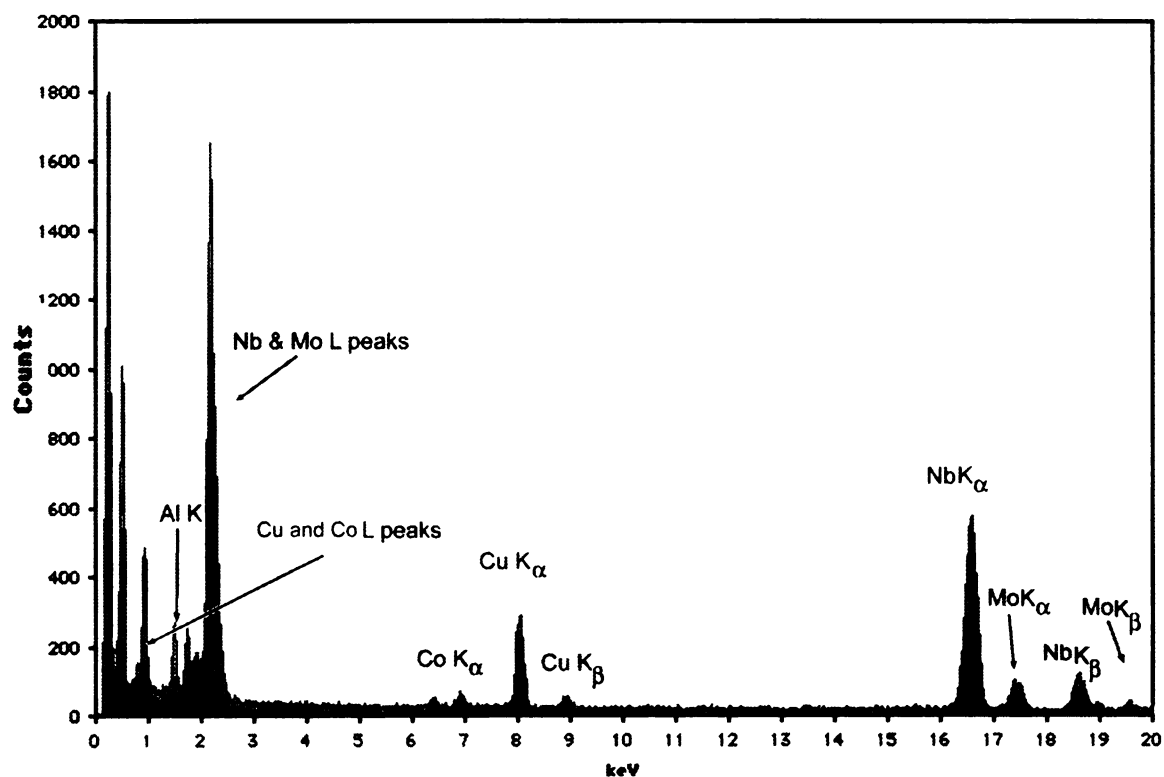


Figure 3.36. An EDS spectrum from the top amorphous layer covering the ML.

combination of the hole and solid structure were made. Figure 3.36 shows the spectra of the amorphous layer above the MLs in an island having a hole in the Cu buffer layer. This layer was structurally identical to the area seen in Figure 3.32 (inset A). The spectrum showed mostly Nb in spite of the generally structureless character observed.

Individual layers in the ML were hard to discern on the viewing screen when the beam convergence angle and spot size were in the analytical mode. To properly position the probe on specimen, the image (objective lens) needed to be near focus and there were few visual clues to the position within the ML. Nevertheless, representative spectra were recorded for a bilayer pair (5) near the top of the ML (Figure 3.37). The upper (Cu) layer in the pair shows some Co content in the sampled volume, but this may be due to the afore mentioned difficulties in aligning the probe in the middle of a Cu layer. The lower total Cu counts may be due to slightly different beam geometry or an effect of the reduction in sample thickness in the beam direction towards the top of the ML. The Co layer below the Cu layer shows a spectrum rich in Co and having a small amount of Cu in it.

A final area tested with HREDS was near the margin of a Cu buffer-layer hole. The structure probed is visible towards the margin of Figure 30.3A (arrow 2). The structure of this hole was essentially the same as that seen for sample 20-3 (Figure 3.28). The EDS spectrum (Figure 3.38) shows a nearly pure Cu buffer-layer with traces of Al, O, Co, Nb, and Mo. These were most likely re-deposited from elsewhere on the sample during the ion milling process.

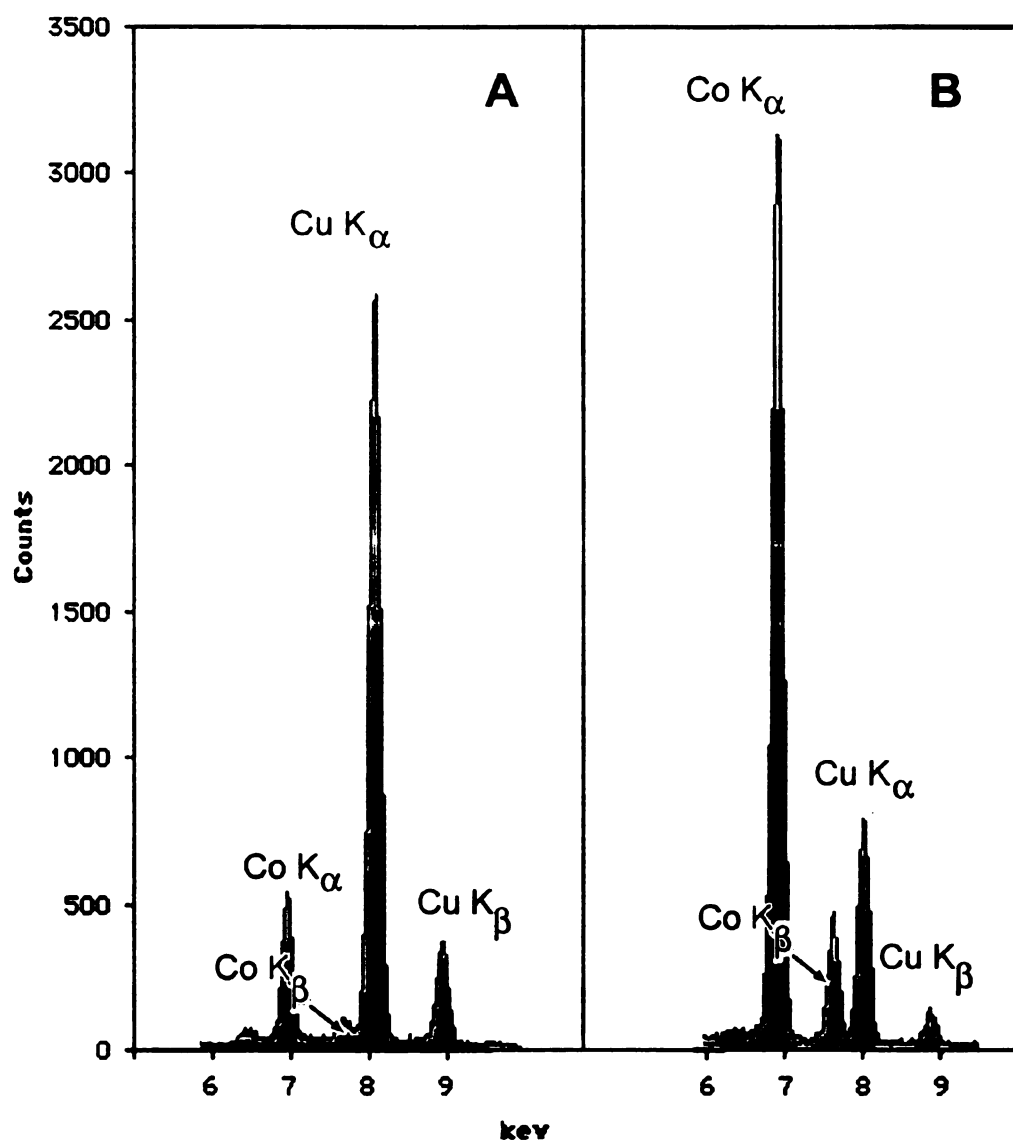


Figure 3.37. EDS spectra from adjoining Cu and Co layers near the top of the ML. A) A Cu layer and B) a Co layer.

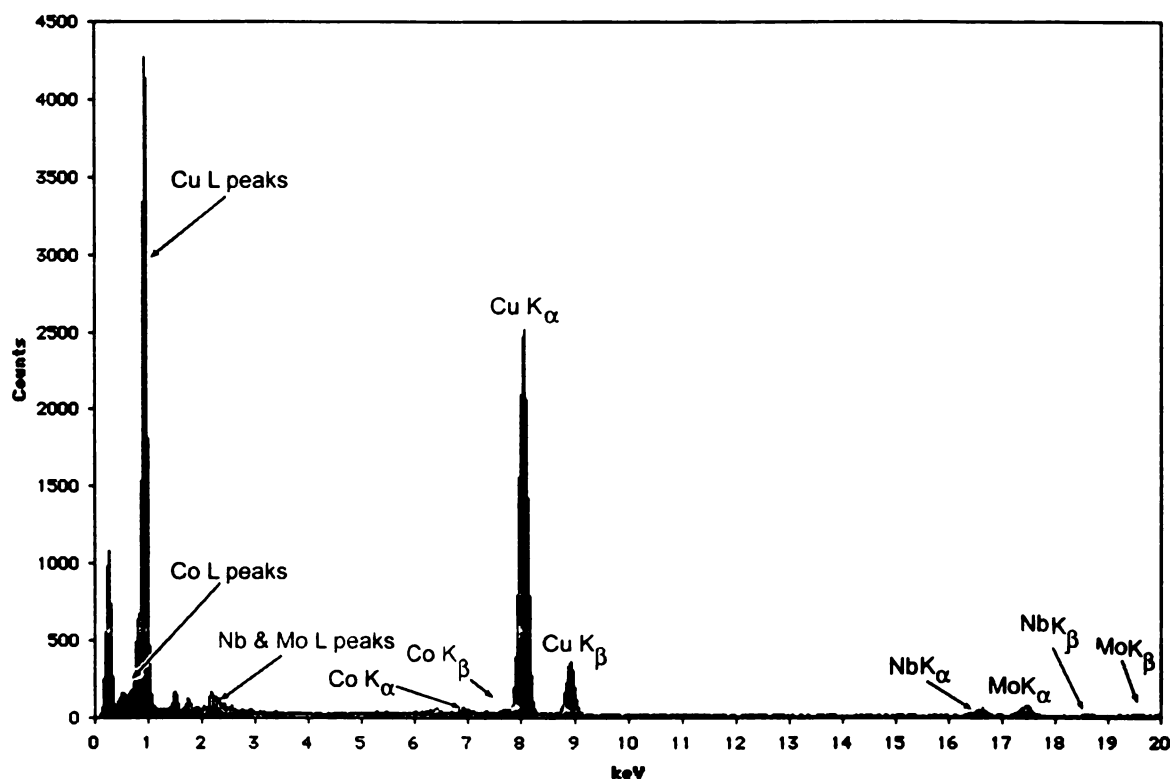


Figure 3.38. An EDS spectrum from the Cu buffer layer of sample 20-4.

Summary for sample 20-4

Sample 20-4, the final epitaxial ML sample studied, also differed markedly from the first epitaxial sample, 20-1. As with sample 20-3, the presence of a grossly discontinuous Cu buffer layer, appearing as a series of islands across the Nb base layer, is its most striking feature. The Cu buffer layer islands were variable within the sample and very similar to those seen in 20-3.

The ML stack in sample 20-4 showed interlayer contrast similar to but less pronounced than that seen in that sample 20-3. However, in sample 20-4, structural images were seen throughout the ML. The Cu appeared to alternate in stacking order on either side of a Co layer and all layers appeared to be growing on the {111} planes with occasional stacking faults evident. All of the Co layers

displayed lattice images, especially near the middle of the layers, where the growth appeared to switch to an hcp stacking. Thus, much of the layer contrast appears to arise from the same $\text{Co}_{\text{fcc}}\text{-Co}_{\text{hcp}}$ strain relations that gave the interlayer contrast in 20-2, and 20-3. HREDS of the sample showed that the overall composition is consistent with the modeled ML system. The topmost Nb (capping) layer was not well formed. It appeared as a thin (5-6 nm) amorphous layer that was mostly Nb but also contained significant Cu.

3.5 Samples 19-3 and 19-4 (epitaxial bilayers)

In an attempt to further understand the events that lead to the anomalous structure of the ML devices, two Cu/Co bilayers, prepared as initial test examples, were also prepared for cross-sectional TEM analysis. These samples consisted of a single layer of Cu, 20 nm thick and a single layer of Co, also 20 nm thick, deposited on a Nb epitaxial layer (Table 2.1). In both samples, the Cu layer was deposited at an elevated temperature (350° and 470° C for 19-3 and 19-4 respectively). In sample 19-3 the Co layer was deposited at 450°C while in 19-4 the Co was deposited at 100°C.

CTEM of samples 19-3 and 19-4

In both of these samples, as with the epitaxial ML samples, the Nb base layer grew as a continuous crystal (Figure 3.39), with a high defect density. The thickness of this layer was 239 nm in sample 19-3 and 165 nm in sample 19-4. Cross sections of both samples showed an island-like morphology. The upper layer of Co, which grew over the Cu islands and the intervening surface, was within 5% of 20 nm thick in both cases and nearly continuous. The islands in 19-

3 covered 62% of the observed surface and were approximately uniform in height with edge angles of $\approx 45^\circ$ from the Nb surface normal. The Cu layer height was 49 nm (Figure 3.39A). The islands in 19-4 covered 69% of the observed surface and the nominal Cu layer height was 62 nm with island edge angles of $\approx 60^\circ$ from the surface normal. In both samples islands were seen that varied in internal contrast, with some appearing to have voids or amorphous areas in either part or all of the island (similar to 20-3 and 20-4). At the base of the islands a thin (≈ 5 nm) uniform layer is visible in the CTEM micrographs (e.g. Figure 3.39). A typical island, having a region of nearly continuous Cu with apparent "holes" included in the island, was chosen for HRTEM analysis (Figure 3.39C). The island was 350 nm along the plane of the bilayer and stood 75 nm above the Nb base layer.

HRTEM of sample 19-4

Three zones were chosen for analysis within the island structure chosen. Figure 3.40 illustrates the area outlined as inset (1) in Figure 3.39C. At this magnification, the "hole" area can be seen to be a continuous thin film. In addition, the Co layer on the top of the island and that covering the Nb adjacent to it can be seen to have markedly different dominant crystal defects. Six representative areas were selected from this side of the island, These areas and their FFTs are presented in Figure 3.41.

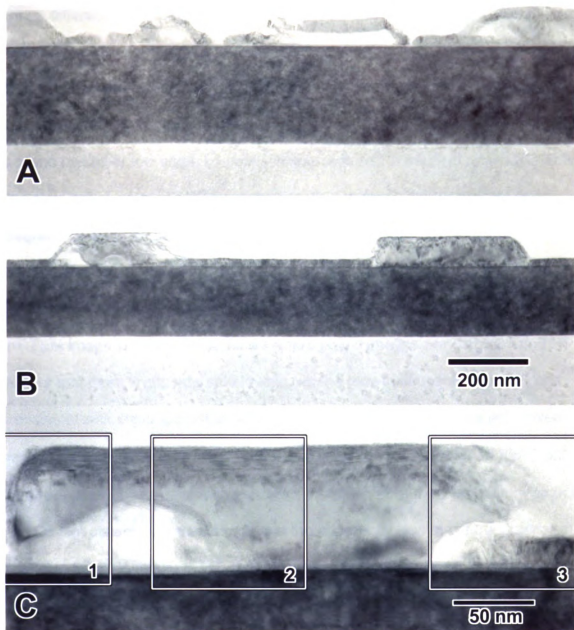


Figure 3.39. Brightfield CTEM cross-section images of samples 19-3 and 19-4. A) Sample 19-3. B) Sample 19-4. C. An island structure from sample 19-4 showing three regions analyzed via HRTEM.

The areas selected were 512 X 512 pixels (about 13 nm square) to capture short range differences in order. Figure 3.41A corresponds to the top Co layer on the island. The transform shows the very prominent lattice repeat at 0.20 nm , which is consistent with the fcc {111} or the hcp {0002} spacing. There is a second pair of spots, 10° from the growth direction at the same spacing, perhaps due to a second crystal or low angle boundary being captured in the field analyzed. There is a third set of spots at 128° from the growth direction. This is roughly three degrees from the angle (125.26°) where the {200} lattice spots should lie if the crystal were fcc. However, these spots also correspond to a 0.20 nm spacing and thus do not appear to be from an fcc arrangement. In Figure 3.41B, the HRTEM image shows isolated areas where lattice images are visible. The FFT shows that there is considerable layering in the growth direction with spacings consistent with either Co or Cu {111}. At 150° to the axis there is a set of weak spots that correspond to the Cu (or Co_{fcc}) ($00\bar{2}$) planes. The area at the "gap" near the outer base of the island shows a transition from the Co structure seen in the Co film distant from the islands and the apparently less structured interior of the island. In the Figure 3.41C the lattices of the Co film appear to fade to an amorphous background towards the island center. There are three discernable pairs of spots in the FFT. On the growth direction, there are the 0.20 nm (111) spots and at 125° there is a doublet of weak spots corresponding to lattice spacings 0.19 nm and 0.21 nm. The latter spacing is consistent with the Cu (111) but the 0.19 nm is further enough apart than the {200} that it doesn't seem to be a misidentification of these planes. Near the top of the inside of the island

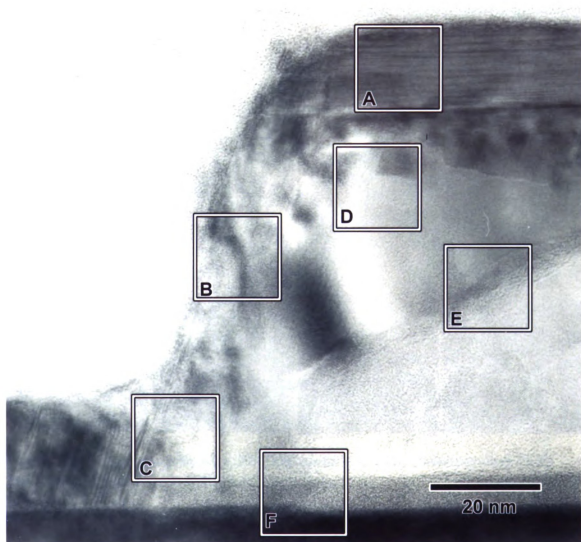


Figure 3.40. HRTEM overview of the "inset 1" area of Figure 3.39C. Six representative areas were selected for lattice image analysis.

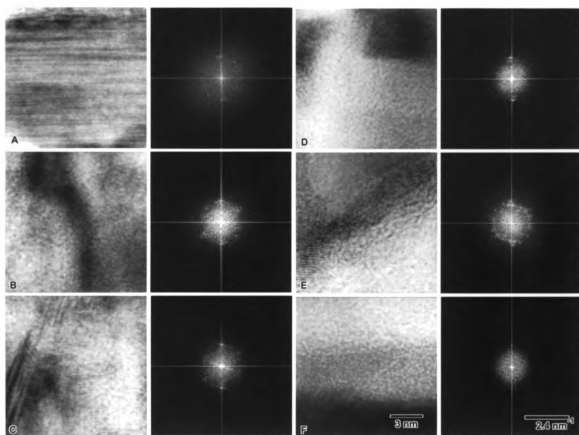


Figure 3.41. High magnification HRTEM areas and their corresponding FFTs from areas A-F in Figure 3.40.

there is an abrupt change in contrast below the Co layer. This is shown in detail in Figure 3.41D. The FFT of this area shows a strong 0.20 nm growth direction spacing with a second coaxial set of spots corresponding to a 0.247 nm lattice. At 125° to the growth direction, there is a set of weak spots at 0.18 nm, the Cu_{fcc} {200} spacing. At the boundary of the light, apparently amorphous area and the darker area below the Co layer topping the island, the boundary displays a band of apparently randomly oriented nano-crystals. There are two rings of spots, one with strong intensity in the growth direction at 0.20 nm and a second with a spacing of 0.25 nm. These latter spots correspond to {110} fcc spacings for Cu or Co. The final area tested on the left side of the island (Figure 3.40F) was the band of transition contrast between the bottom of the island and the Nb base layer. No lattice fringes were evident in the HRTEM image and the transform was accordingly diffuse.

A sample from the mid-section of the island was also analyzed via HRTEM. The section (inset (2) from Figure 3.39C) is presented below. Three areas, on a transect from top of the ML to the Nb surface, were selected for lattice image analysis and are shown in Figure 3.42. The first area (inset A), which is the Co layer at the top of the island, shows the 0.20 nm spacing in the growth direction. A second set of spots at 57° to the growth direction, also at the 0.20 nm spacing is also visible. This second set is within about 2° of being consistent with the Co_{fcc} structure and 3° from the hcp {0111} position. The (00 $\bar{2}$) spots are not seen. However, their spacing is right at the resolution limit. Two crystals separated by a thin structureless band appear further towards the Nb base layer (inset B) of

Figure 3.42. The bottom part of the inset displays lattice fringes in the growth direction and the FFT shows a pair of spots perpendicular to the growth direction at a spacing corresponding to a 0.25 lattice spacing, close to the {110} spacing in Cu or Co_{fcc}. The third area analyzed, just above the continuation of the structureless band described in Fig 3.41F, again showed what appears as multiple crystal forms. In this case they may be either interlocking or overlapping. The FFT of the high magnification inset C of Figure 3.42 shows the expected 0.20 growth direction spacing. It also shows a pair of spots at 62° from the growth direction corresponding to a lattice spacing of 0.23 nm, the Nb {110} spacing. At 66° there is a third, stronger set of spots that corresponds to the 0.20 growth direction spacing. Finally, at 97° there is a set of spots arising from a lattice spacing of 0.25 nm, close to the fcc {110} spacing for this system. On the right-hand side of the island, the junction between the island and the Co layer deposited directly on the Nb appeared different from the overall morphology seen on the left-hand side. Figure 3.43 shows a HRTEM overview of this region. On this side, rather than being continuous with the Co layer on the top of the island, the Co layer appears to continue under the edge of the island. There appears to be a gap at the edge that was continuous of the left side (*cf.* Figure 3.40). Six areas were selected for HRTEM lattice analysis, as was done with the previously examined edge. In the Figure 3.44A, an area in the Co layer atop of the island is shown. The shows strong contrast perpendicular the growth direction with the expected 0.20 nm lattice spacing.

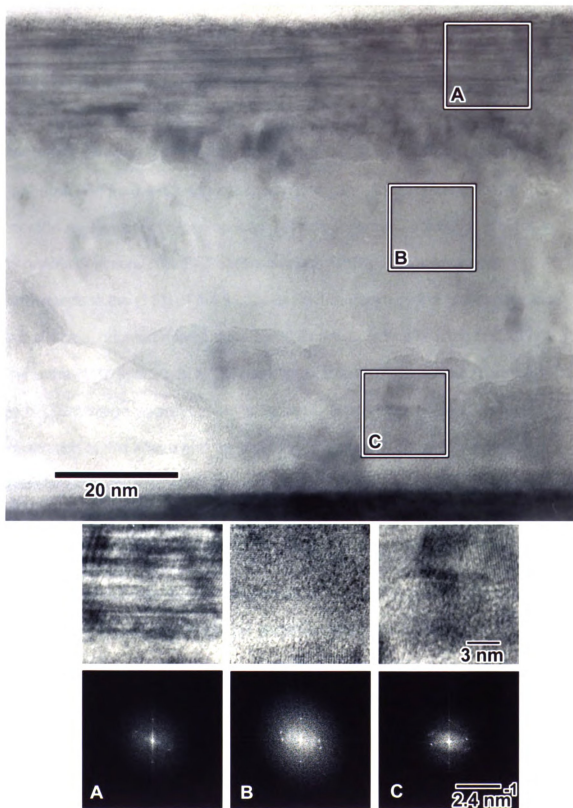


Figure 3.42. HRTEM overview of the "inset 2" area of Figure 3.39C. The three inset areas and their FFTs are also shown.

This motif is continued in Figure 3.44B where the strong growth direction layering prevails. However, significant regions exist in these areas that show a second lattice. These are especially obvious in the upper right-hand corner (towards the outside of the island). The orientation (125° from the growth direction) and the spacing as shown in the FFT are consistent with the Cu ($00\bar{2}$) lattice. In the "gap" area (Figure 3.44C), the enlarged micrograph appears to be nearly amorphous. However, superimposed on this background are lattice images in the growth direction. The FFT shows two spots. The higher frequency corresponds to the $\{111\}$ of the fcc Cu or Co. Interestingly the inner spots arise from a lattice, oriented nearly in the same direction, with a spacing of 0.23 nm. This is the $\{110\}$ spacing in Nb. Towards the interior of the island (Figure 3.44D) the HRTEM image again appears to be nearly amorphous. However, careful observation of this image and the resulting FFT show a set of lattice planes consistent with Cu in the (111) growth orientation. The HRTEM image from near the Nb boundary (Figure 3.44E) shows a number of small lattice areas in at least three orientations. Reference to the FFT from this area shows growth direction lattices consistent with Nb and Cu growing on their (110) and (111) planes respectively. The second major set of lattices shows spots oriented 125° to the growth direction. The inner set corresponds to the 0.20 nm $\{111\}$ spacing while the outer (0.18 nm) matches the $\{200\}$ Cu spacing. Careful inspection of the FFT shows two sets of weaker spots. The first is seen at 40° to the growth axis and arises from a spacing of 0.33 nm this is reasonably close to

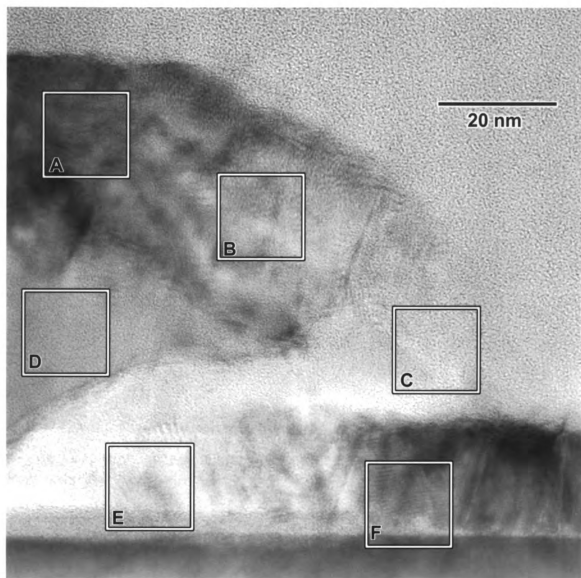


Figure 3.43. HRTEM overview of the "inset 3" area of Figure 3.39C. Six representative areas were selected for lattice image analysis.

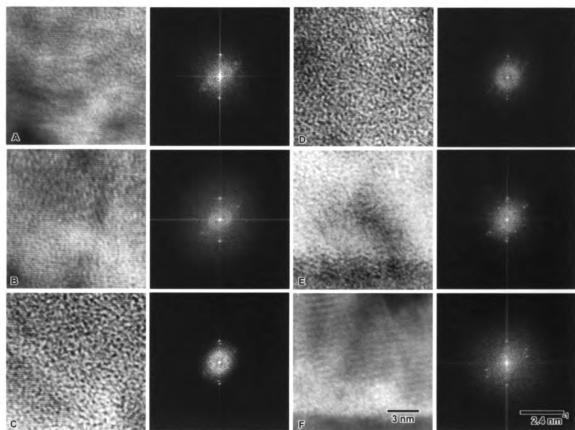


Figure 3.44. High magnification HRTEM areas and their corresponding FFTs from areas A-F in Figure 3.43.

Nb bcc lattice constant, 0.331 nm. The second weak set occurs at 70° from the growth axis and the 0.26 nm spacing they represent is a good fit to the 0.255 nm Cu {110}. The final area analyzed was at the edge of the Nb layer, where it appears to have grown over the quasi-amorphous layer that spans the island at the Nb interface. The HRTEM image shows some moiré fringes implying overlapping lattices. In this case, they appear to be rotational in nature. The typical (111) growth direction planes are seen as is a second set of similarly spaced lattices at 102° from the growth direction. At 125° a third set of spots can be seen in the FFT. These correspond to lattices with a 0.18 nm spacing, close to the Cu {200} planes.

HREDS of sample 19-4

To determine if the local elemental composition and distribution matched that implied by the morphologies, spot mode HREDS was employed using the same operation protocols as before. Figure 3.45 shows an EDS spectrum of the top (striated) Co layer on the top of an island in sample 20-4. It shows a nearly pure Co composition. Similarly, the central parts of the island in both the "denser" and "lighter" areas were nearly pure Cu. (Figure 3.46). Figure 3.47 is a representative spectrum from the nearly transparent region seen near the gaps at the lateral margin of the islands. Again it shows a nearly pure Cu composition, but very little mass. The amorphous area seen at the interface of the island Cu layer and the Nb base layer (e.g. 3.40F) is composed of a low density Cu-Nb mix as the spectrum in Figure 3.48 shows.

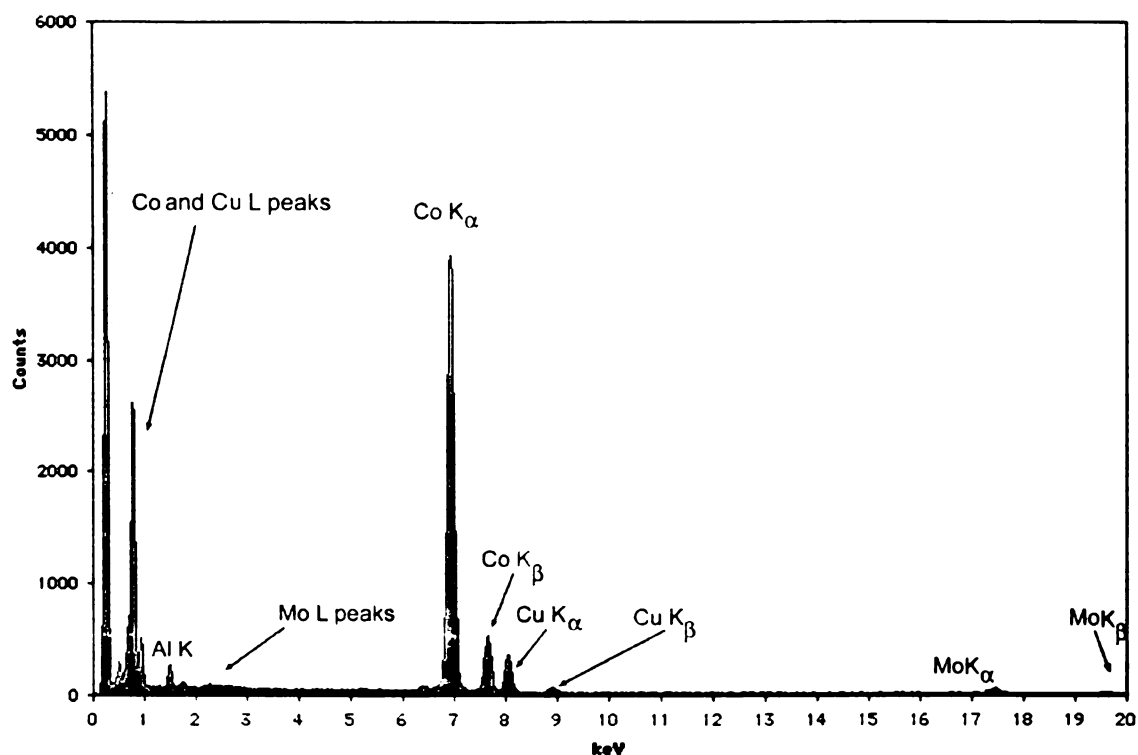


Figure 3.45. HREDS spectrum from the Co layer on an island from sample 19-4.

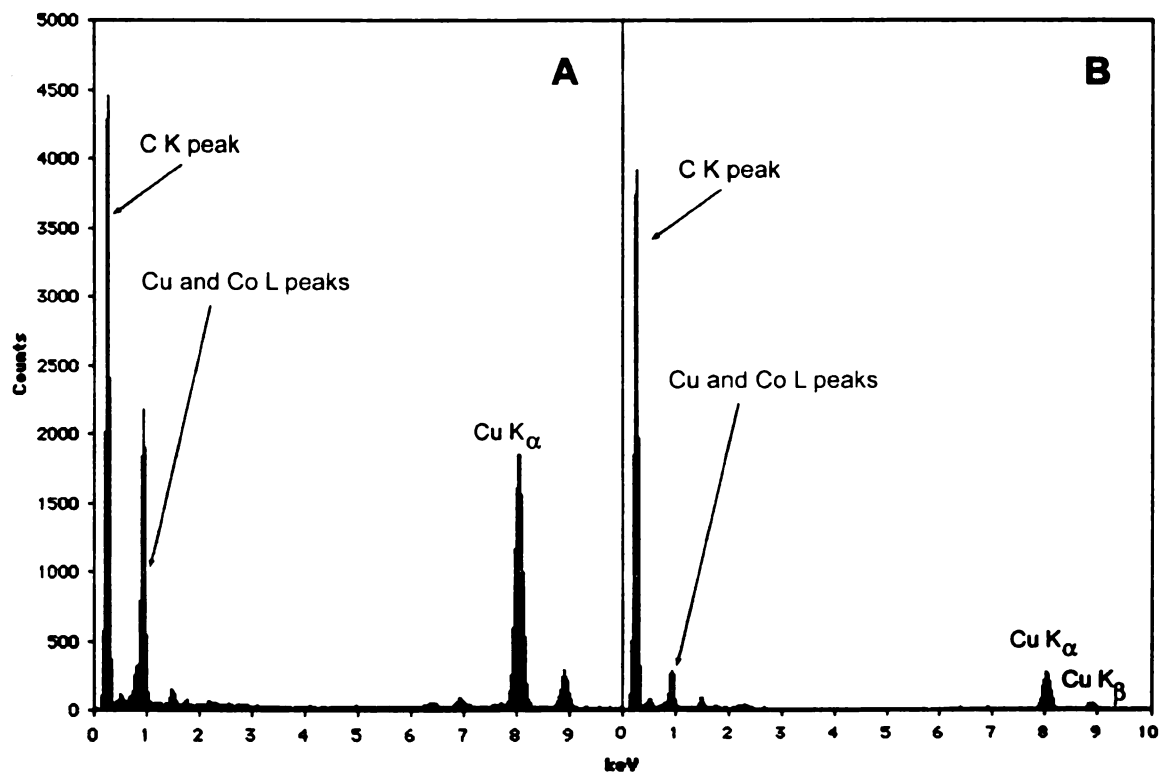


Figure 3.46. An HREDS spectrum from the thicker (A) and thin (B) middle areas of the Cu layer on a island from sample 19-4.

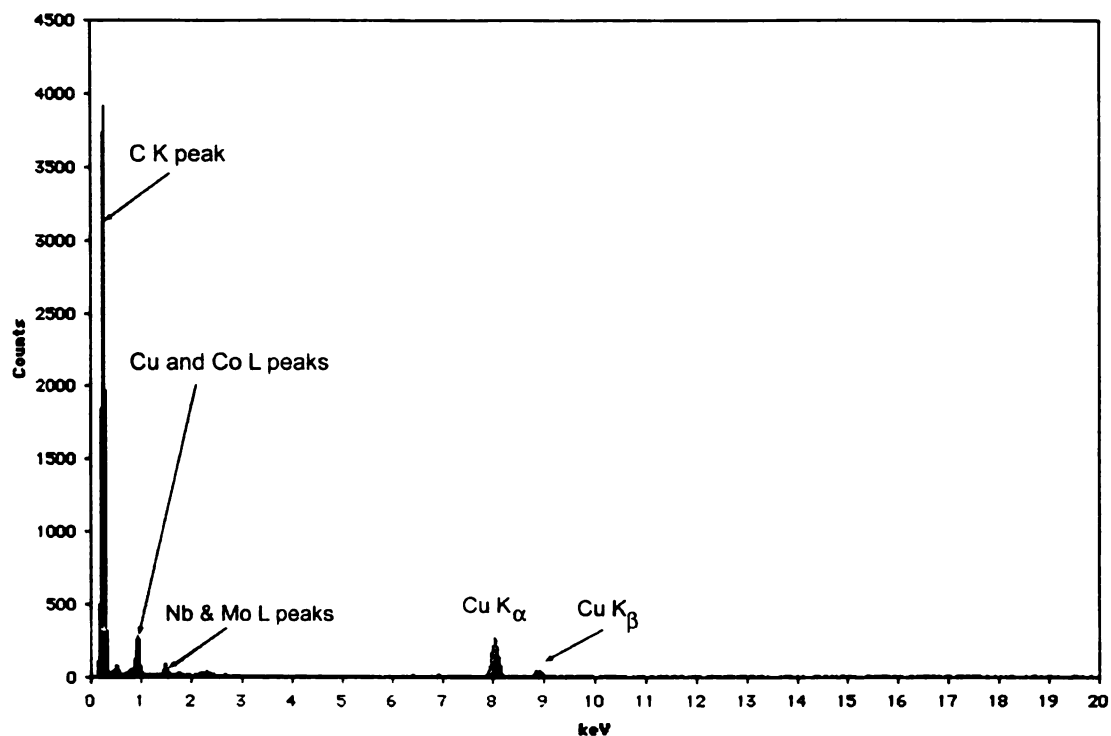


Figure 3.47. An HREDS spectrum from the "gap" area in an island from sample 19-4.

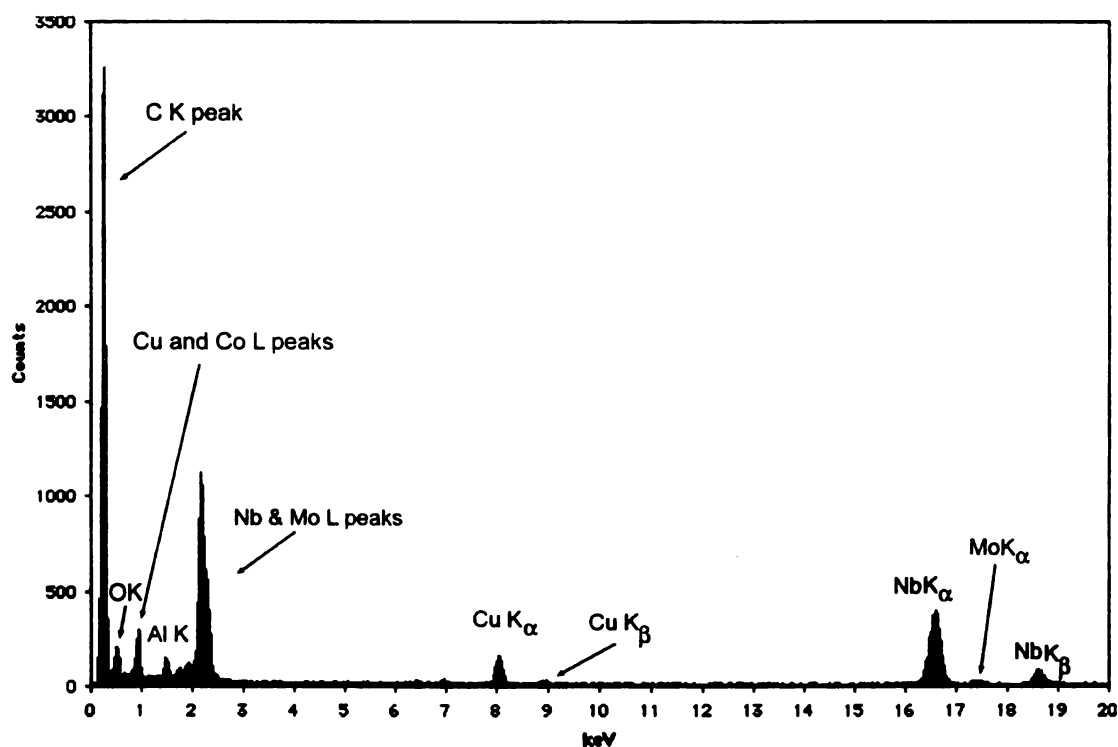


Figure 3.48. An HREDS spectrum from the Cu||Nb interface at the base of an island from sample 19-4.

Summary for samples 19-3 and 19-4

Samples 19-3 and 19-4 were designed to be simple 20 nm bilayers of Cu with Co on top. Uniform structure like this was nowhere evident in either sample. The island morphology seen in these samples was similar to that seen in the epitaxial samples. The holes seen in the epitaxial samples were not seen. However, the copper content of the electron lucent island margins was considerably reduced. In contrast with the epitaxial MLs, there was a continuous amorphous layer that subtended the entire island. This type of formation was only seen at the upper and lower margins of holes in the ML samples. The Co layer on top of the islands appeared to have the same striated contrast mechanisms seen in other Co layers in contact with Cu. However, this was not seen in the Co layer that grew on the Nb directly, implying that it assumed its hcp structure.

CHAPTER 4. DISCUSSION

4.1 TEM of Multilayer Cross-sections

One of the first questions to be considered, in any TEM study, is the fidelity of the data with respect to the actual specimen. Regardless of the material being studied, the recognition of artifacts in TEM images is always a problem. TEM image artifacts can be broadly grouped into those arising from specimen preparation and those arising from TEM operation. In the first group, artifacts can be generated in the initial sample-isolation process, by oxidation or contamination. As the routine sample preparation continues, large free surfaces are generated and elevated temperatures may be required to cure bonding agents. These factors may induce chemical or diffusional changes that alter the structure and thus the TEM image. Thinning the sample requires mechanical abrasion that can cause deformation artifacts and ion milling that can cause changes in the projected structure due to heating, surface amorphization, and changes in the surface topography by differential milling,

Imaging in the TEM is a second major area for artifacts to accumulate. Careful attention to beam geometry, focus and sample tilt are all crucial to the acquisition of unambiguous images.

One method of containing the artifacts is to carry through controls with the experimental treatments. The comparison of features on the controls with the experimental treatment should allow extraction of the artifactual effects (barring a treatment X artifact interaction). Thus, the inclusion of data from polycrystalline sample 20-2, which showed structures consistent with previous work done using

TEM on GMR MLs, provides a degree of assurance in assigning causality to results of the various fabrication treatments.

The Co/Cu multilayer system investigated in this study is an important and relatively mature example of a GMR system. Therefore, it was a good starting point in developing production protocols for creating epitaxial structures for CPP GMR investigations. Very similar epitaxial multilayer systems, grown by MBE, on $(1\ 1\ \bar{2}0)$ sapphire have been previously been reported [e.g 75]. Thus, a main consideration in this investigation was to determine the factors effecting the quality of the final ML product and transferring the approach to a specific magnetron sputtering system. However, no parametric separation of the causes of variability in many of the fabrication steps is strictly possible due to lack of replications. On the other hand, the qualitatively uniform epitaxial growth of Nb films, the one replicated process step, suggests that the run-to-run variability is relatively low in this system.

4.2 Growth of the Nb Base layer

Nb contact layers are required for low temperature (4.2K) CPP GMR experiments. This is due to the high super-conducting temperature of Nb (9.5K) and its ability to remain super conducting well above the 4.2K experimental environment temperature even in a strong applied magnetic field. Therefore, for an epitaxial GMR device to be prepared for a system using Nb superconducting contacts, the Nb contact (base) layer must also be epitaxial.

Epitaxial Nb films

Nb epitaxial films grown in this investigation varied from the nominal layer thickness of 250 nm by more than 20%. However, there were no observed qualitative differences in the epitaxial Nb layers among the samples, within the field of view restrictions of the TEM technique. A length of roughly 25 μm (along the multilayers) near the perforation of ion milled samples, is of "usable" thickness for TEM. Within this range the Nb base layers appeared to be single crystals for all epitaxial samples. This is in comparison to the often less than 50 nm Nb grain size seen in cross sectional view of the polycrystalline Nb capping layer formed atop the epitaxial ML samples (e.g. Figure 3.23). The Nb||sapphire interfaces (data not shown) in the epitaxial samples show extended regions that are either coherent or semi-coherent (strain relaxed by dislocations). No amorphous layer [48] was seen along any Nb||sapphire interface, supporting the proposition that annealing prior to Nb deposition recreates the sapphire surface.

In the epitaxial samples, the upper surface of the Nb base layer was also smooth. Previous work [44, 57, 76] has shown that the upper surface of epitaxial Nb layers, prepared as those studied here, remains smooth to a RMS roughness of 0.35 nm or better. Similar results were recorded in this investigation. However in this investigation, the Nb layer was always subsequently coated with Cu. In some areas the exact upper boundary of the Nb layer was indistinct (e.g. Figures 3.8, 3.40). This could have been due to either intermixing (chemical interdiffusion) or intercalation (due to local physical roughness) between the Nb and the subsequently deposited layer. Separation of the two contributions by HRTEM, if both are present, is not always straightforward [75]. If the concentration gradient is constant along the interface and the roughness is isotropic, the two contributions should be separable using a Fresnel focus series,

[50,51,77]. It is important to note that the majority of these interfacial areas are ordered to within a few atomic radii. The two crystals on either side have characteristically distinct contrasts and there is no appreciable region between the two showing complete loss of resolvable order.

Polycrystalline Nb films

In an SAED pattern of a circular field covering just the metal layers of the polycrystalline sample 20-2 (≈ 450 nm) arcs are seen in the vertical orientation of the Nb {110} frequency ring. These indicate an $\approx 20^\circ$ spread around the growth direction, implying that some low angle grain boundaries exist (Figure 3.12, inset). The exact location of these grain boundaries (whether they are in the top or bottom Nb layer) cannot be determined from the SAED pattern. However, along the Nb||sapphire interface in this sample, coherent or semi-coherent regions, at least 50 nm long, were also seen (data not shown) and neither the base or capping layer crystals are randomly oriented. Thus, even with room temperature deposition, Nb films grown on annealed sapphire surfaces are highly textured in the [111] growth direction.

In the case of room temperature Nb layer deposition (sample 20-2), CTEM (Figure 3.12) has shown that Nb upper surface is also nearly flat. The HRTEM image (Figure 3.14), interpreted with the interfacial roughness caveat mentioned above, also shows little surface roughness at the boundary with the Cu seed layer. This is in contrast to the surface roughness that was seen by AFM with a uncoated epitaxial Nb upper surface [44,57]. In these studies Nb deposited at room temperature on preannealed sapphire surfaces showed a 3.2 nm RMS roughness.

The epitaxial Nb lattice forms a facile but slightly strained continuation of the Al lattice sites in the $(1\ 1\ \bar{2}\ 0)$ of the sapphire. This leads to a system of

dislocations that accommodate this strain [46]. The samples prepared in this study should be able to provide a comparison between the textured polycrystalline strain accommodation and that seen due to mismatch dislocations in the epitaxial system. The differences in the surfaces resulting from the dislocations may affect the behavior of Cu on them.

4.3 Cu buffer layers

A 20 nm thick buffer layer of Cu was deposited on the Nb base layer in all of the ML systems tested. A Cu buffer or seed layer is prescribed to accomplish two tasks. First, the buffer layer should provide a diffusion barrier between the Nb contact layer and the ML. The Co (or other ferromagnetic layer) used in the GMR device might react with the Nb layer if it were deposited directly on the Nb contacts. In the case of Co and Nb, the binary phase diagram indicates that some solubility exists and a variety of intermetallic compounds may be formed. Their phase stability appears to continue to low temperatures (Figure 4.1A). In the case of Cu and Nb the situation is clearer (Figure 4.1B) with no low temperature solubility. Thus, Cu should be a good choice as a diffusion barrier for the subsequently deposited Co/Cu GMR device.

Epitaxial Cu buffer layer

Some regions of the Cu||Nb interface from epitaxial samples had an amorphous layer indicative of an interdiffusion zone. In the sample 20-1 buffer layer, there was an approximately 5 nm wide structure-less zone along the Nb||Cu interface, in addition to some anomalous ordered inclusions. This type of amorphous zone was also seen under the Cu islands in samples 19-3 and 4 and under the buffer layer holes in ML samples 20-3 and 2-4. A similar zone was shown, but not evaluated, previously for the epitaxial Cu||Nb interface [74]. Occasionally, amorphous interfacial regions have been reported for multilayers of

materials that should not interdiffuse. For example, in a Cu/Ta multilayer system, Lee, *et. al.* [76] found that at 500°C (substantially below the Cu or Ta melting points) there were 2 nm amorphous regions at interfaces between layers of these metals. In co-evaporated films in the Co/Cu system, the two materials generally tend to segregate on heating [77]. Paradoxically, while the direct deposition of

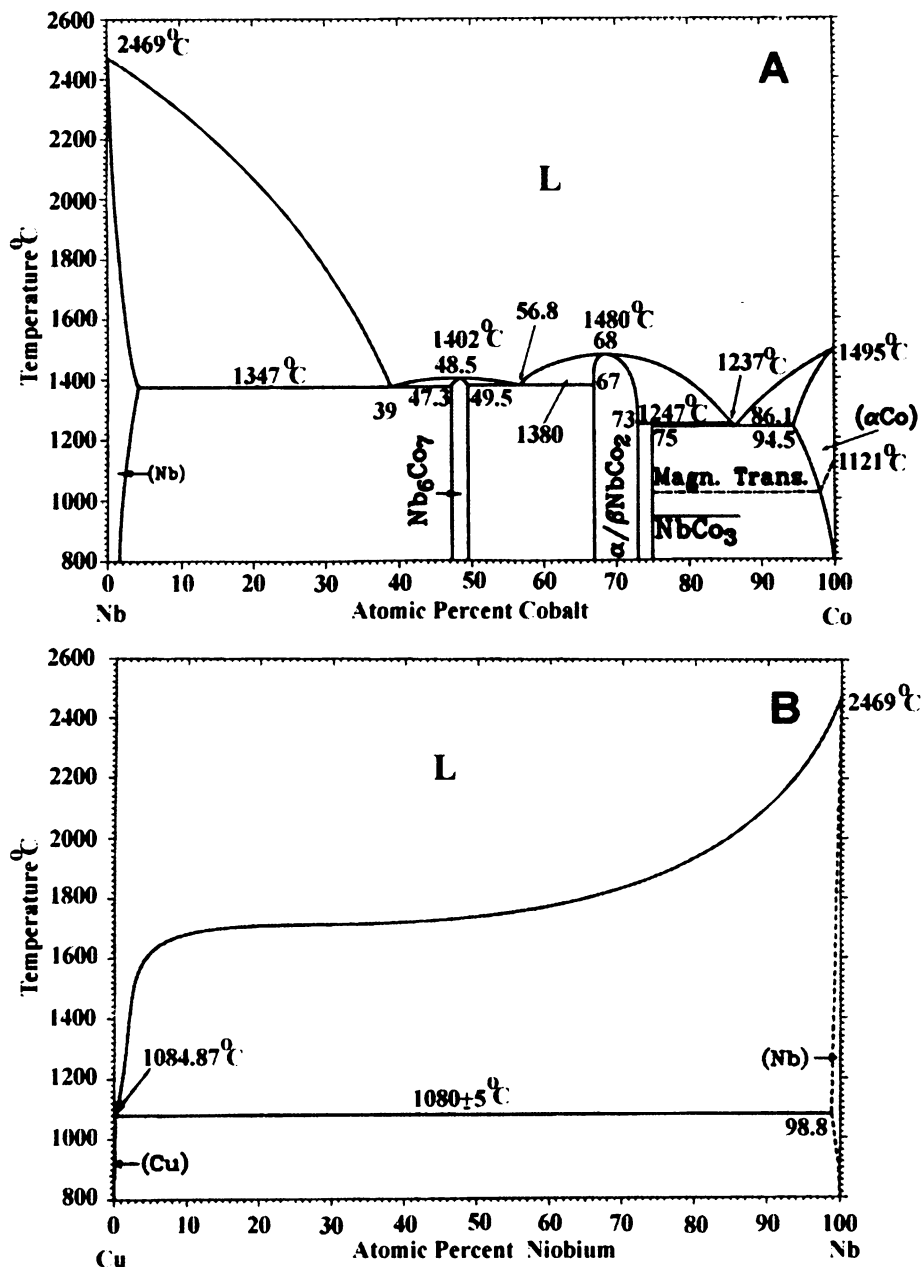


Figure 4.1. Binary phase diagrams. A) Co-Nb. B) Cu-Nb. Below 800°C there should be no solubility of Nb in Cu

the first Co FM layer on to a Nb contact layer could lead to some degree of interdiffusion, this was not supported by the Co||Nb interfaces between the islands in the bilayer systems in this study (Figure 3.39 and 3.40). Although the Co was sputtered on the Nb at roughly 30% of T_m for Co the interface between Co and Nb shows no observable signs of interdiffusion. The diffuse Nb||Cu regions were seen only in some areas of the epitaxial GMR samples and never in the polycrystalline samples. Thus, the creation of the diffuse region at the Nb||Cu interface by physical mixing, due to the sputtering process, also seems unlikely as the same deposition system was used in all cases.

A second reason for using a Cu seed layer is to form a crystallographic motif, in the growth direction, to facilitate the epitaxial growth of the GMR device. It is supposed to translate the {110} bcc closest packed planes of the epitaxial Nb base (contact) layer to the close packed fcc planes of the active ML or spin valve constituents. The Cu seed layers in this study were deposited under 4 different temperatures in the epitaxial samples (Table 2.1). These deposition temperatures resulted in at least 3 different buffer layer morphologies.

In the case of sample 20-1, the Cu buffer layer was deposited at 150°C and subjected to a 10 minute anneal at 350°C. This resulted in the most uniform gross morphology of the epitaxial systems. However, areas in the buffer layer itself exhibited lattice spacings that corresponded to Nb {110} well away from the Nb base layer interface, and other lattice spacings, inconsistent with any known equilibrium structures of the constituent elemental species, were also observed. These anomalous structures may or may not have affected the growth and performance of a GMR device but, there is reason to doubt that the deposition protocol used is the best approach to buffer layer deposition. EDS showed that

the multilayer had no unaccounted for constituents. However, the possibility of $\text{Co}_x\text{Nb}_{1-x}$ phases cannot be ruled out.

The remaining epitaxially grown samples (20-3, 20-4, 19-3 and 19-4) all showed gross disturbances in Cu seed layer confluence (Figures 3.23, 3.30 and 3.39). In these cases, the Cu seed layers had aggregated into what appeared (in cross section) to be islands with their margins acutely tapered in the growth direction. In these islands, the Cu buffer layer varied from 2 to 4 times the nominal thickness. Given the apparent partial covering of the Nb layer by these islands (e.g. Figure 3.23 and 3.39), the increased height of the Cu buffer layer under these islands may well account for the mass of Cu deposited. The form and distribution of these islands is entirely consistent with the plan view AFM images of similarly prepared 20 nm Cu layers grown on epitaxial Nb base layers (Figure 4.2) [47].

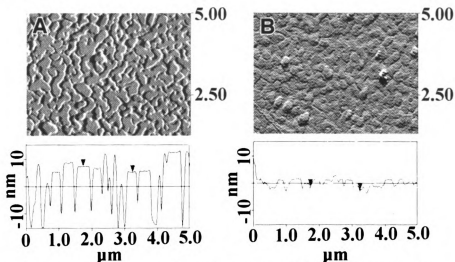


Figure 4.2 Atomic force microscope images of 20 nm Cu layers grown on the surface of 250 nm epitaxial Nb layers. A) Deposited at 350°C. B) Deposited at 150°C and annealed at 350°C for 10 min. From [47].

In that investigation, a 20 nm Cu film grown on a Nb substrate showed what appears to be island (Volmer-Weber) growth and that that growth form persists through 100 nm film thickness at a 350°C. Volmer-Weber growth followed by

cluster migration could account for the widely spaced Cu islands seen in sample 19-4 [34]. In the samples with epitaxially grown Cu-buffer layers, there are no grain boundaries evident (Figures 3.8, 3.25, 3.32, 3.42). This observation differs from some epitaxial Cu buffer layers previously fabricated with this sputtering system [57,74] where twins were found close to the Nb interface. Samples 19-3 and 19-4, were fabricated in the same process run as the sample 19-1 used in the EBSD analysis of the Nb/Cu/Co system [47]. In that investigation, twins were seen but could not be quantitated, due to the thinness of the film and dominance of diffraction from the Nb underlayer. A similar 20 nm Cu||Nb system fabricated in an MBE system yielded X-ray texture scans that also showed twinning [19].

Polycrystalline Cu buffer layer

In contrast to the Cu buffer layers seen in the epitaxial samples, the sample prepared at room temperature (20-2) showed normal layer growth. This included a strong $\langle 111 \rangle$ texture and sharp, ordered interfaces between the Nb base layer and Cu buffer layer grain sizes consistent with those seen in previous investigations [54] (Figures 3.20 and 3.21). Low angle ($<10^\circ$) grain boundaries were seen in the Cu and Nb layers (Figures 3.12, 3.13), but all grain boundaries were not continuous through the Cu||Nb interface (e.g. Figure 3.20). Although only a limited number of crystals were analyzed in the Cu seed layer, no bcc structured Cu was found either in the buffer layer or elsewhere in the ML. However, considering the intermittent occurrence of columnar bcc non-equilibrium grains previously reported for Cu [51,54], (and other normally fcc metals) [54] this finding should be accepted with grave caution.

4.4 Co/Cu multilayers:

Growth of the epitaxial Co/Cu multilayer

The sample 20-1 epitaxial multilayer shows a pronounced overall layer contrast modulation (Figure 3.2A). Even in this image, taken at near Gaussian focus, the layering is obvious. The most immediate cause of this abnormal and inverted contrast modulation is the deficiency of Cu in the nominally Cu layers (Figure 3. 11). While no specific mechanism has yet been derived to account for this, it is interesting to compare this effect with that seen in the islands formed in the bilayer samples, 19-3 and 19-4. In these samples, islands of nearly pure Cu develop that have lower contrast margins and considerable amorphous character. It seems unlikely that the Cu should have diffused into the Co layers, although some Cu was found in all of the Co layers in sample 20-1. Firstly, Cu is insoluble in Co well above any of the temperatures used in the fabrication of this multilayer. Secondly, in the case of sample 20-4, the first Co layer was deposited at a roughly 370°C higher temperature than that used in the Co deposition in sample 20-1. Even in this temperature regimen, the (greatly dilated) Cu buffer layer interface with the first Co layer shows no sign of amorphous material in sample 20-4. Thirdly, the EDS spectrum for the whole multilayer stack in 20-1 shows a far lower Cu/Co ratio than the simulation of the multilayer, the sample 20-4 epitaxial sample or the 20-2 polycrystalline sample (Figures 3.10, 3.11, 3.22, and 3.35). The lower contrast areas in the 20-1 sample, for example those seen near the Co5||Cu4 interface, show a widely spaced lattice structure of undetermined origin, in addition to spacings consistent

with the expected $\{111\}$ of Cu. However, the distinct possibility exists that the fringes arise from the adjacent Co layer. The tortuous interface between these Co and Cu layers (Figure 3.6) supports this. The existence of a high degree of local Co crystal incursions into the Cu layers could give the impression of a much higher Co content than actually present. A possible structure that is consistent with the data gathered so far would be some form of amorphous (glass-like) copper compound (cupric carbonate, for example, can be amorphous [78]). However, any proposed explanation must account for both the low overall Cu concentration and the nearly nominal ML dimensions.

In samples 20-3 and 20-4 the multilayers grown on the top of Cu buffer islands showed little overall inter-layer contrast (*e.g.* Figure 3.2C). However, especially in last deposited layers (nearest the Nb capping layer), layers can be delineated. As can be seen in HRTEM (*e.g.* Figures 3.32-3.34) this differentiation is largely due to abrupt changes in crystal orientation between layers. In the copper layers, there appears to be a tendency for the orientation along the $[111]$ growth axis to switch stacking between sequential Cu layers. Additionally, the Co layers tend to become increasingly hcp towards the center of the layers. In thin Co layers on $\{111\}$ Cu, the transition from fcc to hcp has been shown to be essentially complete within 5 atomic layers (1.03 nm) [79]. This was also seen in epitaxial MBE Co/Cu (111) superlattices grown on Nb base layers on sapphire ($1\ 1\ \bar{2}0$) substrates for Co thicknesses of 1.6 to 2.0 nm separated by 2.6 and 2.0 nm Cu layers [73]. Much of the interlayer delineation that is seen appears to be due to the combined effect of these intra-layer stacking changes.

Growth of the polycrystalline Co/Cu multilayer

The multilayer stack, $(\text{Co}_{6\text{ nm}}/\text{Cu}_{6\text{ nm}}) \times 5$, grown on top of the polycrystalline Cu buffer / Nb layer (sample 20-2) showed no overall contrast difference between individual Co and Cu layers (Figure 3.2B). This is as expected since in the HRTEM (multibeam) objective lens configuration, the differential contrast is due to high angle (Z dependent) scatter of the beam electrons. Cu and Co, differing in Z by two, should be nearly indistinguishable in a focused image. The layering becomes more evident with objective lens defocus, which creates contrast fringes related to the mean inner potential at the interface of the materials in the sample [80]. More obviously, the upper layers in sample 20-2 can be distinguished in some areas in high resolution imaging mode due to layer specific crystal defects (Figure 3.14). In the room temperature sample, grains in the Cu layers were consistently observed to be growing on the (111) planes with extensive areas oriented to allow structural images (Figure 3.14). In the Co layers, extensive in plane twinning was seen in many areas of the field of view. This appears to have led to moiré patterns in some areas of the Co layers, as described for Co-Pt multilayers [81], while in adjacent areas, the film appears to be strictly fcc across an entire Co layer (Figure 3.16). While extensive Co_{fcc} regions have been characterized in sputtered films by EBSP [57], the results seen here, in both the epitaxial and polycrystalline ML samples, demonstrate that the stable range of Co_{fcc} can be much less. Interestingly, in the polycrystalline sample (20-2), the grain column adjacent to the region with the pronounced

stacking fluctuations appears as a continuous fcc crystal through an equivalent vertical range.

In the two bilayer samples, the 20 nm Co layer topping the islands showed strong striations qualitatively similar to those seen in sample 20-2. However, there also appear to be some crystals oriented with their close packed planes off axis (Figures 3.40 and 3.41). Away from the islands, the Co layer showed an apparent mix of hcp and fcc orientations (data not shown).

Summary:

The growth of epitaxial Co/Cu multilayers on Cu buffer layers via sputter deposition appears to be tenable. The uniform persistence of fcc Co in epitaxial layers as thick as 6 nm appears less likely, due to conversion to mixed or the hcp form a few nanometers from a Cu boundary. As suggested by the phase diagrams, Co/Cu interdiffusion appears to be insignificant within the temperature regimens used in this investigation. However, others have reported or suggested that interdiffusion may occur. This needs to be carefully separated from diffusion *through* a film that can also occur [e.g. 25, 82]. Cu/Nb diffusion appears to be more likely, based on the presence of amorphous interfacial layers seen in some instances in epitaxial buffer layers. Amorphous layers, of similar appearance, have been described in Cu/Ta systems [76] despite similar indicated insolubilities. However, the single overriding impediment to success in growing epitaxial Co/Cu GMR multilayers, or any GMR device, on epitaxial Nb layers in the deposition system used herein, seems to be the initial formation of reliable flat single crystal Cu-buffer layers. Either a reassessment of the thermal treatments used and/or, perhaps, the choice of Cu, alone, as the buffer layer element are worth consideration.

CHAPTER 5. CONCLUSIONS AND RECOMENDATIONS

Conclusions:

1. The combination of high deposition temperature and post deposition annealing of the Nb base layer produces uniform, epitaxial, single crystals with a high defect density which appears qualitatively different than the room temperature preparation.
2. The Cu buffer layers of all of the epitaxial samples showed gross deviations from the nominal structure and distribution on the epitaxial Nb base layer. The deviation from the ideotypic deposition took two forms, which may depend on the use of a post deposition anneal for the Cu buffer layer. Lower temperature deposition, with post deposition annealing has lead to laterally continuous buffer layers that appear to have a diffuse interface with the Nb base layer. The deposition of the Cu buffer at higher temperatures, or the deposition of layers subsequent to the Cu layer at high temperatures, may lead to the formation or persistence of buffer layer island growth. No buffer layer material is generally seen between islands. In some islands, voids may appear in the Cu buffer layer that are adjacent to less electron dense less ordered Cu areas.
3. When grown on islands where a uniform epitaxial Cu buffer layer existed, the ML growth appeared epitaxial. The elemental composition appeared consistent with the nominal components and component ratio.

4. The first epitaxial sample (20-1) ML structure shows an unaccountable lower than nominal mass of Cu, despite having layer dimensions consistent with those of the nominal motif. This is corroborated by the lower than expected contrast and lack of order in the nominally Cu layers.
6. The polycrystalline sample (20-2) was entirely crystallographically consistent with other groups samples of this type. The EDS elemental composition was also the same as the model for the ML.

Recommendations:

1. The island growth seen in the 20 nm sputtered Cu buffer layers in the samples in this study, and other samples produced in the sputtering system, needs to be eliminated to form extended epitaxial layers. Currently the individual effects of many system variables cannot be separated and the cause of island growth is unknown. To separate out the deposition temperature X Nb epitaxial layer interaction effect, various thickness of Cu should be deposited on epitaxial Nb at room temperature. Ideally one sample in this test should also have the same nominal layer dimensions used herein with all of the layers prepared at room temperature (much like sample 20-2), *but grown on an epitaxial Nb substrate*. This would help elucidate the main effect of the epitaxial Nb surface on subsequent layer growth.

Prior to TEM sample preparation, these samples should be characterized via X-ray diffraction (Mo tube). Low and high angle X-ray diffraction data, analyzed with the appropriate software [cf. 31] can characterize inter and intra layer crystallinity. This would provide an expeditious method of determining

when further (detailed) TEM studies are warranted and provide a corroborative method for the TEM analyses. Fractions of these samples should be subjected to a series of inert environment annealings at least up the temperature at which the sample 20-4 encountered. This would be followed by further X-ray and AEM evaluation to determine crystalline structure and chemical changes.

The possibility exists to expand these treatments to include a limited number of additional layer thicknesses .

2. For more complicated device designs, it would be useful to routinely deposit the total layer series used in the differentially masked device, on an adjacent area of the substrate coupon, for later TEM and XRD analysis if required.

LIST OF REFERENCES

- [1] A. Barthélémy, A. Fert, F. Petroff (1999) Giant magnetoresistance in magnetic multilayers *In*: K.H.J. Buschow, ed. Handbook of Magnetic Materials V 12 p1-95 Elsevier Science B.V.
- [2] N.M. Baibich, J.M. Broto, A. Fert, F. Nguyen Van Dau, F. Petroff, P. Eitenne, G. Creuzet, A. Friederich, and J. Chazelas. (1988) Giant Magnetoresistance of (001)Fe/(001)Cr Magnetic superlattices, Phys. Rev. Lett. 61, 2472-2475.
- [3] G. Binasch, P. Grunberg, F. Saurenbach, and W. Zinn, (1989) Enhanced Magnetoresistance in Layered Magnetic Structures with Antiferromagnetic Interlayer Exchange, Phys. Rev. B 39, 4828-4830.
- [4] S.S.P.Parkin, N. More, and K.P. Roche, (1990), Oscillations in exchange coupling and magnetoresistance in metallic superlattice structures: Co/Ru, Co/Cr, and Fe/Cr, Phys. Rev. Lett. 64, 2304.
- [5] R. Allenspach and W. Weber (1998), Oscillatory magnetic properties, IBM Journal of Research and Development, 42 (1) ONLINE
- [6] S.S. Parkin, R. F. Marks, R.F.C. Farrow, G.R. Harp, Q.H. Lam, and R.J Savot (1992) Giant magnetoresistance and enhanced antiferromagnetic coupling in highly oriented Co/Cu (111) superlattices, Phys. Rev. B. 46(14) 9262-9265.
- [7] M. Suzuki, T. Ohwaki and Y Taga (1997) Durable giant magnetoresistive sensors using Co/Cu superlattices, Thin Solid Films 304 (1-2) 333-338.
- [8] J.M. Daughton, A.V. Pohm, R.T. Fayfield and C.H. Smith (1999) Applications of spin dependent transport materials, J. Phys. D-Appl. Phys. 32(22); 169-177.
- [9] D.B. Jardine, N.D. Mathur, M.G. Blamire and J.E. Evetts (1998) Increased field sensitivity in Co/Cu multilayers with soft adjacent layers, IEEE Transactions on Magnetics

- [10] S.S.P.Parkin, (1991) Systematic variation of the strength and Oscillation period of indirect magnetic exchange coupling through the 3d, 4d, and 5d transition metals, *Phys. Rev. Lett.* 67, 3598-3601.
- [11] S.S.P.Parkin, R. Bhadra and K.P. Roche (1991) Oscillatory Magnetic Exchange Coupling through Thin Copper Layers, *Phys. Rev. Lett.* 66, 2152-2155
- [12] D. Bisero, G. Bordin, M. Minelli, F. Ronconi, F. Spizzo, A. Baraldi, S. Lizzit, G. Paolucci, L. Pareti and G. Turilli, (1999) Effects of Atomic Diffusion Processes in Co-Cu Multilayer Granular Films, *NanoStructured Materials* 11(6): 769-774.
- [13] J. Unguris, D. Tulchinsky, M.H. Kelly, J.A. Borchers, J.A. Dura, C.F. Majkrzak, S.Y. Hsu, R. Loloee, W.P. Pratt, Jr. and J. Bass (2000) Magnetic depth profiling Co/Cu multilayers to investigate magnetoresistance. *J. Appl. Phys.*, 87(9): 6639-6643.
- [14] T.S. Plaskett and T.R. McGuire (1993) Magnetoresistance in $(\text{Co}_{10\text{\AA}}/\text{Cu}_{10\text{\AA}})_n$ multilayer films as n increases, *J. Appl. Physics*, 73(1) 6378-6380.
- [15] A. Cebollada, J.L. Martinez, J.M Gallego, J.J. de Miguel, R Miranda, S. Ferrer, F. Batallan, G. Fillion and J.P. Rebouillat, (1989) Antiferromagnetic ordering in Co-Cu single-crystal superlattices, *Phys. Rev (B)* 39(13), 9726-9729.
- [16] A. Cebollada R. Miranda, C.M. Schneider, P. Schuster and J. Kirschner (1991) Experimental evidence of an oscillatory magnetic coupling in Co/Cu/Co epitaxial layers, *J. Magn. Magn. Mat.*, 102:25-29.
- [17] H.A.M. de Gronckel, K. Kopinga, W.J.M. de Jonge, P. Panissod, J.P. Schillé and F.J.A. den Broeder (1991) Nanostructure of Co/Cu multilayers, *Phys. Rev. B.*, 44(16) 9100-9103.
- [18] C.M. Emmerson and T.-H. Shen (1996) A study of Co/Cu multilayer growth on Si(111) with silicide buffer layers, *J. Magn Magn. Mat.* 156:15-16.

- [19] D. Greig, M.J. Hall, C. Hammond, B.J. Hickey, H.P. Ho, M.A. Howson, M.J. walker, N. Wiser and D.G. Wright (1992) The giant magnetoresistance of Co / Cu superlattices grown by MBE, *J. Magn Magn. Mat.* 110:L239-L246.
- [20] A.J.R. Ives, R.J. Hicken, J.A.C. Bland, C. Daboo M. Gester, and S.J. Gray (1994) High-field polar MOKE magnetometry as a probe of interlayer exchange coupling in MBE-grown Co/Cu/Co (111) and Fe/Cr/Fe (001) wedged trilayers, *J. Appl. Phys.* 75(10) 6458-6460.
- [21] J.S. Lord, H. Kubo, P.C. Riedi, and M.J. Walker (1993) Nuclear magnetic resonance of molecular beam epitaxially grown Co-Cu superlattices that exhibit large magnetoresistance, *J. Appl. Phys.*, 73(10): 6381-6383.
- [22] W.F. Egelhoff, Jr. and M.T. Kief (1992) Antiferromagnetic coupling in Fe/Cu/Fe and Co/Cu/Co multilayers on Cu(111), *Phys. Rev. B.*, 45(14) 7795-7804.
- [23] D.H. Mosca, F. Petroff, A.Fret , P.A. Schroeder, W.P. Pratt, Jr., and R. Loloee (1991) Oscillatory interlayer coupling and giant magnetoresistance in Co/Cu multilayers, *J. Magn Magn. Mat.* 94: L1-L5.
- [24] M.E. Tomlinson, R.J. Pollard, D.G. Lord and P.J Grundy (1992) Giant magnetoresistance in sputter deposited Co/Cu multilayer systems, *J. Magn. Magn. Mat.*, 111: 79-82.
- [25] K. Rätzke, M.J. Hall, D.B. Jardine, W.C. Shih, R.E. Somekh and A.L. Greer, (1999) Evolution of microstructure and magnetoresistance in Co/Cu multilayers during annealing, *J. Magn. Magn. Mat.* 204: 61-67.
- [26] S. Miura, M. Tsunoda, T. Nagatsuka, S. Sugano, and M. Takahashi (1999) Drastic change of giant magnetoresistance of Co/Cu multilayer by decreasing residual impurities in sputtering atmosphere, *J. Appl. Phys.* 85(8): 4463-4465.
- [27] R.J. Pollard, M.J. Wilson, and P.J. Grundy (1995) Microstructure and GMR in (111) sputter-deposited Co/Cu multilayers, *Mat. Res. Soc. Proc.* 384 365-370.J

- [28] P. Nallet, E. Chassaing, M.G. Walls, and M.J. Hÿtch (1996) Interface characterization in electrodeposited Cu-Co multilayers, J. Appl. Physics, 79(9) 6884-6889.
- [29] W.F. Egelhoff, Jr., and M.T. Kief (1992) Fe/CuFe and Co/Cu/Co multilayers on Cu(111): The absence of oscillatory antiferromagnetic coupling, IEE Trans. Magn. 28(5): 2742-2744.
- [30] A.R. Modak, D.J. Smith, and S.S.P.Parkin, (1994) Dependence of Giant Magnetoresistance on Grain Size in Co/Cu Multilayers, Phys. Rev. (B). 50(6), 4232-4235.
- [31] M. Chádek, C. Dorner, A. Buchal, V. Valvada, and H. Hoffmann (1996) Quantitative *in situ* X-ray diffraction analysis of magnetic multilayers during annealing, J. Appl. Phys 80(3) 1437-1445.
- [32] H. Zhang, R.W. Cochrane, Y Huai, M.Mao,X. Bian and W.B. Muir (1994) Effect of annealing on the giant magnetoresistance of sputtered Co/Cu multilayers, J. Appl. Phys. 75(10): 6534-6536.
- [33] H. Kikuchi, J.-F. Bobo, and R.L. White (1997) The effect of pinholes on the properties of Co/Cu multilayers, IEEE trans. Mag. 33(5) 3583-3585.
- [34] D.J. Smith, Z.G. Li, A.R. Modak, S.S.P. Parkin, R.F.C. Farrow and R.F. Marks, (1994) High resolution imaging of magnetic multilayers, Scripta Met Mat. 30(6) 689-694.
- [35] D. Kubinski, M. Parsons and J. Hansas (2000) Magnetoresistive properties of 1st AFM Co/Cu multilayers sputtered in an Ar+O₂ atmosphere, Mat. Res. Soc. Proc., 614: F8.8.1F-8.8.6.
- [36] M. Ohring (1992) The Materials Science of Thin Films, Academic Press, San Diego
- [37] I.K. Schuller, S. Kim and C Leighton (1999) Magnetic supperlattices and multilayers, J. Magn. Magn. Mat. 200: 571-582.

- [38] C.J. Smithells, E.A. Brandes and G.B. Brook (1998) *Smithells Metals Reference Book 7th Ed.* Butterworth-Heinemann.
- [39] C. Gente, M. Oehring, and R. Bormann (1993) Formation of thermodynamically unstable solid solutions in the Cu-Co system by mechanical alloying. *Phys. Rev. B* 48(18) 13244-13252.
- [40] P. Wu, E.Y.Jiang, H.L. Bai, H.Y. Wang (1997) Evolution of Microstructure in Co-Cu Multilayers during Thermal Annealing, *Phys. Stat. Sol. (a)* 161:389-397
- [41] D.J. Smith, A.R. Modak, T.A. Rabedeau, S.S.P.Parkin, (1997) Growth and Structural Characterization of Highly Oriented Sputter-Deposited (111), (110), and (100) Co/Cu Superlattices, *Appl. Phys. Lett.* 71(11) 1480-1482
- [42] C. Mény, P.Panissod and R. Loloee (1992) Structural study of cobalt-copper multilayers by NMR, *Phys. Rev. (B).* 45(21), 12269-12277.
- [43] J.M. Slaughter, W.P. Pratt, P.A. Schroeder. (1989) Fabrication of Layered Metallic Systems for Perpendicular Resistance Measurements. *Rev. Sci. Insts.* 60(1) 127-131.
- [44] S-F Lee, Q. Yang, P.Holody, R. Loloee, J.H. Hetherington, S. Mahmood, B. Ikegami, K. Vigen, L.L. Henry, P.A. Schroeder, W.P. Pratt, Jr. and J. Bass, (1995) Current-Perpendicular and Current-Parallel Giant Magnetoresistance in Co/Ag Multilayers *Phys. Rev (B)* 52(21), 15426-15441.
- [45] S.M. Durbin, J.E. Cunningham and C.P. Flynn (1982) Growth of single-crystal metal superlattices in chosen orientations, *J. Phys. F: Met. Phys.* 12: L75-78.
- [46] R. Loloee, W.P. Pratt, Jr., and M.A. Crimp (2001) Crystallographic characterization of sputter-deposited epitaxial Nb-Cu-Co and Nb-Cu-Permalloy multilayers using electron back-scatter diffraction patterns, *Philos. Mag. A.*, 81(2) 261-273.
- [47] V. Vitek, G. Gutekunst, J. Mayer and M. Rühle (1995) Atomic structure of misfit dislocations in metal-ceramic interfaces, *Philos. Mag. A* 71(6): 1219-1239.

- [48] G. Gutekunst, J. Mayer, V. Vitek and M. Rühle (1997) Atomic structure of epitaxial Nb-Al₂O₃ interfaces II. Misfit dislocations, *Philos. Mag. A*, 75(5): 1357-1382

- [49] A. Levay, G. Möbus, V. Vitek, M. Rühle and G. Tichy (1999) Structure of misfit dislocations in niobium-sapphire interfaces and the strength of interfacial bonding: an atomistic study, *Acta Mater.* 47(15):4143-4152.

- [50] J. Yuan, V. Gupta, and M. Kim, (1995) Structure and Chemistry of Nb/Sapphire Interfaces with and without Interlayers of Sb and Cr, *Acta Metall. Mater.* 43(2) 769-779

- [51] H. Kung, Y.-C. Lu, A.J. Griffin, Jr., M. Nastasi, T.E. Mitchell, and J.D. Embury, (1997) Observation of Body Centered Cubic Cu in Cu/Nb Nanolayered Composites, *Appl. Phys. Lett.* 71(15) 2103-2105.

- [52] J.N. Ness, W.M. Stobbs and T.F. Page (1986) A TEM Fresnel diffraction-based method for characterizing thin grain-boundary and interfacial films, *Philos. Mag. A.*, 54(5): 679-702

- [53] F.M. Ross and W.M. Stobbs (1991) Computer modeling for Fresnel contrast analysis, *Philos. Mag. A.*, 63(1): 37-70.

- [54] H. Geng, J.W. Heckman, W.P. Pratt, J. Bass, F.J. Espinosa, S.D. Conradson, D. Lederman, and M.A. Crimp (1999) Occasional "long-range" nonequilibrium body-centered-cubic structures in NiFe/Cu spin valves, *J. Appl. Phys.*, 86(8), 4166-4175.

- [55] R.W. Horne and R. Markham (1972) Optical diffraction techniques, *In* A. M. Glauert, ed., *Practical Methods In Electron Microscopy*, Vol1., American-Elsevier Publishing Co., NY

- [56] R. Sinclair, R. Gronsky and G. Thomas (1976) Optical diffraction from lattice images of alloys, *Acta Metall.* 24: 789-796.

- [57] M. Watanabe and D.B. Williams (1999) Atomic-level detection by X-ray microanalysis in the analytical electron microscope, *Ultramicroscopy* 78:89-101.

- [58] P.A. Stadelmann (1987) EMS-A software package for diffraction analysis and HREM image simulation in materials science. *Ultramicroscopy* 21:131-146. [66]
- [59] H. Geng, J.W. Heckman, R. Loloee, W.P. Pratt, J. Bass, and M.A. Crimp, (2001) The Effect of Indium contamination and Nb Contact Layers on the Structure of Ag/NiFe GMR SpinValves., (Submitted to *Mat. Sci and Eng.*).
- [60] R. Loloee, (2000) Growth and Characterization of Epitaxial Films and Magnetic Multilayers Grown by D.C. Sputtering, Doctoral Dissertation, Michigan State University, E. Lansing, MI.
- [61] H. Geng, R. Loloee, J.W. Heckman, J. Bass, W.P. Pratt, Jr. and M.A. Crimp (2000) Structural characterization of epitaxial GMR magnetic multilayers and spin valves grown by sputter deposition, *Mat. Res. Soc. Symp. Proc.* 614: F4.7.1F4.7.6.
- [62] R. Loloee, (2001) personal communication
- [63] J.C. Bravman and R. Sinclair (1984) The Preparation of Cross-Section Specimens for Transmission Electron Microscopy *J. Electron Micro. Tech.*, 1, 53-61.
- [64] D.A. Howell, (1995) Conventional and High-Resolution Transmission Electron Microscopy Study of Spin-Glass/ Amorphous-Silicon Multilayers, Masters Thesis, Michigan State University, E. Lansing, MI.
- [65] NIST/NIH Desk Top Spectrum Analyzer, available from the National Institute of Standards and Technology, Gaithersberg, MD 20899, USA. (<http://micro.nist.gov/DTSA>).
- [66] D.B. Williams and C.B. Carter (1996) *Transmission Electron Microscopy: A textbook for materials science.* Plenum Press, NY. 729 pp.
- [67] S.M. Allen (1981) Foil thickness measurements from convergent-beam diffraction patterns, *Phil. Mag. A* 43(2): 325-335.

- [68] S.M. Allen and E.L. Hall (1992) Foil thickness measurements from convergent-beam diffraction patterns An experimental assessment of error, *Phil. Mag.* A46(2): 243-253.
- [69] Z. Horita, K. Ichitani, T. Sano and M Nemoto (1989) Applicability of the differential X-ray absorption method to the determination of foil thickness and local composition in the analytical electron microscope, *Phil. Mag. A*, 59(5): 939-952.
- [70] W. Rasband NIH Image (developed at the U.S. National Institutes of Health and available on the internet at <http://rsb.info.nih.gov/nih-image/>)
- [71] C. Russ and J. Russ (1996) The Image processing Tool Kit, Reindeer Games, Inc. Asheville, NC 28801
- [72] A. A. Reeves (1990) Optimized fast hartley transformation for the MC68000 with applications in image processing, Masters Thesis, Dartmouth College, Hanover, New Hampshire.
- [73] P. Bödeker, A. Abromeit, K. Bröhl, P. Sonntag, N. Metoki, and H. Zabel (1993) Growth and X-ray characterization of Co/Cu (111) superlattices, *Phys. Rev. B.* 47(4) 2553-2361.
- [74] H. Geng, R. Loloee, J.W. Heckman, J. Bass, W.P. Pratt, Jr. and M.A. Crimp (2000) Structural characterization of epitaxial GMR magnetic multilayers and spin valves grown by sputter deposition, *Mat. Res. Soc. Symp. Proc*, Vol 614. F4.71-F4.76.
- [75] Hÿtch, M.G. Walls, and J.-P. Chevalier (2000) Measurement of roughness and diffuseness of interfaces, *Ultramicroscopy* 83: 217-225
- [76] H.-J. Lee, K.-W. Kwon, C. Ryu and R. Sinclair (1999) Thermal stability of a Cu/Ta multilayer: An intriguing interfacial reaction, *Acta. Mater.* 47(15): 3965-3975.
- [77] K. Barmak, G.A. Lucadamo, C. Cabral, Jr., C. Lavoie, and J.M.E. Harper (2000) Dissociation of dilute immiscible copper alloy thin films, *J. Appl. Phys.* 87(5): 2204-2214.

- [78] P. G. Stecher (ed) (1968) The Merck index; an encyclopedia of chemicals and drugs 8th ed. Merck, Rahway, N.J.
- [79] K. Heinz, S. Müller and L. Hammer (1999) Crystallography of ultrathin iron, cobalt and nickel films grown epitaxially on copper, J. Phys.: Condens. Matter 11: 9437-9454.
- [80] R.E. Dunin-Borkowski (2000) The development of Fresnel contrast, and the interpretation of mean inner potential profiles at interfaces, Ultramicroscopy 193-216.
- [81] K.M. Krishnan (1999) Magnetism and microstructure: The role of interfaces, Acta mater. 47(15): 4233-4244.
- [82] D.-Y. Shih, C.-A Change, J. Paraszczak, S. Nunes and J. Cataldo (1991) Thin-film interdiffusions in Cu/Pd, Cu/Pt, Cu/Ni, Cu/NiB, Cu/Co, Cu/Cr, Cu/Ti and Cu/TiN bilayer films: Correlations of sheet resistance with Rutherford backscattering spectrometries, J. Appl. Phys. 70(6) 3052-306

MICHIGAN STATE UNIVERSITY LIBRARIES



3 1293 02356 3012